

**The Masses of Proton-Rich Isotopes of Nb, Mo, Tc, Ru and Rh and
Their Influence on the Astrophysical rp and νp Processes**

BY

Jennifer Fallis

A Thesis Submitted to
the Faculty of Graduate Studies
in Partial Fulfillment of the Requirements for the Degree of

DOCTOR OF PHILOSOPHY

Department of Physics and Astronomy
University of Manitoba
Winnipeg, Manitoba

© Jennifer Fallis, October 2009

Abstract

The Canadian Penning Trap mass spectrometer located at Argonne National Laboratory has been built for the purpose of studying the masses of both stable and unstable nuclides. For this thesis 18 proton-rich unstable nuclides of elements Nb, Mo, Tc, Ru and Rh have been measured with this apparatus to an average precision of 7.8×10^{-8} . The masses of 6 of these nuclides had not been measured when this thesis was undertaken, and 4 more were not known to the precisions required for use in astrophysical nucleosynthesis models. The masses of these nuclides were of particular interest as the reaction paths of two proposed nucleosynthetic processes, the rp and νp processes, pass through this region. The rp process is thought to occur in X-ray bursts and directly affects the X-ray luminosity which is emitted from these objects. The νp process is thought to occur in the inner regions of the material ejected during a core-collapse supernova explosion and is of particular interest as it may answer some outstanding questions about the origins of the chemical elements in the Universe. The Canadian Penning Trap and associated apparatus were used to determine the masses of 18 nuclides, some for the first time ever. Our measurements improve the precision on all of the masses, by a factor of 70 in some cases. Our results are necessary to determine the proton-separation energies for these nuclides which are critical for determining the paths and reaction rates of the rp and νp processes. In particular, the effect of our measurements of ^{92}Ru and ^{93}Rh on the expected production ratio of ^{92}Mo to ^{94}Mo in the νp process, and the effect of our measurement of ^{87}Mo on the path of this process will be discussed.

Acknowledgements

It is impossible to adequately thank everyone whose help and support has contributed to the development of this thesis. I can only hope that these small words can convey some sense of my gratitude.

My sincerest thanks to both Kumar Sharma and Guy Savard for their advice and the example they have set. Though I began this work as part of a Master's program it didn't take long for me to decide to transfer into the PhD program because I knew it would be hard to find anywhere else where I would learn as much over the course of my studies. I appreciate their ability to encourage independence while still providing guidance, and thank them for always expecting the best while remaining tolerant of the inevitable learning curve.

Thank you also to Jason Clark, for leaving really big shoes to fill and then doing so much to help me as I tried to fill them. This appreciation is not only for help in scientific aspects, but also with everything from finding an apartment to the paper-work involved in living in a foreign country, to the L^AT_EX template that I used in this thesis. I started my PhD with two advisors and feel in some ways like I am finishing with three.

Many thanks to fellow students Dan Lascar, Jon Van Schelt, Shane Caldwell, Matt Sternberg and Gang Li with whom I spent countless hours in the "triangle room" and who managed to ensure that while this whole process was a lot of work, it was also a lot of fun.

I am also thankful for the many post-docs I have had the opportunity to work with over the course of my studies, with specific thanks to Hariprakash Sharma for teaching me to operate the CPT system and to Adam Hecht and Nick Scielzo who were always willing to take the time to answer my questions. Thanks also to Catherine Deibel, Chris Wrede and Anuj Parikh for their comments on various papers, many of which have also been incorporated here.

My thanks to the Operations and Technical staff at the ATLAS facility, specifically to Tony Levand, Bruce Nardi, Bruce Zabransky, and John Rohr who were instrumental in getting and keeping things working.

This thesis would also not have been possible without all of the support I received from those outside of the lab as well. Enumerable thanks to my Mom, Dad and sister who have always supported me in any endeavor I chose to pursue. And last but certainly not least, enormous thanks to my husband Michael who has endured my many long nights working on assignments or at the lab, as well as years living apart, and remained unfailingly supportive throughout all of it.

Contents

1	Introduction	1
1.1	A brief history of mass measurements	1
1.2	The nuclear landscape	3
1.3	The role of mass measurements in nuclear astrophysics	6
1.3.1	Basic nucleosynthesis	7
1.3.2	The rp -process: nucleosynthesis in X-ray bursts	9
1.3.3	The νp -process: proton-rich nucleosynthesis in supernovae	13
2	Ion traps	17
2.1	Penning traps	18
2.1.1	Trapping potential and motion of the ions in the trap	18
2.1.2	Mass selection in gas-filled traps	22
2.2	Linear quadrupole mass spectrometers	24
2.2.1	Trapping potentials and electrode configuration	24
2.2.2	Stable vs. unstable orbits	25
2.2.3	Mass selection in the linear RFQ	28
2.2.4	Effect of gas in the trap	30
3	The Canadian Penning Trap system	33
3.1	Acquiring isotopes	35
3.1.1	Production	35
3.1.2	The gas catchers	42
3.1.3	RFQ ion guide	46
3.2	Ion transport, mass selection and storage	49
3.2.1	Isobar separators	50
3.2.2	Transfer line, deflection pulses and beam diagnostics	56
3.2.3	Linear RFQ trap	62
3.3	Measurement	65
3.3.1	The precision Penning trap	66
3.3.2	Dipole and quadrupole RF excitations	73
3.3.3	Ion detection	77
3.4	System operation	80
3.4.1	Timing control system and RF frequency settings	80
3.4.2	Data acquisition system	84
3.4.3	Data analysis program	84

4	Data, analysis and results	89
4.1	Data and Analysis	92
4.1.1	Summary of experiments	92
4.1.2	Data Analysis	96
4.2	Systematic effects	100
4.2.1	Electric field imperfections	100
4.2.2	Magnetic field imperfections	101
4.2.3	Misalignments	102
4.2.4	Ion-ion effects	103
4.2.5	The resulting systematic uncertainty	104
4.3	Final Numerical Results	105
5	Discussion	109
5.1	Previous mass determinations, extrapolations and models	109
5.2	Comparison of our data to existing values	115
5.2.1	^{87}Nb	116
5.2.2	$^{87,90-92}\text{Mo}$	117
5.2.3	$^{90-93}\text{Tc}$	120
5.2.4	$^{90-94}\text{Ru}$	125
5.2.5	$^{92-95}\text{Rh}$	129
5.3	Separation energy systematics	134
5.4	Extrapolations	139
5.4.1	From systematic trends	139
5.4.2	Using the Garvey-Kelson relations	145
5.5	Implications for Astrophysics	148
5.5.1	The νp process	148
5.5.2	The rp process	156
5.6	Implications of the ^{92}Rh mass for the pp decay of ^{94}Ag	158
6	Conclusions and Outlook	160
6.1	Conclusions	160
6.2	Outlook	161
A	Laplace's equations and the trapping potentials	163
A.0.1	2D confinement	164
A.0.2	3D confinement	165
B	Error propagation	166
C	List of Acronyms	171
	References	172

List of Figures

1.1	Portion of the chart of the nuclides	4
1.2	Possible nuclear reactions on a given nuclide	5
1.3	The origins of Mo isotopes	8
1.4	The rp -process path	10
1.5	The endpoint of the rp -process path	13
1.6	A comparison of the rp - and νp -process paths between Zr and Cd	15
2.1	Penning trap electric field and possible electrode structures	19
2.2	Ion motion in a Penning trap	21
2.3	ω_- to ω_+ conversion in both high-vacuum and gas-filled environments	23
2.4	Linear RFQ trap structure using round rods	25
2.5	The 1 st stability region of the linear RFQ ion guide	28
3.1	CPT System Layout	34
3.2	Fusion-evaporation reaction channels	36
3.3	The target wheel	37
3.4	The two variable degrader systems	40
3.5	The high-intensity gas catcher	45
3.6	Segments of the linear RFQ ion guide	47
3.7	1 st generation isobar separator electrode structure	52
3.8	2 nd generation isobar separator electrode structure	55
3.9	Transfer line schematic: RFQ ion guide to CPT tower	57
3.10	Transfer line schematic: IS2 beam-line	57
3.11	Electrostatic quadrupole deflector	58
3.12	Location of diagnostic stations	59
3.13	Quadrupole deflector settings when using MCP and Si detectors	61
3.14	Linear RFQ trap electrode structure	63
3.15	CPT tower	64
3.16	CPT electrode configuration	68
3.17	TOF drift tube schematic	73
3.18	Example time-of-flight spectrum	77
3.19	Electron multiplication in MCPs and channeltrons	78
3.20	MCP diagram	79
3.21	Channeltron diagram	80
3.22	Box diagram of timing modules and triggering conditions	83
3.23	Example spectrum: number of ions per MCS channel	85

4.1	Representative TOF spectra for ^{87}Mo , ^{90}Tc , ^{90}Ru , ^{92}Rh	95
4.2	Comparison of the Penning trap mass excesses and the AME03 values	106
4.3	Comparison of measured mass excesses from the CPT with those of other Penning traps	107
5.1	Comparison of measured mass excesses from the CPT with various mass models	112
5.2	Calculating Q_{EC} from β -endpoint measurements	113
5.3	Energy spectrum of decays with 2 and 3 body final states	115
5.4	^{87}Mo decay energy measurements	118
5.5	Comparison of ^{87}Mo mass excess values	119
5.6	Comparison of ^{90}Tc mass excess values	122
5.7	^{90}Tc measurements and potential excitation energies	123
5.8	Level diagram for ^{91}Ru	125
5.9	Comparison of ^{91}Ru mass excess values	127
5.10	^{94}Rh energy levels	132
5.11	S_{2p} values	135
5.12	S_p values	136
5.13	S_{2n} values	138
5.14	S_{2p} extrapolations	140
5.15	S_{2n} extrapolations	141
5.16	$Q_{2\beta}$ extrapolations	142
5.17	Separation energies on the chart of the nuclides	144
5.18	Single-particle levels of nuclides in the Garvey-Kelson relation	146
5.19	Relative positions of the nuclides in the Garvey-Kelson relation	147
5.20	Location of our measurements relative to the νp process path	148
5.21	Nuclear reactions important to the νp process	149
5.22	Reactions linking ^{92}Ru , ^{93}Rh and ^{94}Pd in the νp process	152
5.23	A comparison of $S_p(^{93}\text{Rh})$ values	153
5.24	Location of our measurements relative to the rp process path	156
5.25	p and pp decay from the (21^+) state of ^{94}Ag	158
6.1	Progression of measured masses	161

List of Tables

3.1	Example degrader thicknesses: ladder degrader	41
3.2	Example degrader thicknesses: parallel wheel degrader	41
3.3	Small gas catcher: example DC and RF settings	44
3.4	High-intensity gas catcher: example RF and DC settings	46
3.5	Linear RFQ ion guide: example DC and RF settings used with the small gas catcher	49
3.6	Linear RFQ ion guide: example DC and RF settings used with the high-intensity gas catcher	50
3.7	Resolving powers required	51
3.8	1 st generation isobar separator settings	51
3.9	2 nd generation isobar separator settings	54
3.10	Quadrupole deflector voltages	60
3.11	Linear RFQ trap settings	63
3.12	Precision Penning trap potentials	68
3.13	TOF drift tube voltages	74
4.1	Summary of beams, energies and target materials	93
4.2	Frequency ratios between the unknown and calibrant ions	98
4.3	Table of auxiliary data	99
4.4	Summary of measured masses and comparison to other values	108
5.1	Comparison of measured mass excesses to mass models	111
5.2	List of mass excess determinations for ⁸⁷ Nb	116
5.3	List of mass excess determinations for ⁸⁷ Mo	117
5.4	List of mass excess determinations for ⁹⁰ Tc	121
5.5	List of mass excess determinations for ⁹³ Tc	124
5.6	List of mass excess determinations for ⁹¹ Ru	126
5.7	Beams, targets and energies used to study ⁹¹ Ru	126
5.8	Beams, targets and energies used to study ⁹² Rh	130
5.9	Extrapolated S_{2p} , S_{2n} and $Q_{2\beta}$ values	143
5.10	Extrapolated masses	145
5.11	Masses calculated using Garvey-Kelson relation	147
5.12	νp -process reaction rates for ⁸⁷ Mo and ⁸⁸ Tc	155

Chapter 1

Introduction

1.1 A brief history of mass measurements

During my tenure as a graduate student we have passed the 100 year anniversary of Einstein's classic paper on special relativity which provided the famous relation: $E = mc^2$ [1]. An examination of some of the other fundamental equations in physics such as Newton's second law, $F = ma$, from classical mechanics and Schrödinger's equation, $i\hbar\frac{\partial}{\partial t}\psi = -\frac{\hbar^2}{2m}\Delta\psi + V\psi$, from quantum mechanics, shows that mass is required everywhere and could arguably be the most important property of an object, atom or particle.

This is certainly no exception in Nuclear Physics. Nuclear masses have a peculiar property in that the mass of any given isotope is less than the sum of its parts. In other words, if we were to add the mass of each proton and neutron present in the nucleus it will be larger than the overall mass of the nucleus. This difference in mass is the binding energy of the nucleus. The relatively consistent value of the binding energy per nucleon across the elements, combined with measurements of nuclear radii led to the first information about the strong nuclear force indicating that it was a very short range force [2]. Looking at how the binding energy of nuclides changes across the table of isotopes led to the discovery of the Nuclear Shell Model for which Maria Goeppert Mayer and Hans Jensen won the Nobel Prize in 1963 [3]. Most importantly to this thesis, by determining the differences in binding energy between

two neighboring nuclides we can deduce information about their nuclear reaction rates and energies [2, 4, 5].

Because of the importance of nuclear masses there has been a long history of mass measurements, beginning shortly after the turn of the 20th century with J.J. Thompson and his positive ray parabola apparatus [6]. His student F.W. Aston went on to build the first mass spectrograph which determined a particle's mass through deflection by magnetic and electric fields [6]. Since then, most of the stable isotopes have been measured by increasingly precise deflection mass spectrometers, such as the Manitoba II mass spectrometer [7] still present and in operation at the University of Manitoba [8]. Recently however, Penning trap mass spectrometers have been revolutionizing the precise mass measurement of ions, allowing measurements to be made with a precision exceeding 1×10^{-10} (0.1 ppb) on stable isotopes [9].

Within the last two decades it has become possible to not only create but efficiently study an increasing number of short-lived radioactive isotopes. Penning trap mass spectrometers, which were once used as stand alone devices, are being added to more elaborate systems and attached to some form of particle accelerator which allows for the production of these radioactive ions. With approximately 6 times as many isotopes available to be measured than in the past [10], and with new facilities on the horizon which are expected to make far more of these short-lived nuclides available for study, mass measurement programs such as the program underway using the Canadian Penning Trap (CPT) certainly appear to have a strong future. This is especially true when one considers the other fields of physics who are eager to have not only mass measurements of these newly available nuclides (such as astrophysics), but also require already known masses measured to ever increasing precisions (for studies of fundamental symmetries).

Mass measurements using the CPT have contributed to: tests of the V_{ud} term of the CKM (Cabibbo-Kobayashi-Maskawa) quark-mixing matrix which is a test of the Standard Model [11, 12], double β -decay studies and the search for neutrinoless

double β -decay [13], systematic studies of masses and neutron-separation energies on the neutron-rich side of the valley of stability [14, 15], as well as contributed Q_p or S_p values of importance to the astrophysical rp - and νp -processes [16, 17, 18, 19]. The measurements presented in this thesis are of particular interest in astrophysics.

1.2 The nuclear landscape

Similarly to the periodic table of elements which display all of the known chemical elements, the chart of the nuclides (a portion of which is shown in figure 1.1) shows all of the known isotopes of all of the known elements. This includes not only the stable isotopes but also all the unstable isotopes as well. As stable nuclides are more bound they have lower masses than their unstable counterparts. Given the shape of the surface which results if one plots mass as a function of Z and N , this region of stable ions is known as “the valley of stability”. Proton-rich nuclides lie to the left of the valley of stability on the chart (figure 1.1) and their primary means of decay back towards stability are β^+ decay and electron capture. These decay reactions turn one of the excess protons (p) in the nucleus into a neutron (n) resulting in a nuclide of the same mass but of the neighboring element with $Z - 1$. Neutron-rich nuclides lie along the right of the valley of stability on the chart and decay to stability primarily through β^- decay (here an excess n becomes a p and results in a nuclide of the same mass but of the neighboring element with $Z + 1$).

Another feature indicated on the chart of the nuclides are the proton and neutron “magic numbers”, which are the number of protons and neutrons required to fill each “shell” of the nucleus. As protons and neutrons have independent shell structures these magic numbers are seen as columns or rows of nuclides which have p or $n = (8, 20, 28, 50, 82\dots)$.

In addition to the two forms of β decay and the electron capture reactions already mentioned, there are many different reactions and decays which can occur given appropriate conditions (figure 1.2). The nuclide which exists prior to the reaction is

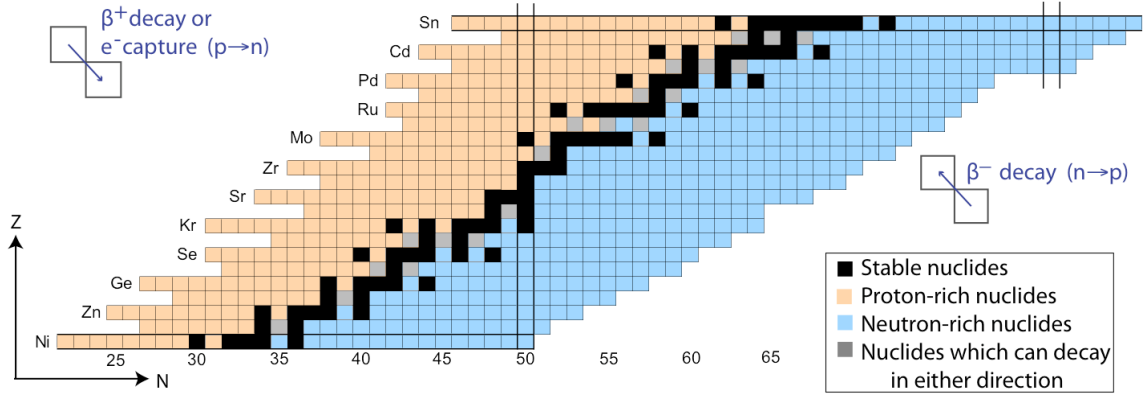


Figure 1.1: A portion of the chart of the nuclides which includes the isotopes of elements from Ni ($Z = 28$) to Sn ($Z = 50$), both of which are proton magic numbers (neutron magic numbers 50 and 82 are also indicated). The directions of β^+ and β^- decay are indicated. Electron capture reactions follow the same path as β^+ decay.

known as a “parent nuclide” and the nuclide which exists after the reaction is known as a “daughter nuclide”. The equations for the reactions can either be written as:

$$\mathcal{N}_i + P_i \longrightarrow \mathcal{N}_r + P_r, \quad (1.1)$$

where \mathcal{N}_i and \mathcal{N}_r are the initial and resulting nuclides and P_i and P_r are initial and resulting particles or they can also be written in a short-hand notation where, using the same variables, the reaction is written as:

$$\mathcal{N}_i(P_i, P_r)\mathcal{N}_r. \quad (1.2)$$

Often when talking about a specific type of reaction as opposed to a reaction on a specific nuclide this is abridged even further and any reaction which has the same incident and resulting particle is then written as a “ (P_i, P_n) ” reaction. Several examples which will be used often in this work are proton-capture reactions (p, γ) , photo-disintegration reactions (γ, p) , and neutron-capture reactions such as (n, p) or (n, γ) .

The energy required for any given reaction is known as the reaction Q value and

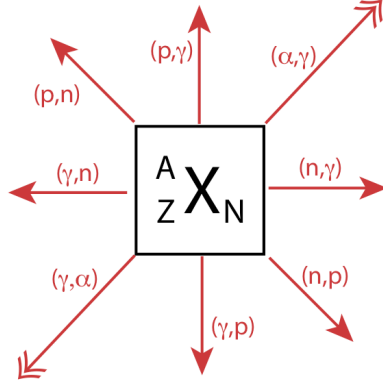


Figure 1.2: All of the nuclear reactions which will be discussed in this work are included above. The single arrows indicate that the reaction produces the next neighboring nuclide, the double arrows indicate that a nuclide past the neighboring nuclide is produced (as capturing an α particle adds $2p$ and $2n$ to the parent nuclide).

is defined in its most general form as follows:

$$(M_{parent} + M_i - M_{daughter} - M_o) c^2 = Q \quad (1.3)$$

where M_i is the mass of any “incoming” particle involved in the reaction and M_o is the mass of any “outgoing” particle. In most cases, the speed of light, c , is often set to 1 and is not written explicitly. We can see that if the mass of all of the particles and nuclides involved in the reaction are known, the energy of the reaction can be determined. Similarly, if the energy can be determined and three of the four masses are known, the fourth can be determined.

A distinction is often made between the energy required for a fusion reaction involving an incoming nucleon (such as proton or neutron capture) and the energy required to remove the same nucleon from the nucleus (such as during photo-disintegration). The energies in the first case are known as reaction Q values. The reverse are known as separation energies (and denoted by S). In the case of inverse reactions (such as (p, γ) and (γ, p)) these two values are not only related, they have the same magnitude – the only difference is which nuclides are considered the “parent” and “daughter” nuclides in equation 1.3 (and which particles are considered to be “incoming” and “outgoing”).

All of the mass data which has been measured to date, either through direct techniques, such as deflection mass spectrometry and Penning trap measurements, or determined from reaction energy measurements, are compiled and evaluated in the Atomic Mass Evaluation (AME). The most recent version is from 2003 (AME03) [20, 21]. In addition to compiling, evaluating and presenting the existing data, the AME uses the systematic trends of various separation energies (S_{2p} , S_{2n} , $Q_{2\beta}$ and Q_{α}) to extrapolate 3 to 4 mass values beyond where mass measurements currently exist.

1.3 The role of mass measurements in nuclear astrophysics

Nuclear Astrophysics is a rich area of study that furthers our understanding of stellar processes, the origin and observed abundances of the chemical elements, and allows us to better understand the fundamentals of nuclear physics. According to what has been determined about the temperatures, densities and time-scales of the Big Bang, and given the fact that there are no stable isotopes of either $A = 5$ or 8 , nucleosynthesis in the Big Bang would only have created elements up to ${}^7\text{Li}$ [4, 5]. All of the almost one hundred other elements (from Li to U) which are naturally occurring on Earth have been created in the nuclear burning processes that fuel the stars, or in explosive stellar environments such as supernovae and X-ray bursts.

To have an accurate theory of a nucleosynthetic process, nuclear physics information such as masses, decay-channels, half-lives, branching ratios and energy level structures need to be well known. There has been a significant effort over the last 50 years or so to acquire this data and, in the case of the stable isotopes most of the required data is available. This has led to a clear understanding of the quiescent burning of the stars which occurs during their lifetimes. In explosive astrophysical scenarios, however, the nuclear reactions occur in such rapid succession that the nuclides involved do not have time to decay to stability before the next reaction takes place. The resulting nucleosynthesis involves very short-lived, unstable nuclides which

have been more difficult to produce in the laboratory and, though significant progress has been made, are consequently not yet as well studied.

1.3.1 Basic nucleosynthesis

There are several different nucleosynthetic processes depending on the environment in which the nucleosynthesis occurs. Two such processes occur under normal stellar conditions. Quiescent burning occurs in main sequence stars (stars in the midst of their normal lives) and this process, which involves fusion reactions among hydrogen and the light nuclides, slowly creates elements up to iron. Once iron has been reached however, it is no longer energetically favorable for these nuclei to fuse into heavier elements and the process stops. The second process occurs in asymptotic giant branch stars (stars nearing the end of their lives) and creates elements heavier than iron through slow neutron capture reactions. This is known as the *s* process. In this process existing seed nuclides slowly capture neutrons becoming the next isotope of the same chemical element. Once the products of these reactions reach an unstable nuclide, as this neutron capture occurs so rarely compared to even long-lived unstable nuclides, the atom β decays back to stability creating an isotope of the neighboring chemical element whose proton number is one higher [4].

In an explosive stellar environment such as when an accreting neutron star undergoes an X-ray burst or a star undergoes a supernova explosion temperatures and densities can reach 2.1×10^9 K and 10^{10} kg/m³ or greater [22]. With these conditions nuclear reactions are able to occur rapidly and can create elements much heavier than iron. In these processes the reactions happen so fast that the newly created nuclides do not have the opportunity to decay before becoming involved in another reaction. Therefore, these nucleosynthetic reaction chains run through regions of unstable isotopes where we have much less information.

In explosive nucleosynthesis the processes involved depend on the type of explosive scenario as well as the seed material available for the reaction. In neutron-rich

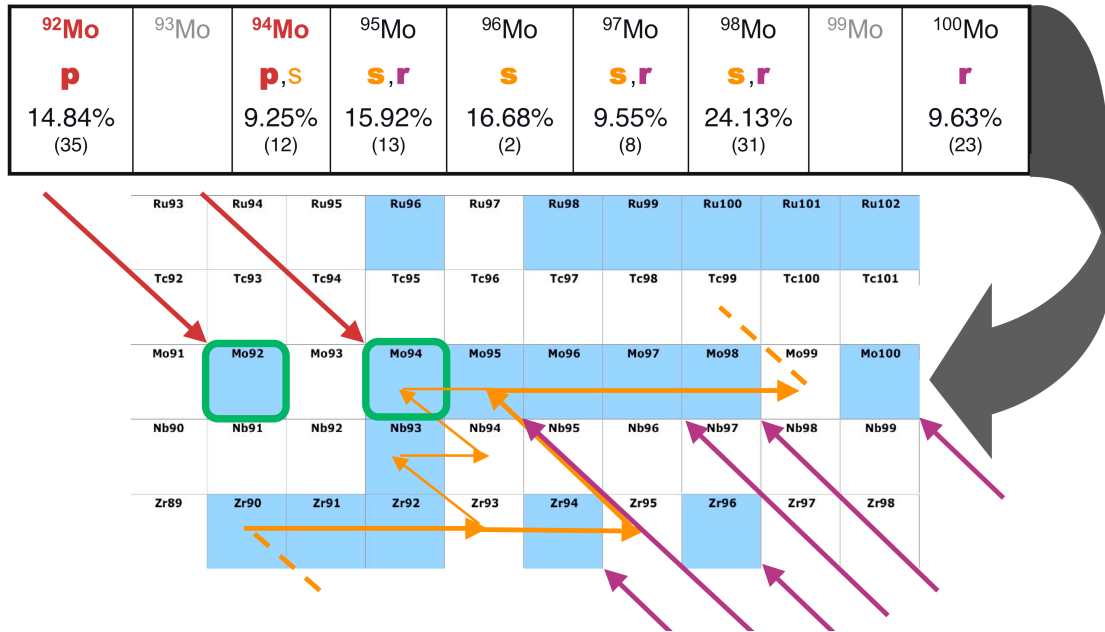


Figure 1.3: The various astrophysical processes which contribute to the production of Mo. Each isotope lists its observed elemental abundance and which process is thought to produce it. ⁹²Mo and ⁹⁴Mo are highlighted due to their significance to this thesis.

environments, such as certain stellar regions during a supernova explosion, it is the capture of neutrons which occurs rapidly and this process is named the rapid or *r* process. In proton-rich environments, such as when a star is undergoing an X-ray burst or in certain regions of a supernova, it is the capture of protons which takes place rapidly and these processes are known as *p* processes. In X-ray bursts this proton capture process is called the rapid proton, *rp*, process. In supernovae it is called the νp process due to the expected contribution of the interaction of the supernova neutrino-wind with the abundantly available protons.

Each of these reaction processes produce different nuclides based on the environment in which the process occurs and the decay chain of these nuclides as they decay back to stability. The result is that some isotopes will have multiple possible production mechanisms and others only one (Fig. 1.3). As already mentioned, very few of the chemical elements were produced in the Big Bang and so the abundances of the

individual chemical elements (and their isotopes) which make up our current Universe are entirely a result of the nucleosynthesis which occurs in these various processes. Determining what the isotopic and elemental abundances in the Universe actually are has proven to be more challenging than one might first assume as the elements most common on earth are not those found most commonly in the solar system. The abundances of the chemical elements which existed in the region of space which now makes up our solar system have been determined from studying the compositions of the sun and the planets resulting in what is known as the “observed solar abundance” (though “solar abundance” and “observed abundance” are also often used).

The Canadian Penning Trap (CPT) is being used to study the mass regions relevant to both the proton- and neutron-rich processes. This work focuses on measurements of masses important in the rp and νp processes.

1.3.2 The rp -process: nucleosynthesis in X-ray bursts

The main rp -process path begins when the temperatures and pressures on an accreting neutron star become high enough to trigger a breakout reaction from the hot CNO (Carbon Nitrogen Oxygen) cycle [23] and a chain of proton-capture (p, γ) reactions and α -capture reactions begins. The α -capture reactions occur up to mass 40 where the Coulomb barrier becomes too large for α capture to be favorable [24]. Above $A = 40$ only proton capture remains as a method of nucleosynthesis. As each p -capture moves the process further from the valley of stability, the proton separation energies (S_p) for each subsequent reaction decreases. As a result the proton capture chain will eventually reach a point where the (p, γ) rate and photo-disintegration (γ, p) rate are in equilibrium and the process stalls. The isotopes where this occurs are known as “waiting point” nuclides and the expected waiting point nuclides of the rp process can be seen in Figure 1.4.

Once the path of the rp -process arrives at one of these waiting point nuclides, due to the comparable rates of (p, γ) and (γ, p) , the lifetime with respect to the p -capture

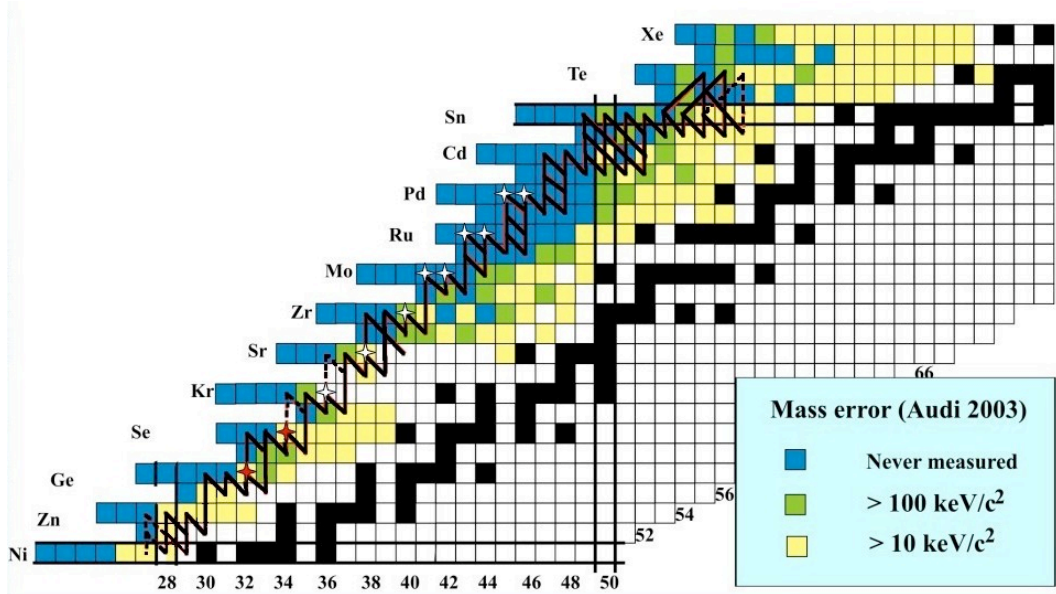


Figure 1.4: This graph contains mass uncertainties from [21] and information about the rp -process from [25]. The black line shows the expected rp -process path. The stars indicate the expected waiting points with the masses of the ones in red (grey) having been measured with the CPT.

reaction becomes potentially very long, to the point where it becomes comparable to or potentially longer than the β -decay lifetime. If the proton capture rate on the nuclide just above the waiting point is rapid enough there is a chance that before the nuclide created from a p -capture reaction on the waiting point nuclide has a chance to photo-disintegrate it may capture a second proton, thus bypassing the waiting point and continuing the rp process to heavier nuclides. The effective lifetime of the waiting point nuclide is in fact a combination of the β -decay and two p -capture lifetimes. If the two p -capture reactions occur at a slower rate than the β decay then the β -decay lifetime dominates and the nuclide is a true waiting point. If the two p -capture processes occur more rapidly than the β decay the effective lifetime of the waiting point nuclide is reduced and the nuclide might be less of a waiting point than originally believed.

As X-ray bursts only typically last between 10-100 seconds, knowing the effective lifetimes of these waiting point nuclides becomes important, especially considering

that the β -decay lifetimes for just the first two waiting points, ^{64}Ge and ^{68}Se , are 63.7 seconds and 35.5 seconds respectively. If the effective lifetimes of these two nuclides are the full β -decay lifetimes the rp process would not be able to produce any of the heavier isotopes in any significant quantity. In an effort to better determine p -capture Q -values and thus better determine the (p, γ) and (γ, p) reaction rates, there have been many mass measurements of the first few waiting point nuclides since the AME03. The first significant waiting point, ^{64}Ge was measured with the CPT at Argonne National Laboratory [17] and has also been measured by the LEBIT Penning trap group at Michigan State University [26]. The first direct measurement of ^{68}Se was also done with the CPT [16] with an indirect measurement from a β end-point measurement being reported around the same time [27]. This mass has also been measured recently using a time-of-flight (TOF) measurement using a cyclotron as a high precision mass-spectrometer, though it did not improve on the CPT precision [28]. ^{72}Kr and ^{76}Sr , the next two waiting-points of the process have both been measured by the ISOLTRAP Penning trap group located at ISOLDE at CERN [29, 30, 31, 32].

While both ^{64}Ge and ^{68}Se are still found to be significant waiting points of the rp -process, both are found to have enough of a contribution from the two successive p -capture reactions that the end-point of the rp process can be reached in the times available. We do find however that the time spent at ^{68}Se is far more significant than the time spent at ^{64}Ge [16, 17, 26].

Above these four measured waiting points on the chart of the nuclides there is a fairly large section of the rp -process which runs through nuclides whose masses have never been measured (from Mo to Cd: $Z = 42$ to 48). This region includes six expected waiting point nuclei (figure 1.4). The ISOL techniques, which were the first to produce ions of exotic nuclides for mass measurement, do not easily produce the elements in this region of the chart of the nuclides. The novel techniques used by the CPT system to produce and collect such ions are what have allowed us to extend our measurements into this previously inaccessible region.

Though the 6 expected waiting points in this region are not likely to stall the reaction process long enough to keep heavier isotopes from being created, which was a possibility for the waiting points closer to the beginning of the rp -process, they are still critical for a detailed understanding of the rp -process [33]. The time spent at these waiting points will have an effect on the shape of the predicted light-curve, one of the observable properties of an X-ray burst, which describes how the X-ray burst luminosity changes with time. Low Q_p values for nuclides along the rp -process path would cause the simulated light curve to be longer but less luminous at later times. Large Q_p values would result in the luminosity remaining higher for longer, but then falling off quickly [25].

The times spent at these waiting points also affect the resulting rp -process abundances. The large gravitational potentials of neutron stars prevent the material synthesized by the rp process from being ejected into the interstellar medium and so the observed solar elemental abundances are unlikely to be affected by the rp -process [34, 35]. As the “ashes” of the rp process contribute to the composition of the seed material for future X-ray bursts, a clear understanding of the rp -process abundances are still required. The changes in this surface composition may be the cause of observed, rare super-bursts and is also thought to contribute to the surface cooling behavior of the neutron star [33].

In this work we have only measured three nuclides which are located on the rp -process path (^{90}Ru , $^{92,93}\text{Rh}$). All of the 18 nuclides presented here, however, will help refine the theoretical predictions of these masses which will in turn improve the nuclear input to the rp -process models.

The last area of the rp process where mass measurements are of interest is the endpoint of the rp -process. Tellurium is known to α decay from its ground state. This results in a cycle being set up involving Sn, Sb and Te [36]. This cycle can be seen at the end of the rp -process path shown in Figure 1.4 and in more detail in Figure 1.5. There are no new isotopes created beyond this point and so the time spent

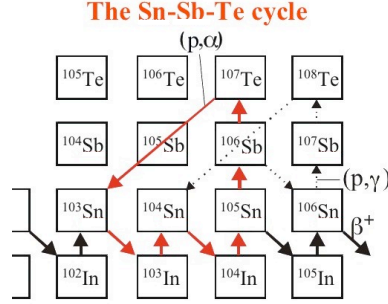


Figure 1.5: An example of an endpoint of the rp -process. Once the chain of reactions reaches ^{107}Te , alpha decays promptly return the nuclide produced to ^{104}Sn , trapping the process in a loop. [36]

both in this cycle and at each specific point becomes important for understanding the elemental abundances that result when the products of this cycle decay towards stability. These isotopes are the subject of ongoing studies with the CPT.

1.3.3 The νp -process: proton-rich nucleosynthesis in supernovae

The production of light p -nuclei, the nuclei on the proton-rich side of the valley of stability between $74 < A < 100$ not made by either the s or r processes, has never been well understood. Some p -nuclei can be produced through photo-disintegration reactions on heavy seed-nuclei produced by the s or r processes but, while this reproduces the heavy p -nuclei abundances quite well, the light p -nuclei, especially ^{92}Mo and ^{94}Mo , remain underproduced [37]. The rp process has been shown to produce these light p -nuclides but, as previously discussed, as these nuclides are not ejected back into the interstellar medium they cannot contribute to the observed solar abundances.

The production of these light p -nuclides through a p -capture process other than the rp process has not typically been thought to be possible due to the short time window available for a p -capture process in the next most likely environment: supernova explosions. The p -capture time window is only ~ 10 s, and so with the long effective half-lives of the early waiting-point nuclides such as ^{64}Ge (at $T=2.0$ GK, $t_{1/2} >$

40 s [17] or > 60 s [26]) a p -capture process in this environment cannot be expected to make nuclides heavier than $A = 64$.

The possibility of a p -capture based process creating the light p -nuclei was revived when Fröhlich *et al.* included neutrino interactions from the neutrino wind present in core-collapse supernova explosions into calculations of nucleosynthesis in the inner ejecta of core-collapse supernovae [38]. It was found that the neutrino wind creates enough free neutrons in an otherwise proton-rich environment, through the reaction



to allow neutron-capture reactions such as (n, p) and (n, γ) to take place. The addition of these two reactions dramatically reduces the effective lifetimes of waiting-point nuclides such as ^{64}Ge . Of these neutron-capture reactions the (n, p) reaction dominates, reducing the effective ^{64}Ge lifetime to ~ 0.25 s. This allows the nucleosynthetic process, dubbed the νp process, to synthesize heavier nuclei via subsequent proton capture. With an entropy per nucleon of $\sim 50 k_B$ (where k_B is the Boltzmann constant) and an electron fraction (the number of electrons per nucleon, denoted by Y_e) of $0.5 - 0.6$, it has been shown that significant quantities of ^{92}Mo and ^{94}Mo can indeed be produced [38, 39].

Since the νp process was proposed, considerable effort has been spent to better understand this reaction process, its path, and its final reaction products. One of the significant differences from the rp -process is that, due to the addition of the n -capture reactions, the νp -process path is much more sensitive to the proton separation energies (S_p) of each nuclide along the path. While the two process paths are relatively similar near the first few waiting points, as the process continues to heavier nuclides the smaller Q_p values and the resulting lower p -capture rates which are encountered result in the two paths being quite different by the time they reach masses ~ 90 . As the β -decay rates are still relatively small compared to the p -capture rates, p -capture reactions are still the dominating reaction and, except in the case of waiting point

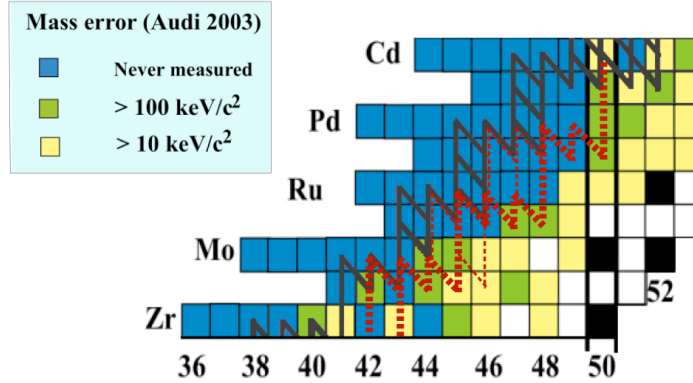


Figure 1.6: Shown here is a section of the chart of the nuclides shown in figure 1.4 which included the path of the rp process (in black, solid). Also included in this figure is the proposed νp process path (in red, dashed) as determined by Pruet *et al.* [39] and shown in greater detail by Fisker *et al.* [40]. The stronger red lines indicate the primary path of the νp reaction process, the thinner red lines indicate secondary paths of the reaction flow.

nuclides, they define the rp -process path. In the νp process however, these lower p -capture rates can become comparable to the n -capture rates which alter the path, moving it closer to stability (fig. 1.6) [39, 40, 41].

Pruet *et al.* [39] have calculated νp -process nucleosynthesis in a simulated supernova explosion of a 15 solar mass (M_{\odot}) star. Two of the six outflow trajectories studied were shown to efficiently synthesize p -nuclei with $A > 90$. Using the trajectory believed to produce the most p -nuclides, the resulting net nuclear flows were further examined by Fisker *et al.* [40, 41]. It was determined that in the νp process $\sim 90\%$ of the final ^{92}Mo abundance is a result of β decay from ^{92}Ru , and an even larger percentage of the final ^{94}Mo abundance is a result of β decay from ^{94}Pd . At νp -process temperatures, the synthesized nuclides are in equilibrium with each other with respect to (p, γ) and (γ, p) reactions, and therefore S_p values determine the relative abundances of these nuclei. The proton separation energy of ^{94}Pd , $S_p(^{94}\text{Pd})$, is expected to be large and so most ^{93}Rh , once created, quickly becomes ^{94}Pd . It is then $S_p(^{93}\text{Rh})$, which sets the ratio of created ^{93}Rh to existing ^{92}Ru , and which

will play the key role in determining the relative abundances of ^{92}Ru and ^{94}Pd and consequently the relative abundances of ^{92}Mo and ^{94}Mo . Experimentally $S_p(^{93}\text{Rh})$ was not known; instead, the value of 2.05 ± 0.50 MeV which was commonly used was determined from the extrapolated masses presented in the AME03 [21]. We have measured the two masses required to provide an experimental $S_p(^{93}\text{Rh})$ value and the results, which will be presented here, have already been published as a rapid communication in Physical Review C [18].

Due to the importance of and interest in these mass measurements other Penning trap groups have also been measuring masses in this region. The JYFLTRAP and SHIPTRAP groups joined forces and not only presented a paper including 21 nuclides between Y and Pd but also recalculated the reaction rates associated with these nuclides [42]. When they looked at how the νp -process path and abundances change when using the newly determined rates, the abundances for $^{87,88}\text{Sr}$, ^{89}Y , $^{90,91}\text{Zr}$ were the only nuclides whose production was significantly different from those calculated using rates from the mass values presented in the AME03. The reason for the change in these particular nuclides results solely from the change in $S_p(^{88}\text{Tc})$ due to their mass measurement of ^{88}Tc which, in turn, led to an increased photo-disintegration rate as compared to that calculated from the AME03 values [42]. Their $S_p(^{88}\text{Tc})$ value, however, used a mass for ^{87}Mo taken from the AME03. We have since measured ^{87}Mo and found a mass excess which falls well outside the uncertainty of the value reported in the AME03.

All 18 mass measurements of proton-rich nuclides in the region between Nb and Pd will be discussed in chapter 4 and chapter 5 along with the resulting implications for the rp and νp processes. Before looking at the results of the measurements however, the experimental techniques and the apparatus involved will be discussed. An introduction to ion traps and the Penning trap in particular will be presented in chapter 2. The remaining apparatus as well as details of the experimental technique will be discussed in chapter 3.

Chapter 2

Ion traps

The most convenient method of studying the mass of a particle with a known charge state is to measure its response to an electromagnetic field. This has been the case since the very early days of mass measurements, and was the principle behind both the positive-ray parabola apparatus and all the deflection mass spectrometers which followed [6]. This is also true in ion traps such as Penning traps, though their more compact design, high precision and high resolution have made them increasingly popular tools for precision mass measurements. Penning trap mass measurements have resulted in the highest precision mass measurements to date [9].

In order to precisely determine the mass of ions in an ion trap, isotopically pure samples of these isotopes must be created. Fusion-evaporation reactions which were used to produce the isotopes presented in this work (which will be discussed in section 3.1.1) produce many isotopes in addition to the isotopes we are interested in studying. As a result much effort is devoted to the efficient mass separation of the reaction products. We have used both Penning traps and linear radio-frequency quadrupole mass spectrometers for this purpose.

As these devices occupy such a central position in our experimental system it is important to have an understanding of the principles behind these traps as well as their various functions. This chapter will discuss their general operating principles, while Chapter 3 will discuss their specific functions in the CPT system.

2.1 Penning traps

2.1.1 Trapping potential and motion of the ions in the trap

A Penning trap confines ions using static electric and magnetic fields. The ion confinement in the radial direction comes from the motion of an ion in the magnetic field, known as the cyclotron motion. The frequency of this motion depends on the charge of the ion (q), the magnetic field strength (B), and the mass of the ion (m) and is described as follows:

$$\omega_c = \frac{qB}{m}. \quad (2.1)$$

To get confinement in the axial direction, along the direction of the magnetic field lines, an electrostatic potential is applied. Two “end-cap” electrodes with positive electric potentials are placed along the \vec{B} field axis (defined as the z -axis) and a ring electrode of negative potential is placed with the ring perpendicular to the magnetic field (figure 2.1). The potential used in our Penning trap is:

$$V = \frac{V_o(z^2 - \frac{r^2}{2})}{2d^2} \quad (2.2)$$

and is one example of a quadrupole electric potential arising from solutions to Laplace’s equation (Appendix A). Quadrupole electric fields are used as they give rise to harmonic potentials. V_o in the above equation is the potential applied to the electrodes, z and r are distances from the center of the trap to the electrodes in their respective directions and d is a geometric factor determined from z and r :

$$d = \sqrt{\frac{1}{2}(z_o^2 + \frac{r_o^2}{2})}. \quad (2.3)$$

This potential gives rise to the following \vec{E} fields:

$$\vec{E}_z = \frac{V_o \vec{z}}{d^2} \quad \vec{E}_r = \frac{V_o \vec{r}}{2d^2}. \quad (2.4)$$

The equipotential lines of this field are given in figure 2.1 along with two possible electrode configurations which can be used to establish this field.

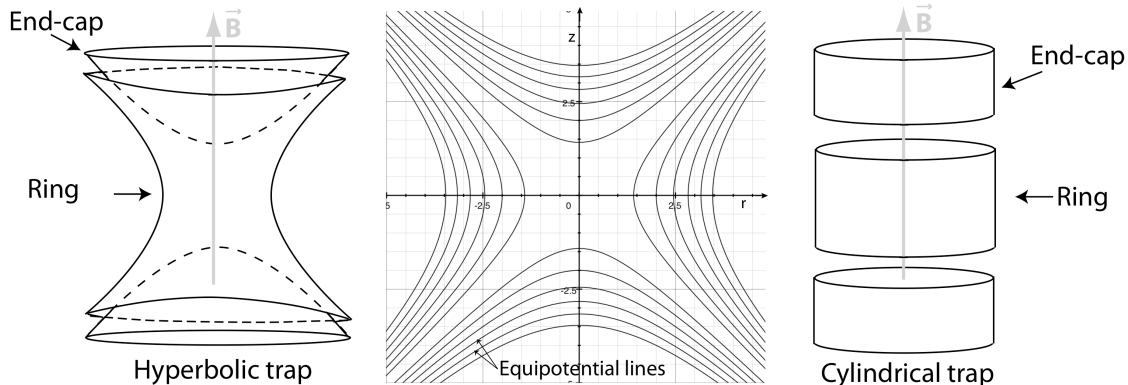


Figure 2.1: The two electrode structures which can be used to create the quadrupole electric field in the Penning trap shown above, along with an example of the field itself. Hyperbolic electrodes are used for the precision Penning trap as they more precisely define the electric field. The cylindrical electrodes are used for the gas-filled Penning trap which we use for mass selection.

It should be noted that the electric potential given above is that of an ideal trap. Practical considerations, such as the truncation of the electrodes as well as the imperfections which arise from needed modifications of the electrodes (such as adding apertures to the end-cap electrodes to permit the ions to enter and exit the trap and segmenting the ring electrode so that radio-frequency fields can be applied) will all modify this ideal field. These imperfections, the methods to correct them and the resulting effects on the ion motion will be addressed in greater detail in sections 3.3.1 and 4.2. Section 3.3.1 discusses the specific configuration of our precision Penning trap and the correction electrodes which have been added. Section 4.2 includes a discussion of all potential systematic effects, which include the effects which can arise due to perturbations in this electric potential.

Adding this electric field to the trap inevitably affects the motion of the ion inside. Only an elementary discussion of the resulting ion motion is given here. A more complete treatment is given by Brown and Gabrielse in their paper on “Geonium theory” (Geonium is defined as a single electron in a Penning trap) [43].

One additional ion motion which arises from the addition of the electric fields is

an axial periodic motion due to the harmonic potential which is applied in the axial direction. This gives rise to a simple harmonic motion of the ions along this axis with a frequency:

$$\omega_z = \sqrt{\frac{qV_o}{md^2}}. \quad (2.5)$$

The additional electric potential applied to the ring electrode of the trap results in there being two competing forces in the radial direction. As a result the motion in this plane is no longer the simple motion described by ω_c . Given a magnetic field which only has a component in the z direction, the ion motion in the radial plane is described as follows:

$$\ddot{r} = \frac{qV_o r}{2m d^2} + \frac{qB \dot{\theta}}{m}. \quad (2.6)$$

Substituting equations 2.5 and 2.1 we find:

$$\ddot{r} = \frac{\omega_z^2 r}{2} + \omega_c \dot{\theta}. \quad (2.7)$$

This is a second order differential equation which has two possible solutions:

$$\omega_{\pm} = \frac{\omega_c \pm \sqrt{\omega_c^2 - 2\omega_z^2}}{2}. \quad (2.8)$$

The two eigenmotions which now exist in the trap are labeled ω_+ and ω_- (these ion motion are shown in figure 2.2). The ω_+ motion is also known as the reduced cyclotron motion and the ω_- motion is known as the magnetron motion. These terms will be used interchangeably throughout the rest of this thesis.

If we could make mass measurements by trapping ions radially (and not have to apply the additional electric field) we could simply measure the ω_c value of the ion as by knowing this, the charge of the ion and the strength of the magnetic field we can calculate the ion mass (see equation 2.1). Fortunately, even though adding the electric field to our trap has resulted in ω_c no longer being an eigenfrequency of the system, this doesn't mean that all information about ω_c is lost. We can see from equation 2.8 that these two new eigenmotions depend on the original ω_c of the ion

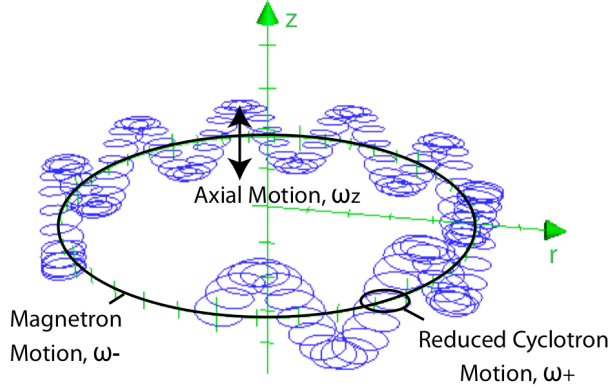


Figure 2.2: The three eigenmotions of ions in a Penning trap.

and that:

$$\omega_+ + \omega_- = \omega_c \quad (2.9)$$

If we split the ring electrode in half and apply a radio frequency (RF) excitation at exactly one of the azimuthal frequencies (ω_+ or ω_-) we can add orbital energy to the system. This provides us with a method of determining the frequencies of the ions inside. If we split the ring again and apply a quadrupole RF excitation we can add energy to the ions when the RF excitation is driven at frequencies which equal the sum of two of the eigenfrequencies. This means that by applying a quadrupole excitation to the ring electrode of the trap we can determine the frequencies of $2\omega_+$, $2\omega_-$ or, the most useful for us, $\omega_+ + \omega_- = \omega_c$.

Driving the system at the ω_c frequency couples the ω_- and ω_+ motions. When this excitation is applied, the result is not an increase in radius but a conversion of the motion from ω_- motion to ω_+ motion and back again, which cyclically adds and then removes orbital energy from the system. When the ion has purely ω_- motion it is at its least energetic as it orbits the trap at a given radius at the slow ω_- frequency. When the ion motion has been fully converted to ω_+ motion the ion is at its most energetic as it orbits the trap at the same radius but at the much faster ω_+ frequency. The change in the ion orbit as the motion is converted from ω_- motion to ω_+ motion is shown in figure 2.3. This conversion from the ω_- to ω_+ motions and the resulting

energy gain is used to determine the cyclotron frequency of the ions, which in turn enables us to determine the ions mass.

2.1.2 Mass selection in gas-filled traps

While mass selection can be applied in a Penning trap which is in an ultra high-vacuum environment (a required condition when using a Penning trap for precise mass measurements), the mass selection in this case relies on the selective excitation of unwanted contaminant ions to drive them out of the trap. Gas-filled Penning traps, in contrast, have an additional mass selective effect which allows for the global removal of all contaminant ions while selectively keeping a single ion species in the trap.

The mass selective effect which occurs in these gas-filled environments is due to the unstable equilibrium of Penning traps. Though the magnetic field provides radial confinement, the ion is still subject to the attractive electric potential in the radial direction. The equilibrium which contains the ions in the trap is only valid so long as the confining force from the motion of the ion in the magnetic field balances the outward force from this electric potential. This interplay between the attractive potential of the ring electrode and the confining magnetic force is what gives rise to the slow precession of the ions about the trap which is the magnetron motion.

In a gas-filled environment, as the ions lose energy through collisions with the gas they begin to slow down. This in turn reduces the magnetic force acting on the ions. With no electric field the motion of the ions would damp towards the center of the trap. In the presence of an outward attractive electric potential, however, as the magnetron motion of the ions is damped the ions will slowly begin to drift outwards towards the attractive potential, which increases the ω_- orbit. In short, in a gas-filled environment the ω_- motion damps outward. The reduced cyclotron motion, ω_+ , in contrast still behaves like the original ω_c motion and damps towards its center [44]. As the damping on each particular motion is proportional to the frequency of the ions

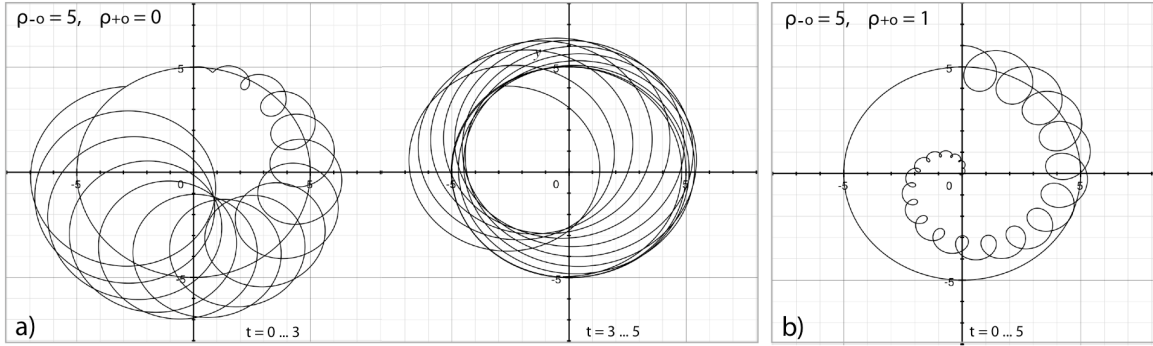


Figure 2.3: These images show the ω_- to ω_+ conversion which occurs when a quadrupole excitation at ω_c is applied in both a) high vacuum and b) gas-filled traps. Note that though the radii are different in the two cases (an initial ρ_+ value was included in b) to show the decay of the ω_+ orbit) in both cases the center of the ω_+ motion becomes centered when the motion is fully converted.

the ω_+ motion damps significantly faster than the ω_- motion. As the ω_+ motion is centered on the ω_- orbit however, the total effect of the damping is still a net outward motion.

If a quadrupole excitation at ω_c is applied, the same ω_- to ω_+ coupling and conversion occurs as in the standard high-vacuum Penning trap. The result however is that as the ω_- motion is converted to ω_+ motion and the ω_+ motion is rapidly damped. Regardless of the damping effect, the center of the magnetron motion orbit still follows the same path as in the high-vacuum Penning trap. The result is that when the ω_- motion is fully converted to ω_+ motion, the ions are centered in the trap (Fig. 2.3). Unlike in the standard Penning trap however, there is no remaining ω_+ motion to convert back to ω_- motion and so as long as the quadrupole excitation is applied the ions remain centered. Due to the strong mass dependence of ω_c , only the ions at the associated mass are re-centered in the trap. The mass resolution of the gas-filled trap in principle depends only on the resolution of the ω_c frequency.

If an additional dipole excitation at ω_- is applied, as long as more energy is added to the ions than is lost in collisions to the gas, the energy added to the ω_- motion increases the orbital radius. This ω_- dipole excitation and the quadrupole

ω_c excitation can be summed together and applied at the same time. The net result is that while all of the other ions are being removed from the trap due to their increasing ω_- radius, the ions whose masses correspond to the applied ω_c frequency are continuously being re-centered in the trap.

2.2 Linear quadrupole mass spectrometers

In contrast to the Penning trap, linear quadrupole mass spectrometers use only electric fields to confine the ions. These traps consist of alternating potentials which cyclically attract and repel the ions. As long as the frequency of the alternating polarity is rapid enough that the ions are either unable to escape the trap or reach one of the electrodes with an attractive potential before the polarity reverses, the ion will remain within the trap. Typical frequencies for confining ions are in the radio-frequency (RF) range.

When these alternating potentials are applied in 3 dimensions these devices are known as Paul traps. When only applying the alternating potentials in 2 dimensions the most common application is a linear radio-frequency quadrupole (linear RFQ). Sextupoles, octopoles and other higher order devices may also be used but they will not be included in this discussion.

2.2.1 Trapping potentials and electrode configuration

As each linear trap electrode defines one of the equipotentials of the applied field, the shape of the electrodes is set by the shape of the field that needs to be applied. The quadrupolar electric potential which arises from the easiest solution to the Laplace's equation (Appendix A) in 2 dimensions is:

$$\Phi = \frac{\Phi_o}{2r_o^2}(x^2 - y^2), \quad (2.10)$$

where r_o is the distance from the center of the trap to the inner edge of each of the electrodes, and where Φ_o is the potential between opposite rods that varies at the

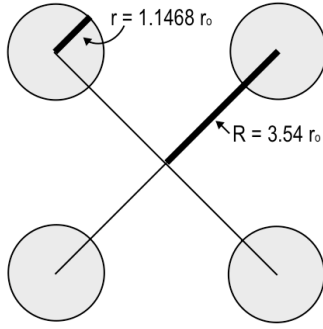


Figure 2.4: The relative size and layout for the optimal use of round rods.

appropriate frequency. To generate this hyperbolic electric potential in the xy plane four hyperbolic shaped rods are set in a square with opposite polarities applied to neighboring rods.

In practice round rods can be substituted for hyperbolic rods without significantly affecting the field near the center of the linear RFQ as long as the radius of the rods (r), is set equal to $1.1468 r_o$ and if the rods themselves are placed at a radius from the center of the trap equal to $3.54 r_o$ [45]. The resulting electrode configuration is shown in figure 2.4.

2.2.2 Stable vs. unstable orbits

Unlike the unstable equilibrium of the Penning trap which is able to confine any ion as long as it is moving, not all masses or charge states of ions are stable given the same RFQ parameters. In very general terms stability is achieved when the periodicity and amplitude of the RF field applied to the electrodes is strong enough to send diverging ions back across the center of the trap but not so strong as to create oscillations large enough for the ions to reach the rods or escape the trap. The stability of an ion then depends on its response to the applied electric fields and so ions with different masses and charge states respond differently to the same applied field.

A quantitative explanation comes from the equations of motion of the ions inside

a linear RFQ. Equations of ion motion are given by:

$$m\ddot{u} = eE_u \quad (2.11)$$

with u , here, representing either x or y and e being the charge of the ion (q , which is used in the rest of this thesis is reserved for a different variable in the discussion of the stability regions). The potential Φ_o can be a combination of both the required alternating (AC) potential as well as an optional direct (DC) potential. The form most commonly used is:

$$\Phi_o = U - V \cos \omega t \quad (2.12)$$

where U is the DC voltage and V is the peak to peak AC voltage.

We can now write the equations of motion in the xy plane as:

$$\ddot{x} + \left(\frac{e}{mr_o^2} \right) (U - V \cos(\omega t))x = 0 \quad (2.13a)$$

$$\ddot{y} - \left(\frac{e}{mr_o^2} \right) (U - V \cos(\omega t))y = 0. \quad (2.13b)$$

By performing the following substitutions,

$$a = a_x = -a_y = \frac{4eU}{m\omega^2 r_o^2} \quad (2.14a)$$

$$q = q_x = -q_y = \frac{2eV}{m\omega^2 r_o^2} \quad (2.14b)$$

$$\xi = \frac{\omega t}{2}, \quad (2.14c)$$

the equations of motion can be simplified to a single equation:

$$\frac{d^2 u}{d\xi^2} + (a - 2q \cos(2\xi))u = 0, \quad (2.15)$$

where u again represents either x or y . This is known as the Mathieu equation and its solutions can be expressed in the following form:

$$u = \alpha' e^{\mu\xi} \sum_{n=-\infty}^{\infty} C_{2n} e^{2in\xi} + \alpha'' e^{-\mu\xi} \sum_{n=-\infty}^{\infty} C_{2n} e^{-2in\xi}. \quad (2.16)$$

C_{2n} and μ are constants which depend only on the values of a and q and not on the initial conditions, whereas α' and α'' are integration constants which do depend on the initial conditions (u_o, \dot{u}_o and ξ).

Being multiplicative constants, C_{2n} , α' and α'' simply affect the overall amplitude of the motion and do not affect the nature of the motion itself. Being in the exponent, μ , however, does. The result is that the stability of the ions does not depend on the initial conditions, but only on the values of a and q .

A necessary condition for stability is that μ remains finite as ξ goes to infinity. Of the four possibilities for μ :

- 1) μ is real and non-zero,
- 2) μ is complex,
- 3) $\mu = im$ is purely imaginary with m being an integer
- 4) $\mu = i\beta$ is purely imaginary with β not being an integer,

the only of these possibilities that gives a stable solution is the last one.

The simplest approximation for β is [45]

$$\beta = \sqrt{a + \frac{q^2}{2}}, \quad (2.17)$$

though a more accurate expression (which was used to plot the stability region in figure 2.5) is:

$$\beta = \sqrt{a + \frac{(a-1)q^2}{2(a-1)^2 - q^2} - \frac{(5a+7)q^2}{32(a-1)^3(a-4)} - \frac{(9a^2 + 58a + 29)q^2}{64(a-1)^5(a-4)(a-9)}}. \quad (2.18)$$

On a plot of a vs. q the region that falls between $0 < \beta_x < 1$ and $0 < \beta_y < 1$ is known as the first stability region. Any ion that has a (q, a) coordinate that lies in this region of the graph will have a stable trajectory in the linear RFQ and therefore be trapped in the xy plane. Any ion that has a (q, a) coordinate that falls outside of this region will be unstable and lost from the trap.

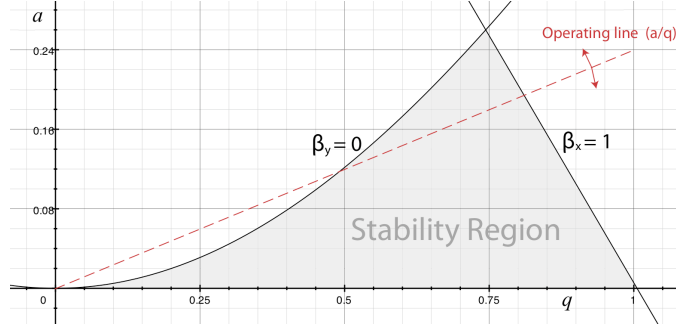


Figure 2.5: The first stability region of the RFQ shown here results from the values of β given in equation 2.18 which are based on approximations. Detailed computations have shown that q_{max} should be 0.908 and the peak of the stability diagram should be located at $q=0.70600$ and $a=0.23699$ [45].

2.2.3 Mass selection in the linear RFQ

In the previous section, 2.2.2, we saw that the values of a and q for a given ion determined whether or not it had a stable trajectory along the linear RFQ. As a linear RFQ can only have one DC potential and one AC potential at any given time and as the geometry of the trap is fixed, the values of U , V , ω and r_o are the same for ions in the trap. As a result the only parameters that give rise to different (q, a) coordinates are the different masses or charge states (equation 2.14). A linear RFQ, then, is naturally a mass selective device, which is why it is also often called a linear quadrupole mass spectrometer.

When no DC potential is applied the value for a is 0. The first stability region (shown in figure 2.5) then has a range of q from 0 to 0.92. The lightest mass which still has a stable trajectory in the RFQ can be chosen by changing the peak to peak voltage (V) and frequency (ω) of the alternating potential:

$$m_{min} = \frac{2eV}{q_{max} \omega^2 r_o^2} = \frac{2eV}{0.92 \omega^2 r_o^2} \quad (2.19)$$

In theory it would seem that all masses heavier than m_{min} should be transmitted as they all fall within the stability diagram. Masses lying at points near $q = 0$ however are all very near the edge of the stability diagram and it is possible for noise to perturb

a particle just enough that it temporarily has a (q, a) coordinate which falls outside of the stability region and results in the ion being lost. The loss of heavy mass ions will also be present if there are enough ions in the trap to generate a space-charge effect. The effect of such a space-charge is that all the ions will be subject to a net repulsive DC potential that has an effect similar to adding a direct voltage U . This will result in $a \neq 0$ and can cause the heavier masses with low q values to fall outside of the stability region.

If instead of only applying an alternating potential, Φ_o , we choose instead to use a potential which has both a DC as well as an AC component we can narrow the range of masses which have stable trajectories and thus increase the mass selectivity of the linear RFQ. Instead of all transmitted masses lying along the q -axis, the ions now lie along a line of slope a/q which is related to the applied voltages as follows:

$$\frac{a}{q} = \frac{2U}{V}. \quad (2.20)$$

This is known as the operating line.

In the x direction, the addition of a DC potential has a focusing effect. The heavier the ion the more stable a trajectory it will have. In contrast, the lighter the ion, the more easily it is affected by the AC potential and the less stable its trajectory will be in this direction. The x -direction then acts as a heavy mass filter by removing the lighter mass particles.

In the y direction we see the opposite effect as in this direction the DC potential has a defocussing effect. This defocusing is more strongly felt by the heavy mass ions as they require a much larger AC voltage to affect their motion and keep moving them back towards the center of the trap. The lighter masses however are not affected by the DC potential as the AC potential is enough to stabilize them. The y -direction then acts as a light mass filter by removing the heavier mass particles.

The amplitudes of both the alternating, V , and direct, U , components of Φ_o can be set to give a certain mass pass-band. The width of this pass band is inversely

proportional to the slope of the operating line. This pass-band is the portion of the operating line that runs through the first stability region (figure 2.5). The location of a given mass along this operating line is set by the values chosen for U , V and ω . Though a/q is proportional to U/V , even for a constant slope the values of U and V can be varied so long as their ratio remains the same. It is generally easier, however, to control the mass range transmitted by changing ω .

2.2.4 Effect of gas in the trap

If there is residual gas present in the linear RFQ the ions interact with this gas through collisions and lose energy. This interaction can be seen as a viscous drag force

$$F_d = -\frac{q}{K}v, \quad (2.21)$$

where K is the ion mobility in the gas. K is both a property of the ions as well as a property of the gas through which the ion is moving, and as such K is a measured property.

The motion of the ions in an electric field can be seen as two velocity components, the random velocity and the drift velocity of the ions (v_d) in the direction of the electric field. The proportion of each velocity component is related to the relative masses of the ions and the gas. For heavy ions and a light gas ($m_{ion} \gg m_{gas}$), which is the case in our system, the ions have the majority of their energy in drift motion. It should be kept in mind, however, that for ions with masses which are comparable to the mass of the gas used, the two velocity components will be comparable as well. In the case of a light ion in a heavier gas, the net result is actually a heating effect instead of a cooling one.

K is related to the drift velocity of the ions as follows:

$$v_d = KE, \quad (2.22)$$

where E is the magnitude of the DC electric field applied in the axial direction.

Measurements of this drift velocity are one of the methods which are used to determine the ion mobility of a given ion in a specific gas. As K varies with temperature and pressure it is generally tabulated as a “standard” or “reduced” mobility K_o which is related to K as follows:

$$K_o = \frac{p}{p_{stp}} \frac{T_{stp}}{T} K. \quad (2.23)$$

Where p and T are, respectively, the operating pressure and temperature and p_{stp} and T_{stp} are the standard pressure and standard temperature. Tables of measured K for various ions and gases can be found in [46].

When studying the ion motion in a linear RFQ the drag force given by Stokes’ Law is generally applied [45, 47]:

$$F_d = 6\pi\eta Rv, \quad (2.24)$$

where η is the viscosity of the gas and R is the radius of the ion. This added drag force from the gas modifies the equations of motion of the ions in the linear RFQ. The new equations of motion are:

$$\ddot{u} + 2k\dot{u} + (a - 2q \cos(2\xi))u = 0, \quad (2.25)$$

where $k = (6\pi\eta R)/(m\omega)$.

Making the substitutions $u = u_1 e^{-k\xi}$ and $\bar{a} = a - k^2$ results in the equation of motion:

$$\ddot{u}_1 + (\bar{a} - 2q \cos(2\xi))u_1 = 0. \quad (2.26)$$

This is again a Mathieu equation, however this time the solutions will involve an exponential term $e^{(\mu-k)\xi}$. This means that when gas is present the ion mobility also contributes to the stability of the ion motion. Similar requirements for stability exist as for the linear RFQ in vacuum and we find that:

- the ion trajectories are stable for $k > \mu > 0$
- the ion trajectories are periodic for $k = \mu > 0$
- the ion trajectories are unstable for $0 < k < \mu$.

The general effect of this added drag force is that it enlarges the boundaries of the stability region [45]

Chapter 3

The Canadian Penning Trap system

To make mass measurements of ions to high precision in a Penning trap the ion bunch delivered to the trap needs to be as pure an ion sample as possible. For high precision measurements of unstable isotopes, especially those produced using accelerated beams, the process of acquiring and purifying the ion bunch is fairly involved. The system which was used to acquire and transport these ions to the CPT is shown in figure 3.1. Instead of talking about the whole system at once, this discussion has been divided into separate sections each focusing on one or two specific aspects of the system. Whenever possible, the various elements of the system will be presented in the order in which the ion encounters them.

The first section, “3.1 Acquiring isotopes”, will discuss how the ions were produced using accelerated beams and stable targets, and how these reaction products were separated from the primary beam. The collection and cooling of the reaction products to the lower energies required by the rest of the CPT system will also be covered in this section. The second section, “3.2.2 Ion transport, mass selection and storage”, will discuss the traps other than the precision Penning trap which are also included in the system. The first of these traps increases the mass selectivity of the system whereas the second of these traps accumulates ions so that the continuous production from the beam is not lost during long measurement times in the precision trap. This

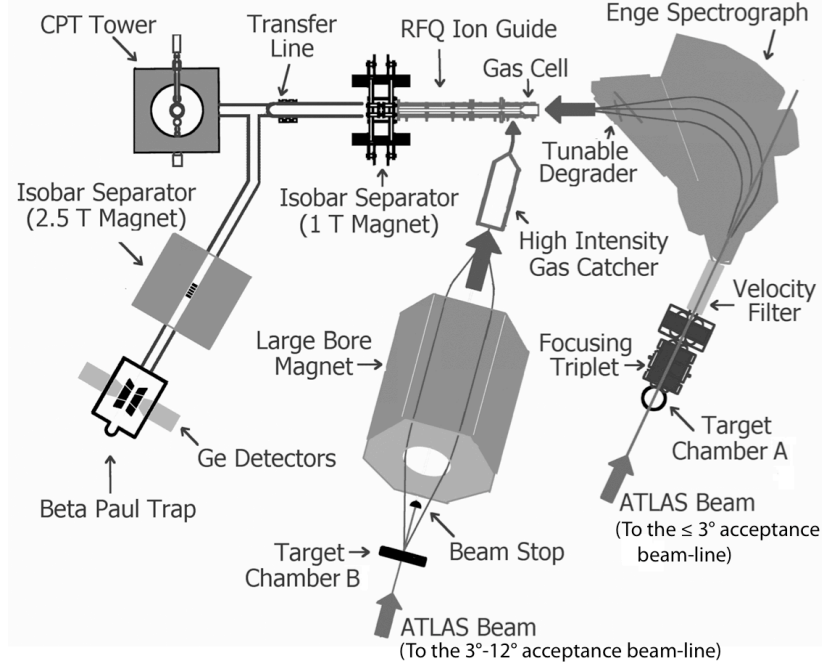


Figure 3.1: The figure above is a bird’s eye view of the layout of the CPT system. The $\leq 3^\circ$ acceptance beam-line, which includes target chamber A and the Enge spectrograph is the original beam-line of the CPT system. The 3° - 12° acceptance beam-line, which includes target chamber B and the high-intensity gas catcher, is a newer addition. The isobar separators shown have also undergone several changes which are discussed in the text (section 3.2.1). The Beta Paul Trap is not used for mass measurements but is a separate system which has been used to measure $\beta - \nu$ coincidences in ^{14}O and is currently being used to study the same correlation in ^8Li .

section will also discuss how the ions are transported from one trap to the other. The third section, “3.3 Measurement”, will build on the discussion of Penning traps in chapter 2 and discuss the specifics of the precision Penning trap. The time-of-flight (TOF) method used to determine when energy had been added to the ions through the application of an RF excitation will also be discussed along with the details of these RF excitations. A discussion of the detectors will also be included here. The last section, “3.4 System Operation”, will discuss the computer control system which was used to ensure that all the various pieces of the system work in concert. The data acquisition system and online data analysis which are included as part of this program will also be discussed.

3.1 Acquiring isotopes

3.1.1 Production

Before we can take any measurements we must first acquire the isotopes we wish to measure. There are three main sources of ions for the measurements performed with the CPT. A ^{252}Cf fission source is used to produce unstable neutron-rich nuclides, a laser ion source is used to produce ions of stable and very long-lived isotopes, and fusion-evaporation reactions using accelerated ion beams provided by the Argonne Tandem Linear Accelerator System (ATLAS) at Argonne National Laboratory are used to produce unstable proton-rich nuclides (this is known as “online operation”). As all the nuclides presented in this thesis are proton-rich, this discussion of ion production and collection techniques will focus on “online” ion production from these fusion-evaporation reactions.

When one of the ions in the accelerated beam strikes an atom in our thin target, the atoms fuse together to create a compound nucleus with a number of protons Z and number of neutrons N equal to the total number of nucleons involved in the collision. Proton-rich nuclides are created in this reaction because the proton to neutron ratio of stable isotopes decreases as the element number increases. When the two lighter stable isotopes (the beam and target isotopes) fuse together the resulting compound nucleus has fewer neutrons than the stable isotopes of the resulting element.

Due to the beam energy required to form a compound nucleus, the energy of the nucleus is much higher than its ground state energy. In addition to the production of gamma rays (γ), excess energy is carried away by protons (p), neutrons (n), and/or alpha particles (α) that are “boiled off” of the compound nucleus. The resulting reaction products all reside near the compound nucleus on the chart of the nuclides but will be a few nucleons lighter, as shown in figure 3.2. The probability that a specific nuclide will be produced can be estimated from what is known about the energy of the beam as well as the binding energies of these particles for each of

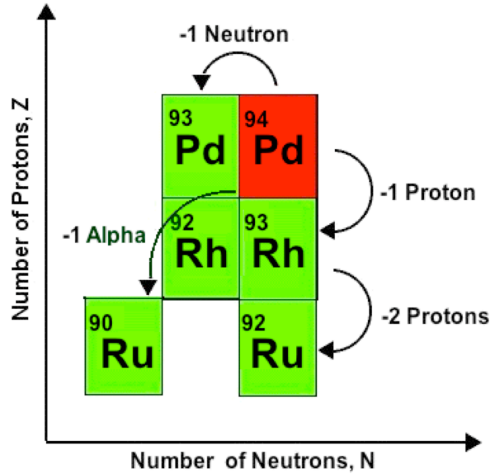


Figure 3.2: Shown in red (dark grey) is one example of a compound nucleus created through the fusion of an atom in one of our targets with an atom from the incident beam (in this case an ^{36}Ar beam and a ^{58}Ni target). Shown in green (light grey) are some of the possible recoils which result after nucleons have evaporated off the compound nucleus

the different nuclides. Programs such as PACE4 [48] are generally used for such calculations. It should be noted, however, that in regions where little production information is available these calculations can be far from reliable and are generally used as a qualitative measure of the relative production of various nuclides, rather than as a quantitative prediction. It should also be noted that as fusion-evaporation reactions require an atom from the beam to interact with an atom in the target, only a small fraction of the beam reacts and the remainder of the primary beam passes through the target unaffected. This unreacted beam will need to be separated from the reaction products.

The ATLAS facility has the capability of providing beams of any stable isotope up to uranium and so we are free to select target materials that are easy to acquire and maintain. The nuclides presented in this thesis were produced by beams hitting target foils of either natural nickel or nickel which was enriched to 99.6% ^{58}Ni . The thickness of the foils was 0.9 mg/cm^2 and 0.8 mg/cm^2 respectively. In order to dissipate the energy deposited by the beam so that higher beam intensities could be used without



Figure 3.3: The target wheel.

destroying the target, 16 target foils were mounted on a 30 cm diameter aluminium wheel which was rotated at ~ 1000 rpm [49] (Figure 3.3).

As the targets are separated from each other by spokes, a shaft encoder, which measures the angular position of the wheel, was used to generate an electronic signal which interrupted the accelerated beam whenever a spoke crossed the beam-spot. This was done to prevent undue irradiation of the target wheel. To determine the location of the spokes, the beam current downstream of the target was monitored as the current dropped significantly whenever one of the spokes crossed the beam spot. The beam current in one of the two beam-lines (the $\leq 3^\circ$ acceptance beam-line) was monitored visually by looking for changes in the intensity of the beam-spot on a scintillator which was moved into the beam path. The beam current in the other beam-line (the $3^\circ - 12^\circ$ acceptance beam-line) was monitored by using the beam-stop already included in the beam-line as a faraday cup.

When nucleons are emitted by the compound nucleus the law of conservation of momentum requires that the compound nucleus, which originally just had the momentum imparted to it by the beam, acquire a perpendicular component as well

to compensate for the mass of the ejected nucleon and the angle at which it boiled off. The resulting nuclides, known as “recoils”, emerge from the target in a cone of a certain angle. When a compound nucleus emits many particles (protons and/or neutrons) the resulting transverse momentum transfer averages close to zero and the trajectory of the recoils remains relatively close to that of the beam (within angles of ~ 0 to 3°). When an α particle boils off, however, the momentum transfer is larger and causes deviations from the beam trajectory of $\sim 3^\circ$ to $> 12^\circ$. The CPT system includes 2 separate beam-lines, each one suited to better accommodate one of these two outcomes (figure 3.1). The smaller acceptance beam-line, for use with p and n boil off, can accept ions with a maximum angular dispersion of 3° . The larger acceptance beam-line, for use when α particles are emitted, can accept an angular dispersion of $3^\circ - 12^\circ$ (with the center 3° being blocked by a beam-stop whose purpose is to eliminate the primary beam). The choice of which beam-line to use for a given experiment then depends primarily on the expected reaction channels required to produce the nuclides of interest. These beam-lines both provide a means of refocusing the reaction products and separating them from the primary beam, but as the specific methods used are different in each case they will be discussed independently.

The $\leq 3^\circ$ acceptance beam-line

After the reaction products recoiled out of the target they were focused by a magnetic quadrupole triplet. Each segment of the triplet is an individual magnetic quadrupole field which focuses the ions. The nature of these magnetic lenses is that they only focus in one of the two transverse directions (x or y) and that they defocus in the other. Using two magnetic quadrupoles, one which focuses in the x direction and the other in the y direction results in a net focusing effect. As in optical systems, the second focusing element partially undoes the focusing of the first but the resulting beam-spot is still reduced. This effect is known as strong focusing. As the resulting focus is astigmatic the third magnetic quadrupole lens is added to help improve the

focusing.

The primary unreacted beam was separated from the recoils using a combination of a Wien velocity filter and an Enge spectrograph [50]. Due to the principle of conservation of momentum the heavier reaction products had a lower velocity than the primary beam particles. A Wien velocity filter with crossed electric (E) and magnetic (B) fields was used to deflect the unreacted beam and allow the products of the reaction to enter the spectrograph. Both the current in the magnet as well as the electrostatic potential can be adjusted to select the appropriate velocity to allow the recoils of the desired mass to pass while deflecting the primary beam. The maximum electrostatic potential which can be applied across the 5 cm gap between the electrode plates is 100 kV and the maximum magnetic field which can be applied is 1500 Gauss. The estimated deflection of ~ 0.6 cm over the 70 cm length of the velocity filter is enough to prevent the primary beam from entering the Enge spectrometer.

The Enge magnetic spectrograph uses a split-pole magnet to bend the recoils and disperse them along the focal plane of the spectrograph according to momentum and charge state. The bending radius ρ of a given ion is determined by the following equation

$$B_{Enge}\rho = p/q \tag{3.1}$$

where p is the momentum of the recoil and q is its charge state. The bending radius required for the ion to reach the small gas catcher is 72 cm. We set B_{Enge} by adjusting the current in the Enge magnet, thus selecting which p/q value was directed through an energy degrader and into the gas catcher. When used in combination with the velocity filter, this results in a selection of one particular m/q where m is the mass of the ion. This charge state selection, however, reduces the efficiency of the system as the production of a particular nuclide is usually spread over several charge states.

To cool the ions from the higher energies imparted by the beam to the lower energies required to trap the ions, the ions are deposited in a volume of purified He gas which is known as a “gas catcher”. The gas catcher used in this beam-line can only

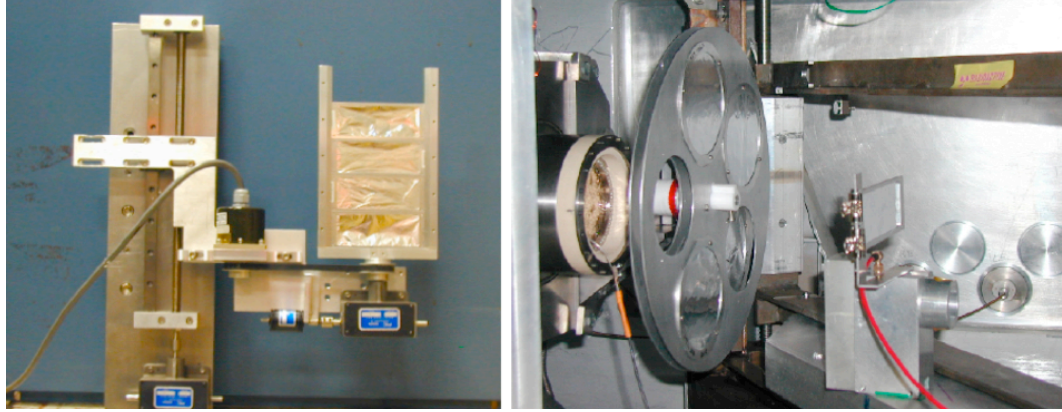


Figure 3.4: The two variable degrader systems. The image on the left shows the original variable degrader system used in experiments 1-3 (section 4.1.1). The image on the right shows the current degrader system which was used in experiment 4.

stop ions with energies $< 3 \text{ MeV}/u$ which is often lower than the incoming energies of the reaction products. As ions lose varying amounts of energy as they pass through thin foils (depending on the foil thickness and the Z of the ion) a variable degrader consisting of several thin foils of different thickness, was installed just upstream of this gas catcher. By selecting an appropriate foil thickness it is possible to reduce the energies of the incoming ions so that it can be stopped in the gas catcher. As with the rest of this system, the design of the variable degrader has evolved over the course of this work.

The first degrader system, which was used in the first 3 of the 8 experiments presented in this work (section 4.1.1), consisted of a ladder of 4 degrader foils of different thicknesses with one space open in case no degrader was required. This ladder had the additional feature in that it could be rotated slightly with respect to the incoming ions causing the ions to pass diagonally through the foil thus increasing the thickness of the chosen degrader slightly. Degrader thicknesses for the same mass range of recoils but at two different beam energies are given in Table 3.1.

In later experiments a new variable degrader system was installed. This was only used for the fourth experiment presented here (section 4.1.1) as it was the last of

Table 3.1: Example degrader thicknesses: ladder degrader

ATLAS Beam	degrader thicknesses (mg/cm ²)				
150 MeV ³⁶ Ar beam	0	0.47	0.63	0.83	1.11
130 MeV ³⁶ Ar beam	0	0.25	0.47	0.63	0.83

Table 3.2: Example degrader thicknesses: parallel wheel degrader

	degrader thicknesses (mg/cm ²)				
Wheel 1	0	0.17	0.41	0.61	0.87
Wheel 2	0	1.04	1.96	3.02	3.91

these experiments to use the $\leq 3^\circ$ beam-line. The new degrader setup consists of two parallel wheels, each able to hold 5 degrader foils. One wheel has a larger range of degrader thicknesses and the second wheel has a smaller range of thicknesses which span the range of thicknesses between the degraders on the first wheel. This allowed us to choose from 25 different degrader thicknesses in total. The degrader thicknesses which were available for experiment 4 are provided in Table 3.2. Both degrader systems can be seen in figure 3.4.

The $3^\circ - 12^\circ$ acceptance beam-line

This beam-line was added to the system in the fall of 2006 (a process in which I was involved) to take better advantage of fusion-evaporation reactions involving α -particle boil-off. This fusion-evaporation channel becomes much more common as the mass of the desired p -rich nuclide increases and is a particularly significant fusion-evaporation channel for the production of the nuclides presented in this work.

There are far fewer components in this beam-line as compared to the $\leq 3^\circ$ acceptance beam-line and this has its benefits as well as its disadvantages. As there is no charge state selection all the recoils of a given mass range are focused into the gas catcher, as opposed to just the one charge state of a single mass which was the case when using the Enge spectrograph. One drawback however is that, with no mass selection prior to the gas catcher, the gas catcher and ion guide have to be able to

handle much higher ion intensities and mass selection at later points becomes more critical.

To separate the primary beam from the recoils we took advantage of the much larger angular dispersion of the recoils compared to the primary beam. As the primary beam passes largely undeflected through the target a beam-stop which blocks ions with a dispersion of less than of $3^\circ - 4^\circ$ was sufficient to remove it. This beam-stop is simply a Faraday cup located in the center of the beam-line which is mounted on a track so that its position along the beam-line relative to the target can be adjusted, which changes its solid angle.

The sole focusing element along this beam-line is a 1 T superconducting solenoid magnet which acts as a magnetic lens, focusing the dispersing cone of recoils into the high-intensity gas catcher. This magnet has a 0.6 m bore which allows for the larger beam-pipe needed to achieve this 12° acceptance. The current in this magnet is varied depending on the mass of the recoils being studied and their energy. The whole solenoid magnet itself can also be moved along the beam-line closer to, or further from, the target depending on the dispersion cone of the recoils.

Due to the greater stopping power of the high-intensity gas catcher, and as the foil thickness of the gas catcher window is thicker than the window of the small gas catcher, a separate degrader is not required in this beam-line.

3.1.2 The gas catchers

Each beam-line has a different gas catcher whose specific design is better suited to the state of the incoming ions. Both gas catchers, however, operate under the same basic principles. The ions produced in the fusion-evaporation reactions pass through a thin window, which separates the gas volume from the high vacuum in the beam-line, and into a volume of 50-150 torr of purified He gas. Here the ions are thermalized through collisions and ionization in the gas. Once thermalized the ions are extracted from the gas catcher through a combination of RF and DC electric fields and gas flow. These

RF and DC fields are generated by voltages applied to an electrode structure placed within the closed gas catcher volume. RF fields are applied to the extraction cone and in some cases to the walls of the gas catcher to prevent the ions from reaching the inner surface of the gas catcher and being lost.

The multiply charged ions which result from the fusion-evaporation reactions undergo charge exchange and, due to the high ionization potential of He (25 eV) leave the gas catcher singly- or, more rarely, doubly-charged. Studies have demonstrated that this process is chemically independent and is efficient for even the most chemically active ions as long as appropriate DC extraction fields are used [51]. The amplitude of the RF field which is required is a function of the mobility of the ions in the gas and so higher amplitudes are needed when higher gas pressures are used. There are limits to both of these DC and RF potentials, however, as eventually breakdown can occur between the neighboring electrodes causing discharges in the gas catcher. With appropriate voltages the reaction products produced by the beam are extracted from either gas catcher, along with the He gas, as low (thermal) energy ions.

To limit potential contamination of the He gas, both gas catchers are made from ultra-high vacuum (UHV) materials.

The small gas catcher

The window of the small gas catcher is made of 1.9 mg/cm² HAVAR reinforced with a grid of gold plated tungsten wires (grid transmission is 90%). Both the window and the inner volume of the gas catcher have a diameter of 8 cm. Originally 12 electrodes connected by a resistor chain provided the DC gradient along the 27 cm length of the gas catcher. The extraction cone of the gas catcher is made of 76 parallel plates 0.43 mm thick separated by 0.5 mm mica insulators. These plates are linked by a resistor chain (to provide the DC gradient) and two capacitor chains (providing the two RF polarities). The inner diameter of the cone at its largest point matches the diameter of the gas catcher body and reduces slowly to the size of the 1.6 mm

Small Gas Catcher

	cylinder		middle	cone	
	begin	end		begin	end
DC voltages (V):	201	92	73	65	10
RF:	none		none	3505 kHz @ 0.15 V _{pp}	

Table 3.3: The DC and RF settings shown in this table were those used in experiment 4 (section 4.1.1). The cylinder and the cone each have an internal resistor chain and so the “begin” and “end” DCs are the voltages applied to either end of this chain. The “middle” electrode is an electrode that sits between the cylinder and the cone. The gas pressure used was ~ 150 torr.

extraction nozzle. Example DC and RF potentials (those used in experiment 4) can be seen in table 3.3. More details about this gas catcher are presented in a paper by Savard *et al.* [51].

The high-intensity gas catcher

The high-intensity gas catcher is a similar structure to the small gas catcher but much larger, having a diameter of 25 cm and a total length of 1.2 m. It also has an RF field applied along the body of the gas catcher, and so the electrode structure in this section is also a collection of thin plates, similar to the cone. With the larger volume, with the RF field applied to the body this gas catcher has been shown to work with ion intensities up to 1×10^9 incident ions per second [52]. The small gas catcher, in contrast, was shown to work up to ion densities of $\sim 10^8$ ion-electron pairs per cm³ per second [51].

The extraction time of the ions from the gas catcher was found to be important as radioactive molecular ions can form if the extraction times are too slow [53]. The gradient defined by the voltages presented in table 3.4 however is sufficient to limit this effect.

The construction and commissioning of this new gas catcher and its associated ion guide (section 3.1.3) was part of this thesis work.

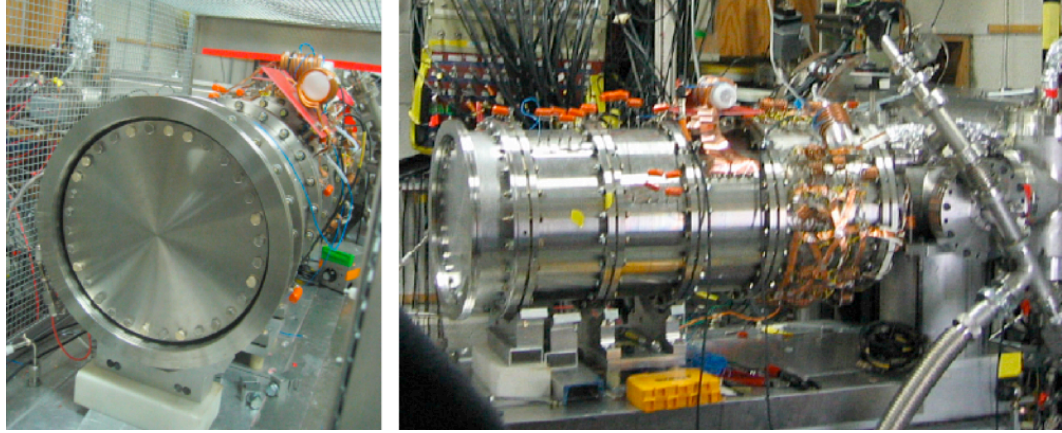


Figure 3.5: The outside of the high-intensity gas catcher is shown here. These images were taken when the ^{252}Cf source was in use. For these measurements the gas catcher window was replaced with a blank flange and the gas catcher was not connected to the ATLAS beam-line. Reconnecting the gas catcher to the ATLAS beam-line for online experiments was simply a matter of replacing the thin window and reattaching the missing section of beam-pipe.

He purification

As the extraction nozzle of both gas catchers is open to a region of higher vacuum the He gas could escape the gas catcher and so needed to be continually replaced. A manual needle valve and, in later experiments, a mass flow controller were used to regulate the gas pressure. Even when using 99.995% pure He gas it has been found that further He purification is still needed to remove the remaining water and other contaminants. Our He purification system is composed of 3 primary components. In the first stage the He gas passes through an activated charcoal filter submerged in a bath of liquid nitrogen (which has a temperature of 77 K). This step alone has proven effective in reducing the amount of H_2O present in the system. The second stage (added for experiments 7 and 8 (section 4.1.1)) is a volume of charcoal which is cooled with a cryopump to 20 - 30 K [11] and which freezes out most of the chemical elements which remain after the first cold trap. The third and final stage of purification is a commercially available Monotorr[®] purifier from SAES Pure Gas Inc. The presence of all three steps has resulted in a visible drop in the number of

High-intensity gas catcher

	cylinder		cone	
	begin	end	begin	end
DC voltages (V):	750	290	260	5.16
RF:	2814 kHz @ 0.15 V _{pp}	2157 kHz @ 0.15 V _{pp}	2348 kHz @ 0.22 V _{pp}	

Table 3.4: This table includes the DC and RF settings used for the high-intensity gas catcher in experiment 8 (section 4.1.1). The cylinder and the cone each have an internal resistor chain and so the “begin” and “end” DCs are the voltages applied to either end of the chain. Note that while the whole cylinder has a single resistor chain to set the DC gradient, it is divided into two sections with individual RF fields. The gas pressure used was 60–70 torr.

molecules that emerge from the gas catchers.

3.1.3 RFQ ion guide

Once the ions are extracted from either gas catcher they become trapped in a radio frequency quadrupole (RFQ) ion guide and, aside from the ion guide being longer when connected to the high intensity gas catcher, from this point on the ions are treated in the same manner regardless of which target chamber and beam-line were used to create and capture them.

The RFQ ion guide consists of 4 cylindrical rods of alternating electric potential, the polarity of which is switched at RF frequencies as discussed in 2.2. In short, the charged ions are alternately attracted to and repelled from each rod in turn but never with enough amplitude for them to move in one direction far enough to either reach one of the rods or escape the trap. Though the residual He gas is beginning to be pumped away the gas pressure remains high enough that there is a damping force on the trapped ions. The result is that the ions are cooled into the region of lowest electric potential, which is located along the symmetry axis of the quadrupole at the center of the ion guide. While the ions are being cooled and centered radially they are free to move axially. In fact, due to the application of a DC field gradient they are drawn away from the gas catcher and along the length of the ion guide. At the end

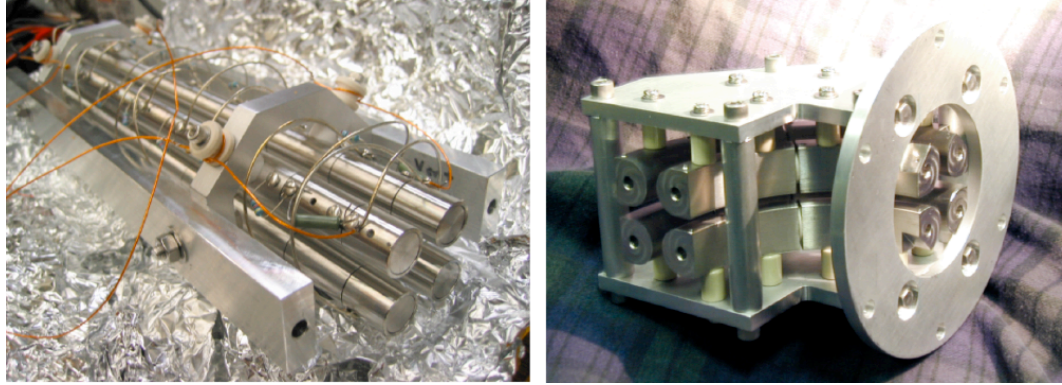


Figure 3.6: Segments of the linear RFQ ion guide. One of the straight segments is shown on the left. The linear RFQ segment shown on the right is the 90° bend which was used with the high-intensity gas catcher.

of the ion guide the continuous stream of ions which emerges from the gas catchers is collected in a small potential well. The ions are then ejected into the rest of the system in pulses, at rates from 2 to 20 Hz. The combination of the gas catchers and this RFQ ion guide has taken the high-energy, continuous beam of reaction products which results from the fusion-evaporation reactions and transformed it into the cooled, bunched beam which is required for efficient trapping.

RFQ ion guide design and settings

The ion guide is made up of three smaller sections of RFQ each separated by nozzles. The electrode structure (shown in figure 3.6) is made from 0.75" diameter rods positioned with a center to center distance of 1.40" between each pair of rods. Each length of rod is made of a collection of 0.78" long segments separated by ceramic insulators. These segments, which are connected by parallel resistor and capacitor chains, provide the DC gradient along the ion guide. A short section of a much smaller RFQ structure was also used to guide the ions into the original isobar separator (discussed in section 3.2.1) when it was in use.

The third section of the ion guide (section 3) is the same when either the small gas catcher or the high-intensity gas catcher is used, whereas the first portion of the ion

guide (section 1) is a different structure in both cases. The second section of the ion guide (section 2) used with the small gas catcher is also used with the high-intensity gas catcher but it becomes only one subsection of many which make up this section. This portion of section 2 is also known as the mass selective section as it is the only part of the ion guide which was set up to allow for a DC voltage offset between the rods.

As was discussed in section 2.2, the RFQ ion guide has an inherent mass selection based on the RF frequency which is applied and this mass selection can be enhanced by applying a static DC offset between the pairs of rods. This has proven particularly useful when using the high-intensity gas catcher beam-line as, unlike the $< 3^\circ$ acceptance beam-line, there is no mass selection prior to the collection of the ions in the gas catcher. This mass selection is instrumental in reducing the number of ions which are captured in the potential well located at the end of section 3. If too many ions are present in the well the space-charge of the ion cloud causes this small trap to saturate resulting in a loss of ions. This saturation can still occur with the mass selection applied if there are too many ions at the mass of interest, however the mass selection does ensure that a larger percentage of the ions which remain in the trap are the ions we are interested in studying.

As mentioned previously, each of the three sections is separated by a conical nozzle which has only a small aperture (2-6 mm) allowing the ions to pass between the sections. This limits the gas flow from one section of the RFQ to the next and allows for differential pumping along the length of the ion guide. The He pressure drops from ~ 3 torr in Sec 1 (in the high-intensity gas catcher case) to $\sim 2.5 \times 10^{-6}$ torr in the transfer line after the last section of the ion guide. The intermediate pressures can be seen in tables 3.5 and 3.6. It was discovered in early high-intensity gas catcher experiments that due to the larger volume associated with the longer ion guide the differential pumping was in fact too effective to allow for efficient cooling and collection in the potential well in section 3. A He gas feed was added to section 3 to keep the

	Section 1	Section 2	Section 3	Section 4
RFs:	957 kHz @ 3.8 V _{pp}	640 kHz @ 0.12 V _{pp}	608 kHz @ 0.18 V _{pp}	608 kHz @ 0.18 V _{pp}
	↔ ⊙	↔ ⊙	↔ □ □ □ ⊙	↔
DCs (V):	6 27 6	11.5 10.4 0.87 -4.5 -5.6	-0.77 -1.5 -2.6 -5.0 -2.6 7.0	3.1 3.1
ejection (V):			(80) (-80) (-80)	(-80) (-80)
pressure:	0.54 torr	0.14 torr	1.3×10 ⁻⁴ torr	

Table 3.5: RFQ ion guide settings for small gas catcher used in experiment 4 (section 4.1.1). For the DC electrodes the following symbols have been used: ↔ indicates that these two voltages are applied to either end of an internal resistor chain, ⊙ indicates the voltage applied to the nozzle between sections and □ indicates that the given voltage is applied to a single electrode (this is used to set the potential well in section 3). The ejection rate from the section 3 potential well was 550 ms and the gas catcher pressure used was ∼150 torr.

pressure around $\sim 2.4 \times 10^{-4}$ torr, which has proved optimal for ion collection.

3.2 Ion transport, mass selection and storage

Through the use of the gas catchers and the RFQ ion guide, the continuous beam of high-energy ions produced in the fusion-evaporation reactions was converted to a cooled, bunched beam. Though the beam properties out of the ion guide are sufficient for efficient capture in the precision Penning trap there are still two further steps in the CPT system prior to the ion bunches arriving at CPT. The first of these is a gas-filled Penning trap which was specifically designed to increase the mass selectivity of the CPT system. The second step involves ion collection and cooling in a linear RFQ trap. This trap both accumulates multiple ion bunches so that the continuous production of the beam is not lost when using long measurement times in the precision trap, and ensures that all ions are injected into the precision trap in the same way, regardless of which ion source is used to produce the ions.

The transport of the ions from one trap to another will also be discussed, as will the various diagnostic elements which are included along the beam-line.

	Section 1	Section 2	Section 3
RFs:	700 kHz @ 0.2 V _{pp}	800 kHz @ 0.16 V _{pp}	700 kHz @ 0.35 V _{pp}
DCs (V):	↔ ⊙	↔ ↔ ↔ ↔ ⊙	↔ □ □ □ ⊙
ejection (V):	2.5 3.1 1.0	-0.5 -0.8 -1.0 -1.1 -1.8 -3.4 4.5 3.4 -6.5 -11.5 -12.6	-7.1 -8.1 -8.5 -11.0 -8.5 0 (80) (-80) (-80)
pressure:	2.9 torr	1.2 × 10 ⁻² torr	2.0 × 10 ⁻⁴ torr

Table 3.6: RFQ ion guide setting for use with the high-intensity gas catcher. The settings shown here are from experiment 8 (section 4.1.1). For the DC electrodes the following symbols have been used: ↔ indicates that these two voltages are applied to either end of an internal resistor chain, ⊙ indicates the voltage applied to the nozzle between sections and □ indicates that the given voltage is applied to a single segment of the electrodes (this is used to set the potential well in section 3). The gas catcher pressure used was 60 torr and the ejection rate was set to 100 ms.

3.2.1 Isobar separators

It is generally the case when studying p -rich nuclides that the ions we are most interested in measuring are those with small production cross-sections. The reason for this is simple, if these ions were easy to produce they would already have been measured. Even within a single unit mass, which is the upper limit of mass selectivity available in the ion guide, there are still many isobars (ions of the same mass but different Z) present in addition to the isotope we wish to measure. For precise measurements using the precision Penning trap, however, the ion sample needs to be as pure as possible. Though there is some cleaning of these contaminants which can be applied in the CPT prior to measurement it is not sufficient to remove large quantities of contaminants. To that end additional gas-filled Penning traps have been added to the CPT system to improve the purity of the ion bunch prior to its arrival in the precision Penning trap. These gas-filled Penning traps are called “isobar separators”. The mass selective effects which occur in these gas-filled traps have already been discussed in 2.1.2.

There have been two different isobar separators which have been used over the course of the 8 experiments which will be presented here (section 4.1.1). They are

	Required resolving power ($m/\Delta m$)
neighboring masses	250
molecular ions	500 - 1000
isobars	5000 - 50000
isomers	$10^5 - 10^6$

Table 3.7: The resolving powers required to separate possible contaminants are shown here. Note that isobars near stability are closer in mass than unstable isobars and so the lower end of the range of required resolving powers is sufficient for most of the masses presented here.

1 st generation I.S.									
capture pulse(V):	(-10)	(-10)	(-8)						
DCs (V):	0.9	0.9	-0.9	-6.0	-8.0	-6.0	-1.1	1.0	19.5
ejection pulse (V):				(80)		(-80)	(-100)	(-100)	(-250)

Table 3.8: 1st generation isobar separator DC voltages, and capture and ejection pulse amplitudes from experiment 4 (section 4.1.1). The cycle time of this isobar separator was the same as the 550 ms cycle time of the ion guide. The ω_c frequency applied for ^{91}Tc with these settings was 164043 Hz @ 0.3 V_{pp} .

known as the first generation isobar separator (IS1) and the second generation isobar separator (IS2). The design and operation of these two isobar separators is sufficiently different that they will each be discussed in their own section.

1st generation isobar separator

In the first few experiments presented in this thesis (experiments 1-4) the first generation isobar separator (IS1) was used. It was located directly following the RFQ ion guide and the gas pressure in the trap was simply the residual gas still present at the end of the ion guide (between 10^{-5} and 10^{-6} torr). The electrode structure of this Penning trap (see fig. 3.7) was located inside a 1 T conventional electromagnet. Due to the lower magnetic field and the slow removal of ions from the trap through the damping of the ω_- motion, the resolving power normally achieved with this isobar separator was $m/\Delta m \simeq 1000$ (for $A = 100$). Table 3.7 provides a scale by which to determine how much resolving power is desired.

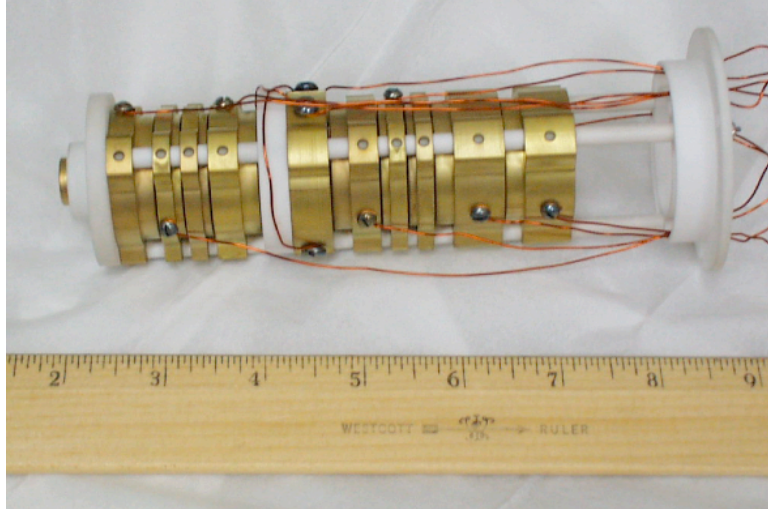


Figure 3.7: The 1st generation isobar separator electrode structure.

Unlike in the potential well in the RFQ ion guide, the confining potentials which make up the walls of the Penning trap have higher potentials than the incoming ions. This means that the potentials of the electrodes upstream from the center of the trap need to be lowered below the incoming ion energy to allow the ions to enter. The timing of the capture pulse which lowers the potentials of the upstream electrodes depends on the arrival time of the ions of interest. As the isobar separator was located so close to the end of the RFQ ion guide there was very little difference in the time-of-flight (TOF) of the ions regardless of their mass. The beginning of the capture pulse of the isobar separator was set to coincide with the ejection from the ion guide and the electrode potentials stayed lowered for as long as it took for the ions of interest to reach the trap. This time could be tuned for one mass by determining which capture pulse duration maximized the transmission of the ion of interest. Once an initial time was determined this capture time could be scaled to all other masses. The quadrupole excitation at the ω_c frequency which was used to re-center the ions of interest was only applied once the ions were captured in the trap.

When ejecting ions from the trap a negative potential was applied to the downstream electrodes and a positive pulse was applied to the upstream electrode closest

to the center of the trap. The capture and ejection pulse amplitudes as well as an example ω_c frequency are listed along with example DC voltages in table 3.8.

2nd generation isobar separator

The second generation isobar separator (IS2) is a new cylindrical Penning trap electrode structure (shown in figure 3.8) which was housed in a 7 T superconducting solenoid. In experiment 4 (section 4.1.1), the first to use this isobar separator, it was used in combination with the IS1. With the successful demonstration of this new isobar separator the IS1 was removed. In April 2007 a catastrophic quench of the 7 T superconducting magnet forced us to find a replacement magnet and so the electrode structure of the IS2 was then housed in a 2.25 T superconducting solenoid. This version of the isobar separator has been used in all of the remaining experiments presented here (experiments 5-8). Commissioning of the IS2 in both of its incarnations was part of this thesis work.

In addition to the higher magnetic field and improved electrode structure, the electronics for this new isobar separator have been set up so that a dipole excitation at the ω_- frequency can be applied resulting in a more rapid removal of the unwanted ions from the trap. This has also allowed us to apply an ω_+ excitation. At first the application of an ω_+ excitation may not seem particularly useful as this motion damps quickly to a point on the ω_- orbit and any added ω_+ energy simply gets lost in collisions with the gas (see section 2.1.2). What the addition of this excitation does however is increase the energy of the collisions with the gas and this has proven useful for breaking up molecules which arrive at the trap.

As the time-of-flight of the ions from the RFQ ion guide to the 2nd generation isobar separator is long there is a much larger difference between the capture times required for different mass ions. When using the IS2 both the beginning and the end of the capture pulse needs to be tuned and this is done by looking at the ions which are ejected back out of the trap. The pulse is originally set wider than necessary and

2 nd generation isobar separator (2.5 T magnet)						
electrode #:	1&2	3	4	5	6	7 8&9
capture pulse (V):	(-119)	(-25)				
DCs (V):	48	32	7.1	-1.5	7.1	32 48
ejection pulse (V):	(-119)	(-25)	(-60)		(120)	

Table 3.9: 2nd generation isobar separator DC voltages, and capture and ejection pulse amplitudes from experiment 8 (section 4.1.1). Sample frequencies resulting from these settings were $\omega_- = 1938$ Hz @ $0.01 V_{pp}$, $\omega_{c(87Mo)} = 397875$ Hz @ $0.10 V_{pp}$ and $\omega_{+(87Mo)} = 395919$ Hz @ $0.35 V_{pp}$.

the whole pulse is moved in time until the TOF peak of the ejected ions corresponding to the mass of interest is maximized. This tunes the stop time of the pulse as, if the pulse ends too soon the last of the ions arriving will not be able to enter the trap, and if the pulse ends too late the earliest arriving ions have enough time to reflect off of the back wall of the trap and escape before the pulse closes. The front of the pulse is then tuned by slowly moving it later in time, narrowing the pulse width. When the number of ions returned from the trap begins to decrease this indicates that the pulse is not opening early enough to allow the first of the arriving ions into the trap; the start time of the pulse is set just earlier than this time. When tuning this capture pulse an effort is made to keep the pulse length as short as possible while still letting all the ions at the mass of interest enter the trap.

The voltages applied to the electrodes and the capture and ejection pulse amplitudes used are given in table 3.9. In this table it can be seen that electrode 4 does not have a capture pulse applied even though it sits at a higher potential than the center of the trap. This is done deliberately so that multiple incoming ion bunches can be captured prior to ejection. Each bunch of incoming ions has enough energy to get over this small potential barrier when they enter but the interactions with the gas in the time between capture pulses cools the ions enough that by the time the next pulse is applied they no longer have enough energy to escape the small remaining potential well.

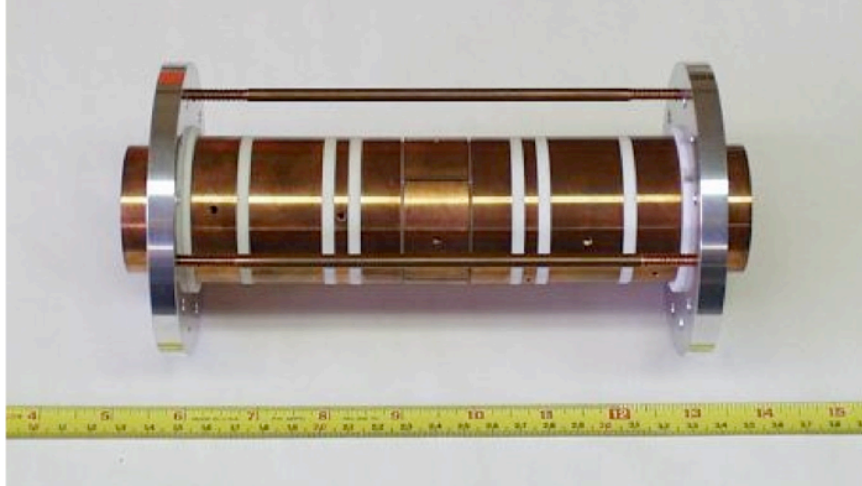


Figure 3.8: The 2nd generation isobar separator electrode structure.

Once the ions were captured in this isobar separator they were allowed to cool for ~ 8 ms before the ω_- dipole excitation was applied. This RF excitation was set to be applied for a fixed duration of cycles corresponding to approximately 20 ms. The quadrupole ω_c excitation was started shortly after the ω_- excitation and was applied for $\sim 70 - 100$ ms. After the ω_c excitation ended the ions were given another 5.5 ms to cool before they were ejected from the trap. The ω_+ dipole excitation, when used, was triggered with the ω_c excitation and was set to be applied for a set number of cycles resulting in an application time of approximately 13 ms. The resolving power we have been able to achieve with the IS2 and the 2.5 T magnet is on the order of $m/\Delta m \simeq 5000$ to 7000 (for $A \approx 84$)

Because of the location of this isobar separator, unlike the IS1, a separate gas feed is needed to provide the gas pressure in this trap. One benefit is that this allows us to optimize the gas pressure. There is no direct measure of the pressure in the trap itself but the effect of the trap pressure on the beam-line pressure gives us an indirect means of regulating the trap pressure. As the He purity can affect the lifetime of the ions in the trap a liquid nitrogen cold trap is included on this He gas line prior to the gas feed.

Due to space restrictions in the experimental area the new isobar separator could not be included in the previously existing beam-line and so a new beam-line was constructed perpendicular to the original beam-line (fig. 3.1). As the ions have to be sent back down this portion of beam-line in the opposite direction to get from the isobar separator to the precision Penning trap for measurement an additional experimental station could be added downstream of the new isobar separator. Currently an open geometry RFQ Paul trap (known as the Beta Paul Trap or BPT) is in place and is being used for $\beta - \nu$ correlation studies. With this in mind the IS2 was designed to allow for ejection in either direction from the trap.

3.2.2 Transfer line, deflection pulses and beam diagnostics

The potentials for all of the traps are kept close to 0 V to minimize the energy of the ions in the traps. When transferring the ions from one trap to another however, we would like this to occur rapidly and so after being ejected from the trap the ions are subjected to an accelerating voltage of -1490 kV which is applied to the drift tube along the transfer line. To keep the beam traveling down the desired path electrostatic deflectors and steering elements are used, and to keep the beam from dispersing electrostatic lenses are included at intervals along the transfer line. A schematic for the primary beam-line running from the RFQ ion guide to the CPT tower is given in figure 3.9 and a schematic of the beam-line built for the second generation isobar separator is given in figure 3.10.

Beam router

As the isobar separator is located on a segment of the beam-line perpendicular to the primary beam-line the ions need to travel both directions down this beam-line en-route to the precision Penning trap. As the voltages applied to the steerers and the lenses for the best tune along this portion of the beam-line are not necessarily the same in both directions, these voltages need to be switched depending on the

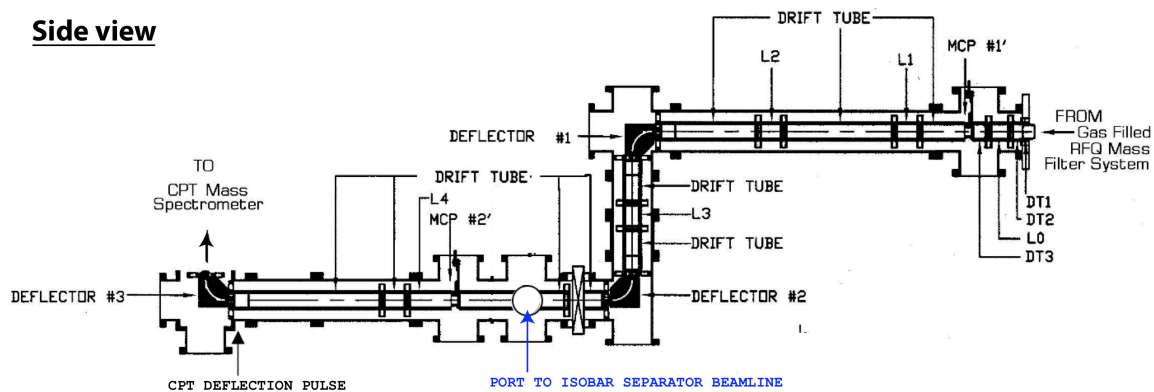


Figure 3.9: A schematic of the transfer line from the end of the RFQ ion guide to the base of the CPT tower. The port to the isobar separator beam-line is indicated and that beam-line is shown in the following figure.

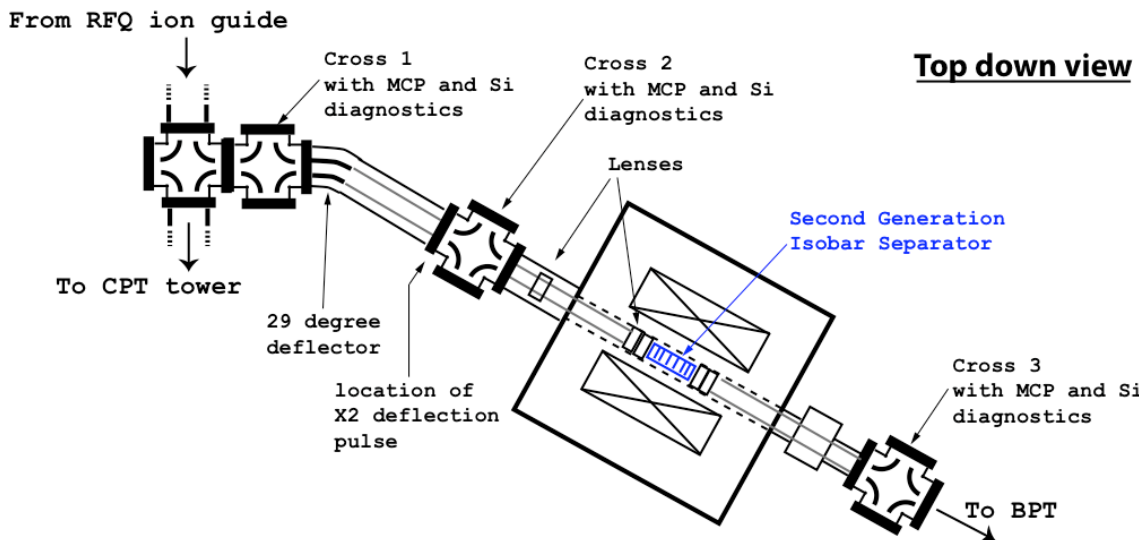


Figure 3.10: A schematic of the transfer line from the primary beam-line to the second generation isobar separator. This diagram is only approximately to scale.

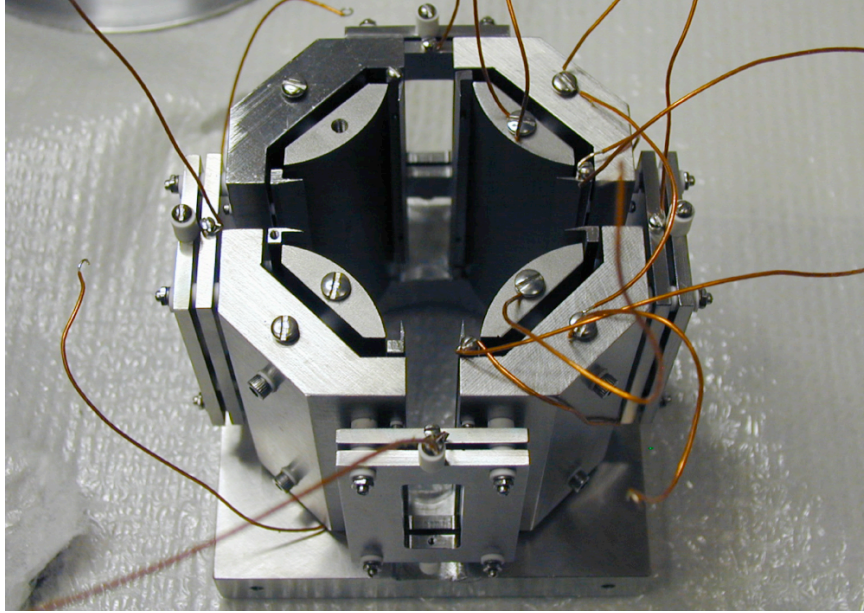


Figure 3.11: Electrostatic quadrupole deflector. The specific deflector shown is the one which directs the ions from the CPT beam-line down to the 2nd generation isobar separator and then towards the CPT tower and the precision Penning trap once the ions have been ejected from the isobar separator (it can also be set so that the ions pass through un-deflected).

direction of ion travel and on the timescales of the capture and ejection pulses of the IS2. A “beam router” box, consisting of ~ 60 mechanical high-voltage relays, is used to switch all of these voltages. The “forward” direction voltages (for ions traveling towards the IS2) are applied prior to ejection from the ion guide, and the “backward” direction voltages (for ions traveling from the IS2 towards CPT) are applied prior to ejection from the IS2.

Beam diagnostics

To help us when steering the beam down the transfer line, and to help us to optimize the transmission, various diagnostic elements such as microchannel plate (MCP) detectors and silicon surface barrier detectors have been included in the beam-line. These diagnostics also enable us to determine either which masses of ions are present in what relative quantity, or how many radioactive ions are present. The location of

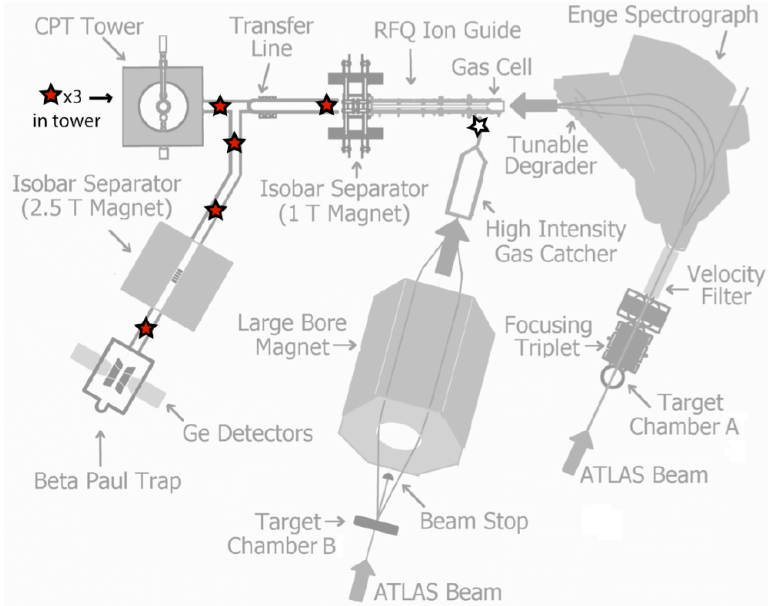


Figure 3.12: Location of diagnostic stations. Red (grey) stars indicate both MCP and Si detectors, the white star indicates a location with a Si detector only.

the diagnostic stations can be seen in figure 3.12.

The MCP detectors (which are discussed in more detail in section 3.3.3) are used for acquiring timing and counting information and record the arrival of every ion. As each bunch of ions has a precise start time (the moment of ejection from the previous trap) we can acquire time of flight information for each ion as it arrives at the MCP. This allows us to determine the relative numbers of ions at each mass and helps us tune the system for maximum transmission of the mass of interest. The MCP detectors however, cannot distinguish between stable atoms, radioactive atoms or molecules and so it provides no way of quantifying the number of short-lived reaction products arriving. To that end the Si detectors have been included. When using a Si detector the incoming ions get implanted on a foil which is located 1-2 mm in front of the Si detector. When one of these ions decays the resulting β particle passes through the foil and is detected by the energy it deposits as it passes through the detector. Counting the number of these events in a given time interval (compared to a background measurement) provides an indication of the number of radioactive ions

in the beam.

The detectors at each diagnostic station are typically attached to a mechanical arm which is lowered into the beam-line when needed. Two diagnostic stations along the IS2 beam-line, however, need to have the detectors accessible from either direction without inhibiting the beam as the ions travel in both direction down this portion of the beam-line. These MCPs and Si detectors are fixed in place parallel to the beam path and an electrostatic quadrupole deflector is set to deflect the beam so that it hits the appropriate detector. As the quadrupole deflector voltages required to reach a given detector are different depending on whether the ion is traveling “forward” or “backward” down the beam-line these voltage are also applied through the use of the beam router discussed in section 3.2.2. While most of the beam-line elements switched by the beam router only have two voltages, a “forward” voltage and a “backward” voltage the quadrupole deflectors have three: the drift tube voltage, a voltage more positive than the drift tube and one voltage more negative. Three different configurations of these voltages (given in table 3.10) can be applied by the beam router. The choice of settings applied depends on the incoming ion direction and desired destination (fig. 3.13).

	electrodes 1&3	electrodes 2&4
Drift tube voltage (no deflection)	-1490 V	-1490 V
To MCP forward or Si backward	-680 V	-2300 V
To Si forward or MCP backward	-2300 V	-680 V

Table 3.10: The three possible settings for the quadrupole deflector, depending on the desired destination for the ions and their direction of travel are shown above.

Deflection pulses

Another element included in the transfer lines are “deflection pulse” electrodes. These electrodes are set to an electric potential which deflects all the incoming ions except during a small time window chosen based on the time-of-flight of the ion species of interest. When the ions of interest arrive at the deflection electrodes, the potentials

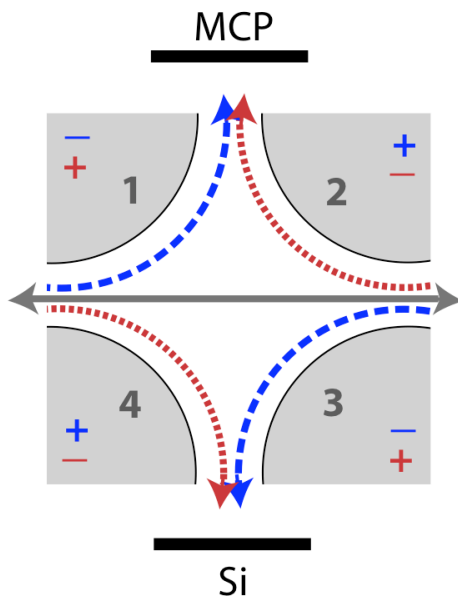


Figure 3.13: A cartoon of the quadrupole deflector to one of the MCP or Si detectors. Each colour of arrow indicates the ion path for one of the 3 voltage settings. Notice that different settings are needed to reach the same detector depending on the trajectory of the ions.

are pulsed back down to the transfer line voltages allowing only the ions arriving in that time interval to pass.

The first deflection pulse was installed before the addition of the original isobar separator and has remained even after its addition as the resolution of the IS1 did not always allow for the complete removal of the most abundant contaminants at nearby masses. Its electrode structure consists of a 1" long tube of square plates located just before the 90° bend at the base of the CPT tower (fig. 3.9). This is known as the CPT deflection pulse. Three of the plates are set to the drift tube potential while the fourth plate has a voltage that is $\sim 400\text{V}$ higher. An additional plate with a large aperture for the ions to pass through is also included. This plate is positioned perpendicular to the other 4 plates and prevents this deflection pulse voltage from affecting the ions when they are outside of the deflection pulse region. The duration of this pulse is selected so that only ions of one chosen mass unit are allowed to pass.

A second deflection pulse was added upstream of the IS2 to limit the number of

ions arriving at the trap. As this was not included in the original design of the beam-line and was added after the fact there is no special structure and the potentials and pulses are applied to a convenient set of electrodes which are part of the electrostatic quadrupole deflectors located in the second diagnostic cross along this beam-line (which has been labeled “X2”). Another difference between this deflection pulse and the CPT deflection pulse is that, instead of only a single electrode being set to a deflection voltage, two opposing plates are biased to deflection voltages, one of which is 300 V greater than the drift tube potential and the other is 300 V less. Due to the location of this deflection pulse, the spatial extent of the electrodes, and the fact that unlike the CPT deflection pulse this deflection pulse structure does not have a vertical shielding plate, the minimum mass range which can be selected with this deflection pulse is a range of 2-3 mass units.

3.2.3 Linear RFQ trap

After ejection from the isobar separator but prior to capture in the precision Penning trap, the ions are captured in a linear RFQ trap. This trap is similar in principle to the potential well at the end of the RFQ ion guide but with a more well-defined confining DC potential in the axial direction. The 10^{-4} to 10^{-5} torr of He gas which is present in this trap is maintained by a manual gas-feed. This residual gas cools the ions into the lowest potential of the trap while they wait to be transferred into the CPT (the minimum cooling time of the ions in this trap is ~ 10 ms).

The linear RFQ trap consists of four 0.75” diameter cylindrical rods with each pair of rods separated by a center to center distance of 0.65”. Each of these rods is divided into 3 segments 0.78” long which are separated by ceramic insulators. At each end of the trap additional conical end-cap electrodes are added. These end-caps each have an aperture in the center to allow the ions pass through. The deceleration electrode is seen by the ions as they approach the trap, slowing them down prior to capture. Once the capture pulse has ended the deceleration electrode then acts as an

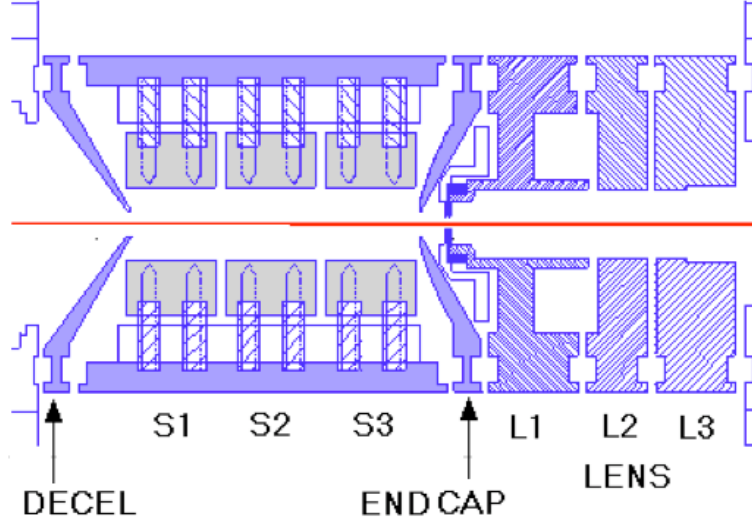


Figure 3.14: The linear RFQ trap electrode structure.

Linear RFQ Trap					
Electrodes:	Decel.	S1	S2	S3	Endcap
Capture pulse (V):	(-13.5)	(-13.5)			
DCs (V):	19.3	7.2	-3.72	7.2	20.6
Ejection pulse (V):		(168)		(-60)	(-60)

Table 3.11: Linear RFQ trap settings used in experiment 8 (section 4.1.1). The RF field applied was 750 Hz @ 0.10 V_{pp} .

end-cap electrode. A schematic of this trap is provided in figure 3.14 and its location in the CPT tower is shown in figure 3.15.

The principle of ion capture is the same here as in the case of the isobar separators: A pulse is applied to the upstream electrodes of the trap (in this case the deceleration electrode and S1) allowing the ions to enter. The pulse width is tuned to allow all ions of a single mass to enter while still closing before the earliest arriving ions have a chance to reflect from the back of the trap and escape. As this trap is used to accumulate multiple bunches of ions so that the continuous production from the beam is not lost during longer measurements in the CPT, the pulse height of the electrodes during capture is low enough to let the arriving ions enter but still high enough to maintain a small potential well to confine the previously captured ions

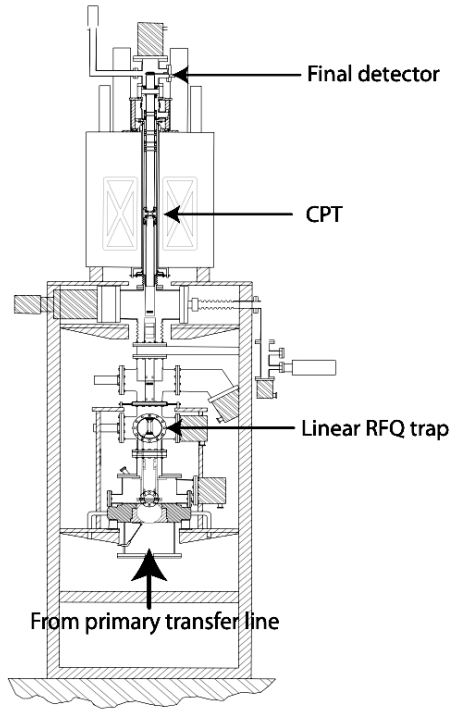


Figure 3.15: The CPT tower. The locations of the precision Penning trap, linear RFQ trap and final detector are indicated.

which will have cooled through collisions with the gas.

Ions are ejected from this trap by applying a positive pulse to electrode S1 along with the negative pulse applied to electrode S3 and the top end-cap. Due to the inevitable spatial extent of the ion cloud along the length of the trap, the ions experience slightly different potentials upon ejection depending on their location. This results in the ion bunch having both an energy and a time spread. The best conditions for capture in the precision Penning trap would be if the ion bunch had both a small time spread and a small energy spread. Unfortunately, due to conservation of phase space, any attempt to reduce the energy spread caused by the pulses upon ejection would lead to a larger time spread and vice versa. The pulse heights for the ejection pulses are chosen to provide the best compromise between the time and energy spread of the ions. At some future point we hope to improve on this further by cooling the linear RFQ trap with liquid nitrogen. This would allow for gas cooling

of the ion bunch to even lower energies in the trap and would help limit the spatial extent of the ion cloud.

After ejection from the linear trap, lenses placed along the transfer line focus the ions through 2 apertures which are included in the beam-line. These were included to limit the possible trajectories of the ions and ensure a better alignment of these ion trajectories along the magnetic field axis. This helps to minimize the orbital motion of the ions in the magnetic field which would result from an incoming ion having an additional transverse motion.

3.3 Measurement

While the basic principles of Penning traps have been discussed in section 2.1, there are many details of the electrode structure and operation which are specific to our system. Also, the technique used to determine when energy has been added to the ions through the application of an RF excitation, which has not yet been discussed, will be described here.

The ordering of this section will vary slightly from the previous sections as the discussion will not proceed exactly in the order of operations experienced by the ion. The reason for this is that an understanding of what takes place once the ions are ejected from the trap is required for a detailed discussion of the application and tuning of the various RF excitations.

This section will start with a discussion of the Penning trap electrode structure, followed by a description of the techniques for optimal capture in the trap and a discussion of the time-of-flight (TOF) of the ions which results upon ejection from the trap. Only then will the various dipole and quadrupole RF excitations, their purpose, and the techniques for determining their optimal settings be discussed. A discussion of the detectors used for the TOF measurements is included at the end of this section.

3.3.1 The precision Penning trap

The precision Penning trap is the final trap and is where the mass measurements are performed. The ring and end-cap electrodes of this Penning trap (seen in figure 3.16) are precisely machined hyperboloids of revolution so that the electric potentials applied to the electrodes create a well defined harmonic potential inside the trap. The ring electrode is split into four quadrants to allow for the application of dipolar and quadrupolar RF electric fields to drive the excitation of the ions.

As mentioned briefly in section 2.1.1, any deviations from an ideal form of the harmonic potential can lead to shifts in the measured values and other systematic effects. The finite spatial extent of the electrodes is enough to perturb the field, as are the apertures in the end-cap electrodes which allow the ions to enter and exit the trap. To reduce both of these effects correction electrodes have been added to the Penning trap structure (and are also included in figure 3.16). Correction ring electrodes have been added on both the top and bottom of the trap between the ring and end-cap electrodes. These correct for the change in the field due to the finite spatial extent of the electrodes and also correct for any anharmonic effects which arise from the splitting of the ring electrode into quadrants. Correction tube electrodes have been added outside of the end-caps around the entrance and exit apertures to limit the effect of this missing end-cap material.

As the stability of the electric field is also crucial for high precision measurements, the reference voltages from which all of the electrode potentials are generated are provided by two precision Kenwood PD 56-6AD regulated DC power supplies which are stable to 0.005% of the output voltage of 24 V. The RF excitations and the AC voltages such as the capture, ejection and evaporation pulses, are capacitively coupled to these DC voltages.

The magnetic field of the Penning trap is provided by a 5.9 T superconducting solenoid magnet. The field produced by this superconducting solenoid is both

homogeneous and extremely stable, both of which are required to reduce potential systematic errors in the mass measurements. To avoid disturbing the uniformity of this magnetic field all materials which are used need to have low magnetic susceptibility. The electrodes of the Penning trap are made of oxygen-free high-conductivity (OFHC) copper and then gold plated to reduce patch effects which can be caused by electrostatic buildup and which would alter the electric field in the trap. While the inside surface of the electrodes has been precisely machined to define the desired electric field, the outside shape of the electrodes has also been carefully chosen to best maintain the magnetic field uniformity. The beam-line, drift tubes and support structures are also made of low magnetic susceptibility, ultra-high vacuum materials such as stainless steel, OFHC copper, molybdenum and Macor[®] ceramic. The magnetic susceptibility of a material is not a constant but depends on the temperature. As such, any change in the temperature of the experimental area can potentially result in a change in the magnetic properties of the materials over the timescale of an experiment, affecting the magnetic field stability in the trap. To limit these potential effects the drift tube of the precision Penning trap is made of molybdenum instead of the more commonly used stainless steel [11]. The lower initial magnetic susceptibility of molybdenum helps to minimize these temperature dependent effects.

As the alignment of the trap in the magnetic field is critical (see section 4.2.3) the bore of the tube has been precisely machined so that the assembled trap and associated injection electrodes have the minimum amount of clearance when positioned in this tube. The tight tolerance ensures that the trap is aligned in the drift tube as any misalignment would result in it no longer fitting inside the drift tube.

To reduce ion losses in the trap and minimize other potential systematic effects the Penning trap is located in an ultra high vacuum (UHV) environment. Typical pressures achieved in the precision Penning trap portion of the beam-line are on the order of 4.8×10^{-10} torr.

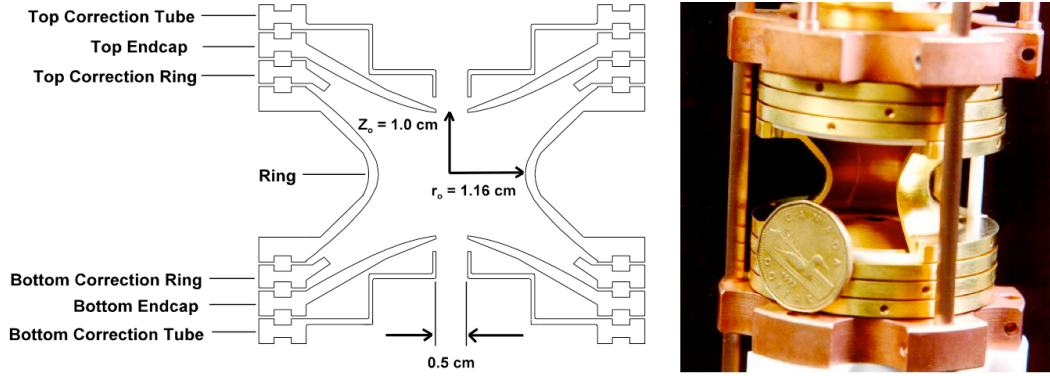


Figure 3.16: CPT electrodes. On the left is a schematic showing the electrodes, their placement and relative sizes. On the right is a photo of the trap with one quadrant of the ring electrode removed. The Canadian \$1.00 coin (the Loonie), which has a diameter of 2.65 cm, is included to provide a sense of scale.

Penning trap electrodes	DC voltages (V)
Tof A:	-10.421
Top correction tube:	0.300
Top endcap:	-2.797
Top correction ring:	-8.241
Ring:	-12.323
Bottom correction ring:	-8.240
Bottom endcap:	-2.805
Bottom correction tube:	0.300
Top decel:	-14.965

Table 3.12: DC Electric potentials applied to the electrodes of the precision Penning trap.

Techniques for capture

To ensure that the ions captured in each trap have as little kinetic energy as possible the electric potential energies of the ions in the traps are maintained at similar potentials. This requirement is particularly critical in the case of the precision Penning trap as, unlike all of the other traps, there is almost no residual gas present to damp the motion of the ions. Minimizing the kinetic energy of the ions minimizes the initial amplitudes of the ion motions in the trap and ensures that the ions sample a small region of the almost ideal electric and magnetic fields which exist near the center of

the trap.

The DC voltage on the ring electrode of the trap, which sets the lowest potential of the trap, needs to be carefully chosen so that the ions which are captured are as close to rest as possible. To determine the optimal value of the potential applied to the ring electrode all of the electrodes of the trap are tied to a single voltage which (in combination with the magnetic field) is used as a retardation lens. The initial value for this potential is chosen to be low enough that all of the ions ejected from the linear RFQ trap simply fly through the precision Penning trap. The voltage is then raised slowly until the number of transmitted ions begins to decrease, indicating that the voltage has reached a value which corresponds to the lowest energy ions in the bunch. This is then the voltage which gets applied to the ring electrode once the trap is set back to the trapping potentials.

This “fly-through” method is also used to tune the steering of the ions into the trap as ions which have a transverse component of velocity in the magnetic field have less axial energy and are the first to be stopped by the potential hill created by the electrodes. The steering is tuned to maximize the number of ions seen on the final detector, which is equivalent to maximizing the axial energy of the ions. The potential of the trap is then raised slightly and the process is repeated, fine tuning the steering.

If the lowest electric potential of the trap corresponds to the energy of the ion bunch, the trapping potentials which define the walls of the trap are too high to allow the ions to enter and have to be lowered to (or below) the ring electrode voltage by a capture pulse. Methods of tuning the capture pulse timing have already been discussed for the gas-filled Penning trap and the linear RFQ trap but, while these principles apply here, there are additional factors to take into consideration. While ensuring that the pulse begins soon enough to allow the ions of interest to enter, and ends soon enough that the ions do not have a chance to reflect back out of the trap, we also need to ensure that no additional energy is added to the ions when the capture pulse closes. If the capture pulse closes too soon or too late it can add kinetic

energy to any ions which are in the region of the bottom end-cap electrode. The optimal capture time would be to close the trap when the ion bunch is as far from the bottom electrodes as possible. To determine the optimal capture time in practice we tune it by monitoring the time-of-flight of unexcited ions ejected from the trap as a function of various capture times. If additional energy is being added to the ions by the capture pulse the average TOF of the ions will be shorter.

The final means of limiting the energies of the ions in the trap is to apply an “evaporation pulse” to the top electrodes of the trap. Shortly after the end of the capture pulse the potentials applied to the top end-cap and correction tube electrodes are lowered slightly to allow the highest energy ions to escape. Tuning the trap for optimal capture is still the preferred method of limiting the ion energies, however, as the loss of ions during the evaporation pulse reduces the number of ions available for measurement.

Ejection and time-of-flight measurements

Though there are several different RF excitations which are applied to the precision Penning trap between the capture and ejection of each ion bunch, a discussion of the time-of-flight techniques used to determine when energy has been added to the ions will be presented first. The RF excitations will be discussed in detail in the section [3.3.2](#) which follows this one.

A heavy ion detector with good timing characteristics (discussed further in section [3.3.3](#)) is used to determine the number of ions ejected from the trap and their TOF. This information is used to determine when an applied RF excitation has added energy to the ions. In the case of dipole RF excitations this can be determined by monitoring the number of ions detected as a function of the applied frequency. When the applied frequency of the dipole excitation matches either the ω_+ or ω_- frequencies energy is added to the ions and their orbital radius increases until they can no longer

escape through the 5 mm aperture in the top end-cap electrode.

In the case of a quadrupole RF excitation, when the applied frequency matches the ω_c frequency of the ions, energy is added to the system without increasing the radius of the orbit (see section 2.1.1). The increased energy in this orbital motion contributes to the linear kinetic energy of the ions once ejected from the trap and results in a shorter TOF to the detector. This occurs due to the interaction of the electric dipole of the orbiting ion with the magnetic field gradient in the fringe field of the magnet.

For any ion in the trap (not just ions which have been excited) this electric dipole is characterized by the magnetic moment, $\vec{\mu}$ which is given by:

$$\vec{\mu} = \frac{E_r}{B_o} \hat{z}, \quad (3.2)$$

where E_r is the radial energy of the ion, and B_o is the volume of the magnetic field within the ion orbit. When the electric dipole passes through the magnetic field gradient the force along the axial direction is given by:

$$\vec{F} = -\vec{\nabla}(\vec{\mu}_i \cdot \vec{B}_o) \Rightarrow -\mu_i \frac{\partial B}{\partial z} \hat{z}. \quad (3.3)$$

The resulting axial energy is combined with the ejection energy of the ion and is what determines its TOF.

When a quadrupole RF excitation is applied and the frequency (ω_D) matches the cyclotron frequency of the ions, additional radial energy is added to the system. Given a total energy in this case of $E_{r(\omega_D=\omega_c)}$ which is greater than the energy in the case of unexcited ions $E_{r(\omega_D \neq \omega_c)}$, we find the resulting force $\vec{F}_{(\omega_D=\omega_c)}$ is greater as well. This increase in the orbital energy of the ions results in an increase in the axial energy, which in turn results in a shorter TOF to the final detector. The more orbital energy is added to the ions, the shorter a time it will take the ions to reach the trap, and the larger the TOF difference between the excited and unexcited ions.

Our data then consists of a series of different TOF measurements each for a specific applied RF frequency. The applied frequency is varied for each ion bunch captured in

the trap and the applied frequencies sweep over a range which is expected to include the ω_c frequency of the ion of interest. The data associated with each ion bunch at a particular frequency is called a “point”, a collection of points which cover the entire frequency region being studied is called a “scan”, and each “run” is a collection of many scans. The number of scans required for a given measurement depends on the number of ions per shot in the trap, the desired precision of the measurement, and the percentage of ions in the trap which are contaminant ions and not the ions of interest. The reasons for this will be discussed in greater detail in section 3.4.3. To determine the ω_c frequency of the ions the average TOF of each point is plotted versus the applied frequency. When the applied frequency matches the ω_c frequency of the ions, there will be a minimum in the TOF spectrum (See Fig 3.18).

To provide a long time-of-flight path to allow for more dispersion between the excited and non-excited ions the ejection pulse for the CPT is different from the ejection pulses for the other traps. In this case only the top electrodes of the trap are pulsed down and no positive pulse is applied to the upstream electrodes. While there is an accelerating gradient along the beam-line (as it is needed to allow for ion focusing) the slope of this gradient (given in table 3.13) is deliberately shallow.

As many of the TOF drift tubes lie within the CPT magnet and its fringe field the materials used for this TOF drift tube are all materials with low magnetic susceptibility. The electrode known as TOF A, which sits closest to the Penning trap, is made of gold plated OFHC copper, similar to the Penning trap electrodes (the gold plating reduces possible surface charge which could affect the electric field in the Penning trap). Electrodes TOF B, C, D, E & F are made of OFHC copper but without the gold plating. All of the remaining TOF electrodes are made of stainless steel. A schematic of this electrode structure can be seen in figure 3.17.

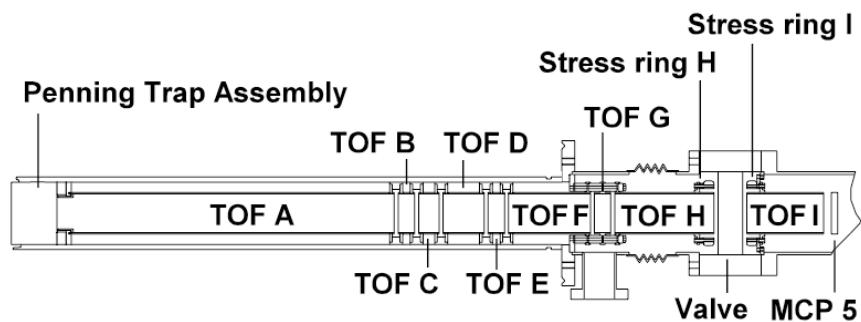


Figure 3.17: TOF drift tube schematic.

3.3.2 Dipole and quadrupole RF excitations

Dipole RF excitations at ω_- and ω_+ frequencies

Once the ions are captured in the trap and after the high energy ions are removed, the first of a sequence of RF excitations is applied to the ring electrode of the trap. This is also the last mass selective “cleaning” step prior to measurement. Dipole excitations at certain selected ω_+ frequencies corresponding to possible contaminant ions are applied to the trap. As the ω_+ frequency is highly mass dependent these RF excitations mass selectively excite any unwanted ions that may have made it passed the isobar separators out of the trap. While some ω_+ frequencies were determined before the experiments (for example, the ω_+ frequencies of any isobars known to be produced in the fusion evaporation reaction) there are occasionally other molecules (typically hydrocarbons) which are found to be present. Broad scans of a range of ω_+ frequencies were done to identify these possible contaminant ions and the contaminant ω_+ frequencies were determined by monitoring the number of ions ejected from the trap as a function of the applied dipole excitation frequency. When the applied frequency matches the ω_+ frequency of one species of contaminant ion they are driven to ever larger orbits and are lost from the trap, resulting in a drop in the number of ions seen on the final detector.

To maximize the number of ion species that can be cleaned while reducing the total

TOF electrodes	Voltage (V)	
	for MCP	for channeltron
A:	-10.40	-10.42
B:	-100	-100
C:	-300	-300
D:	-500	-500
E:	-700	-600
F:	-900	-300
G:	-450	-810
H:	-900	-1500
H stress:	-900	-300
I stress:	-500	-1500
I:	-900	-300

Table 3.13: TOF drift tube voltages when using the MCP (experiments 1-7 (section 4.1.1), experiment 7 shown here) or when using the channeltron (experiment 8)(the channeltron requires more focusing).

ω_+ cleaning time a Tabor arbitrary waveform generator (model WW1071) is used. It is capable of generating complex waveforms and can apply a waveform which is the sum of all of the various ω_+ frequencies. This pulse is then applied for anywhere from 100 to 300 ms depending on the ω_+ resolution required, which in turn depends on how close the nearest contaminant is to the ion of interest. Prior to the installation of the Tabor arbitrary waveform generator (experiments 1-3, (section 4.1.1)) only the 3 most abundant contaminants were cleaned by applying their individual ω_+ frequencies in sequence. The addition of this arbitrary waveform generator has allowed for the removal of many contaminant ion species in the time previously used for a single species. This is particularly useful when studying short-lived nuclides where long preparation times can result in decay losses in the trap and can limit the maximum precision of the measurements (this will be discussed further in chapter 4).

At the end of the cleaning process we are left with a very pure sample of the ions of interest, which are still almost at rest in the center of the trap. Even when almost at rest the two azimuthal ion motions are still present. The ω_+ motion has an initial radius, $r_{o,+}$ and the ω_- motion has an initial radius of $r_{o,-}$. With careful injection

(described earlier) the radius of the ω_+ motion can be minimized and is found to be much smaller than the initial radius of the ω_- motion.

When a ω_c quadrupole RF excitation is applied, the ion motion gets cyclically converted from ω_- motion to ω_+ motion and back again. At its most energetic, when the motion has been entirely converted to ω_+ motion, the kinetic energy gain in the orbital motion is given by [54]:

$$\Delta E_r = \frac{m}{2}(\omega_+^2 - \omega_-^2)(r_{-,o}^2 - r_{+,o}^2). \quad (3.4)$$

As $r_{\pm,o}$ are the initial radii of the respective motions, we see that starting with a large radius for the ω_- motion and a small radius for the ω_+ motion allows for the largest energy transfer to the ions. To achieve a larger initial radius for the ω_- motion, and thus increase this energy gain further, a dipole RF excitation at the ω_- frequency is applied prior to the quadrupole RF excitation at ω_c . As the ω_- motion is almost mass independent this dipole excitation drives all of the ions into a larger initial ω_- orbit. This excitation was applied for 40 ms at an amplitude of 0.016 V_{pp} on the Stanford Research Systems DS345 function generator which provides this ω_- RF excitation. These values were determined by varying the amplitude for successive ion bunches and noting at which amplitude the ω_- orbit became too large for the ions to escape through the 5 mm diameter aperture in the top end-cap. This determined the amplitude required to position the ions in the maximum initial radius $r_{o,-}$. This allows for the largest energy gain upon conversion from ω_- motion to ω_+ motion.

The outputs from the function generator which provided the ω_- RF excitation and the Tabor arbitrary waveform generator which provides the ω_+ RF excitation were summed and a phase splitter was used to generate opposite phases of this summed signal. A set of relays under computer control then selected the appropriate phase to apply to each segment of the ring electrode.

Quadrupole RF excitations around the ω_c frequency

Following the two dipole excitations which prepare the ions in the trap, a quadrupole RF excitation is applied. As already discussed, when the applied frequency matches the ω_c frequency of the ions the ion motion is cyclically converted from ω_- motion to ω_+ motion and back again. As the ions have the maximum energy when fully converted to ω_+ motion the amplitude and the time of the applied ω_c excitation are chosen such that the applied excitation ends when ions are fully converted to ω_+ motion. The required amplitude to achieve a full conversion in a given excitation time is:

$$T_{conv} V_{RF} = \frac{B r_o^2 \pi (\omega_+ - \omega_-)}{2 \omega_c}, \quad (3.5)$$

where T_{conv} is the time required to fully convert the ions when using an applied amplitude V_{RF} . B is the strength of the magnetic field and r_o is the radius from the center of the trap to the innermost edge of the ring electrode. Note that because ω_- is small compared to ω_+ and ω_c the value for $\frac{(\omega_+ - \omega_-)}{\omega_c}$ is close to 1 and so this relationship is only weakly mass dependent [54].

The amplitude, V_{RF} , for any given excitation time can be tuned by taking several short runs of a highly produced ion species (typically our calibrant ion) at various amplitudes and monitoring the TOF difference between the excited and unexcited ions. When this TOF difference is largest the chosen amplitude corresponds to a full conversion of the ion motion. An additional tuning technique is to double the applied amplitude. This results in a TOF spectrum which has no TOF minima at the ω_c value but instead has two minima, which should be symmetric, on either side of ω_c . Tuning the amplitude so that these two peaks are as symmetrical as possible optimizes the value of $2V_{RF}$.

The RF excitation for the ω_c excitation is provided by a Stanford Research Systems DS345 function generator which includes an additional, precise 10MHz internal clock which increases the frequency stability of the function generator to 1 ppb per day

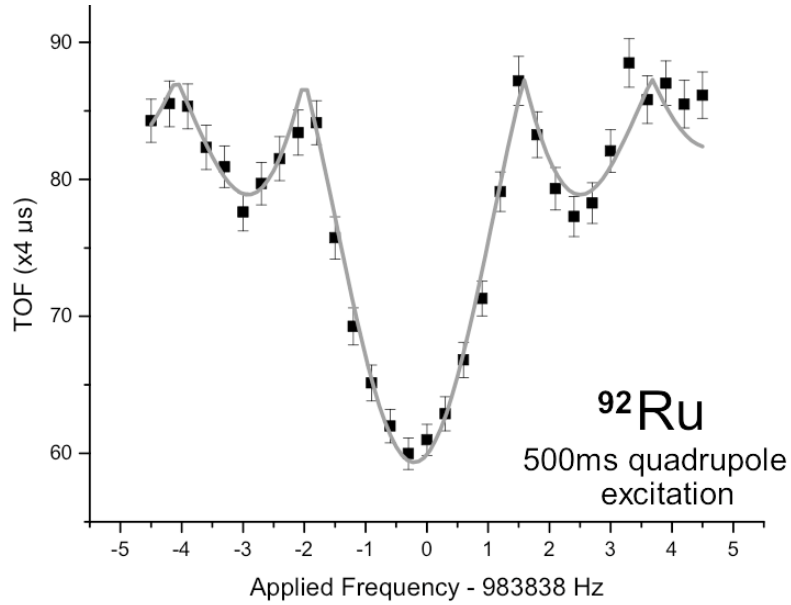


Figure 3.18: This sample TOF spectrum of ^{92}Ru used a 500 ms quadrupole RF excitation time. The curve shown is the best fit of the theoretical line shape to the data. The fitting function used here was a “modified sinc” function given in equation 3.13.

(this internal clock is also used as a reference time-base for all of the other function generators which provide RF frequencies for the precision Penning trap). As with the ω_- and ω_+ excitations, this signal was sent to the phase splitter and then to the computer controlled relays which, for a quadrupole excitation, applied opposite phases of the RF excitation to neighboring ring segments.

3.3.3 Ion detection

At the end of the TOF drift tube is a heavy-ion detector (either a MCP detector or a channel electron multiplier) which provides the “stop” time for the TOF measurements (the “start” time having been the ejection from the CPT). The requirements for this detector include the ability to detect an incoming ion, good time resolution (the ability to detect multiple ions in a $\lesssim 1\mu\text{s}$ time window) and a low background rate. A high detection efficiency is also desired but timing and background considerations are more important. For the first 7 of the 8 experiments an MCP detector

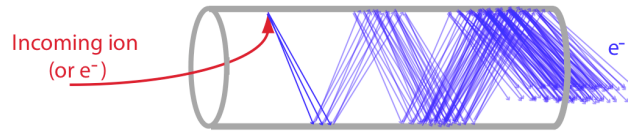


Figure 3.19: Electron multiplication in MCPs and channeltrons.

was used. Prior to experiment 8 (section 4.1.1) however it was replaced by a channel electron multiplier (which is often called a channeltron).

Both MCP detectors and channeltrons are based on the same method of converting an incoming particle into an electronic signal and differ mostly in their implementation. This basic method involves a channel whose walls are usually made of lead glass and which is then coated with a semi-conductor material. There are metal electrodes at either end of the channel and a voltage gradient is applied across it. When an ion enters the channel and hits the channel wall secondary electrons are produced and in greater number than the original particle. These electrons are then accelerated along the channel by the applied voltage gradient and produce more electrons every time they strike the wall (this is shown in figure 3.19). The resulting “avalanche” of electrons is then read out as either a distinct pulse or as a continuous current depending on the rate of arriving ions. In the CPT system both detectors were operated in the pulse counting mode.

Microchannel plate detector

MCP detectors have been named appropriately as they are a plate (or stack of plates) of very small, μm diameter channels which have been grouped together. The MCP which was used in the CPT system had an active area of 40 mm which consisted of a collection of 10 μm channels separated by center to center distances of 12 μm . To insure that ions impacted the walls of the channel and did not manage to simply fly through, the channels were angled 8° from the normal of the plate. This MCP

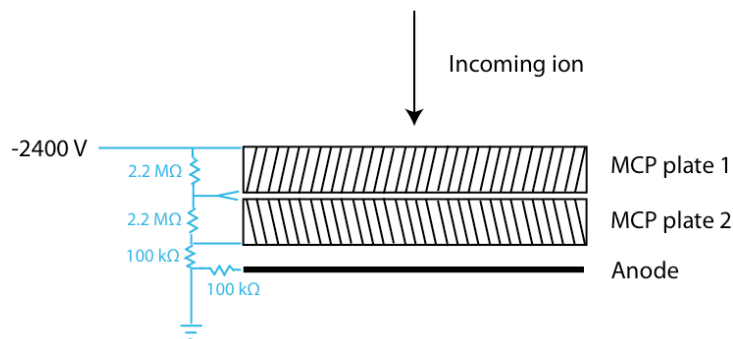


Figure 3.20: Schematic of the MCP detector.

contained two such plates which were stacked together in a chevron configuration to increase the gain of the detector. One drawback to the MCP detector was that, due to the spacing between channels only about 50% of the MCP surface was active. The best detector efficiency we could expect was also $\sim 50\%$. The circuit and voltages applied to this MCP are shown in figure 3.20. A bias was applied across each MCP plate and created a positive potential which accelerated the resulting electrons from the front of the first MCP plate to the detection anode. The voltages applied to this MCP are provided by a single channel on a high voltage power supply which is sent through a voltage divider.

Channeltron detector

Channeltron detectors are single channels about 1 mm in diameter and about 2-5 inches long. To increase the collection area the incident end of the channel is expanded into a ~ 1 cm diameter cone and the electrons produced in this collector region then are accelerated into the channel by the applied electric fields. The collection area of the channeltron is much smaller than the MCP and so additional focusing of the ions along the TOF path is required. One potential drawback is that the time resolution of the channeltron is around 100 times less than is possible with a MCP detector. As this still provides a ~ 20 ns resolution, and given the typically small number of ions per bunch, this should not adversely impact its performance. One benefit of the

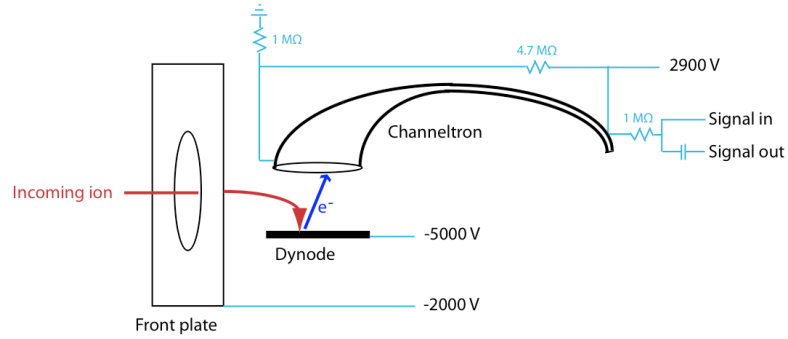


Figure 3.21: Schematic of the channeltron detector.

channeltron is that the whole surface is active and so the detection efficiency should be greatly improved over the MCP. The channeltron circuit and applied voltages can be seen in figure 3.21.

3.4 System operation

A software program called the “online program” controls many of the aspects of the CPT system during data taking. This program performs the functions of initializing the system parameters, controlling the measurement process, acquiring and storing the data, and performing online analysis. This online program has also undergone many changes over time. Its original form is documented extensively in the thesis by Jason Clark [49] and so only the most recent version of the program will be discussed here. However, an effort will be made to indicate new features and changes.

3.4.1 Timing control system and RF frequency settings

One of the primary functions of the online program is to initialize the timing settings for all of the capture pulses, ejection pulses, and deflection pulses as well as to set all of the RF excitation times. These time values are loaded from parameter files generated by the operator in a separate program. Each ion species requires its own parameter file, but as the TOF of the ions and their frequencies in the various traps

are directly related to their mass, all of these values can be scaled from previously determined timings. Also included in this parameter file and loaded by the program are the frequencies and amplitudes of the RF fields or RF excitations applied to all 3 traps.

As the capture pulses of the various traps need to be precisely timed after the ejection from the previous trap, precision digital delays (DG11A Digital Delay generators from the Data Design Corporation) are used. The timing of the deflection pulses are also set by these digital delays to allow for the narrow pulse width required to select a narrow mass range. For the duration of the RF excitations in each trap, which only need to be accurate on the order of ms, Jorway 221 Timing and Sequencing modules are used. All of the delay modules are located in a single CAMAC crate which is connected to the computer running the online program.

There are currently three DG11A modules which are used in the current version of our timing system and they control:

- 1) The RFQ ion guide ejection pulse, the X2 deflection pulse, and the IS2 capture pulse
- 2) The IS2 ejection pulse, the CPT deflection pulse, and the linear RFQ trap capture pulse
- 3) The linear RFQ trap ejection pulse and the CPT capture pulse.

There are two Jorway 221 modules in the timing system and they control:

- A) The ω_- and ω_c excitations in the IS2
- B) The evaporation pulse, and the three RF excitations applied to the ring electrode of the CPT.

In experiments 1, 2 and 3 (section 4.1.1), when the IS2 was not present in the system, only two DG11A modules were used: one to control the ejection from the IS1 and the capture in the linear RFQ trap, and one to control the ejection of the linear RFQ trap and the capture in the Penning trap. The 4th experiment, which used both the IS1 and IS2, used the three DG11A modules listed above but the IS1 ejection pulse

was used in place of the RFQ ion guide ejection pulse.

To take advantage of the continuous production from the beam while measurements are being done in the CPT each trap is used simultaneously. Both the IS2 and the linear RFQ trap are able to accumulate multiple bunches of ions and so the ejection from the ion guide can occur more frequently than the capture cycle in the CPT (the IS2 can be set to capture a certain number of shots (M) prior to its ejection towards the linear trap and the linear RFQ trap can be set to capture a certain number of shots (N) prior to ejection towards the CPT). To ensure that these separate timings do not cause a loss of ions due to one trap ejecting when another is not prepared to capture, a feedback system is set up based on the following considerations:

i) The RFQ ion guide ejection and IS2 capture pulses require both a signal from a master clock, and a signal indicating that the linear RFQ trap is “ready” (i.e. has captured fewer than N shots).

ii) The IS2 ejection and linear RFQ trap capture pulses require the IS2 to have already captured M shots and require a signal indicating the linear RFQ trap is “ready”.

iii) The linear RFQ trap ejection and CPT capture pulses require the linear RFQ trap to have already captured N shots and requires a signal indicating that the data from the previous ion bunch in the CPT has been written to the computer.

These conditions are perhaps better illustrated by the box diagram (figure 3.22) showing the DG11A and Jorway 221 modules and the required conditions.

Some care on the part of the operator is required to ensure that the maximum number of shots are captured in each trap (to prevent decay losses in the traps) while still keeping the total time in the linear RFQ trap slightly less than the time the ions

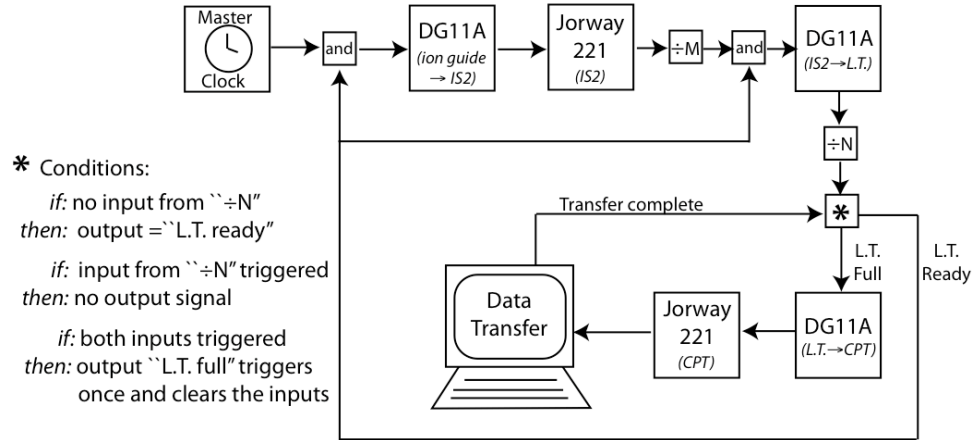


Figure 3.22: This box diagram shows the dependence of each of the timing modules on the capture and ejection conditions of the linear RFQ trap (L.T.) and the CPT. The full timing-circuit diagram is not included here. The box marked with an asterisk is subject to more conditions than the simple “and” gates which are used to provide the conditions for the RFQ ion guide ejection and the IS2 ejection, these conditions are included as part the figure.

spend in the CPT (capturing too many pulses results in the CPT being idle longer than required). The time spent in the IS2 dictates the number of shots which can be captured in the linear trap for a given time spent in the CPT. The time spent applying the RF excitations in the IS2 should be slightly less than the time the ions spend in the ion guide which is set by the master clock.

For all experiments presented here which used the IS2, M was set to 1 and all of the accumulation of ions occurred in the linear RFQ trap.

The frequency and amplitude settings for the RF excitations applied to the CPT had always been set by the online program from values in the loaded parameter file. Modifications to the program within the past year have enabled the IS2 excitation frequencies and amplitudes to also be set via the online program. Prior to these changes the frequencies and amplitudes were set manually by the operator and only the excitation times were controlled by the online program.

3.4.2 Data acquisition system

The data acquisition system is responsible for taking the signal generated when an ion hits the final detector and turning it into a data point containing both the ions TOF information, as well as the applied frequency used for that ion bunch. This is done as follows:

When the ion strikes the MCP or channeltron the signal is amplified, digitized and sent to a multichannel scaler (MCS). Each channel on the MCS is associated with a certain time window, with the first time bin of the MCS being triggered shortly after the ejection pulse from the CPT. The MCS then keeps track of the number of ions which arrive at the final detector during each time channel.

The time allocated to each channel is generated by a 1 MHz clock which is sent through a divide-by- N module. The value chosen for N then becomes the number of 1 MHz pulses (and so the number of μs) per channel. For $A \simeq 90$, N is typically set to 4. As the MCS has 256 channels the total detection time for each ion bunch is typically 1024 μs . The majority of the ions, however, arrive around channels 50-60 (an arrival time of 200-240 μs). This data is transferred to the computer for analysis at the end of each MCS cycle (after each ion bunch).

3.4.3 Data analysis program

The data acquired is stored as 2D array given by the number of ions per MCS channel and the applied frequency. For analysis it is sorted into the following tables, which can be graphed by the online program:

- 1) number of ion *vs.* MCS channel
- 2) TOF_{avg} *vs.* applied frequency
- 3) number of ions *vs.* applied frequency.

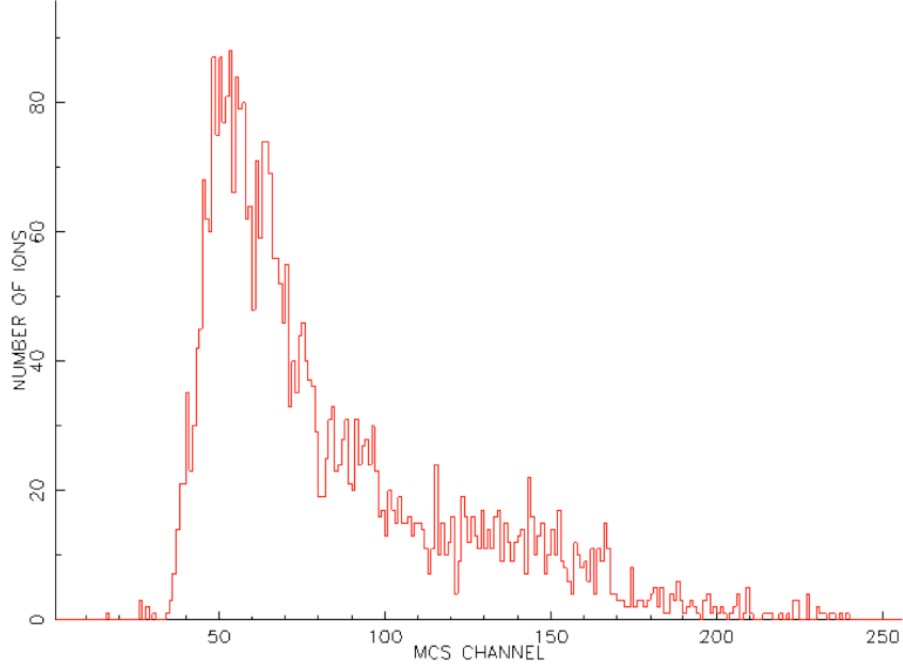


Figure 3.23: Number of ions per MCS channel. The data shown here is for a measurement of ^{87}Mo which used an excitation time of 500 ms.

Fitting function

The data table which is used to determine the ω_c frequency of the ions in the precision Penning trap is the table of the average TOF of the ions *vs.* the applied frequency. An example of the resulting spectrum has already been given in figure 3.18. The line shape of the fitting function which is applied to the TOF spectrum to determine the location of the TOF minimum should be one which best matches the radial energy gain of the ions. This radial energy gain is related to the duration of the RF excitation, T_{conv} , which was originally defined in equation 3.5.

The form of this energy gain for a quadrupole excitation at an applied frequency ω_D is given by [54]:

$$E_{r(\omega_D)} = \frac{q^2 V_{RF}}{2mr_o^4} \frac{\omega_+^2}{(\omega_+ - \omega_-)^2} \frac{\sin^2(\omega_b T_{conv})}{\omega_b^2} \quad (3.6a)$$

$$= \frac{m\pi^2}{8} \omega_+^2 \text{sinc}^2(\omega_b T_{conv}), \quad (3.6b)$$

where

$$\omega_b = \frac{1}{2} \sqrt{(\omega_c - \omega_D)^2 + \left(\frac{\pi}{T_{conv}}\right)^2}. \quad (3.7)$$

The frequency width of the resulting energy-gain spectrum can be determined from equation 3.6. The full width at the half maximum (FWHM or Γ) is the frequency difference between the two applied frequencies for which the following is true:

$$E_{r(\omega_D)} = \frac{E_{r(\omega_c)}}{2}. \quad (3.8)$$

The FWHM is found to be dependent on the excitation time T_{conv} as follows [54]:

$$\text{FWHM} \approx \frac{0.8}{T_{conv}}. \quad (3.9)$$

While this radial energy gain is the basis for the shorter TOF of the excited ions the TOF of the ions also depends on the conversion of this orbital energy to axial energy which occurs in the fringe field of the magnet. This has already been discussed in section 3.3.1; in summary, the axial force on the ions results from the interaction of magnetic moment $\vec{\mu}$ of the ion orbit with the magnetic field gradient in the fringe field of the superconducting solenoid.

The absolute TOF of an ion is then given by:

$$\text{TOF}(\omega_D) = \int_{z_o}^{z_1} \sqrt{\frac{m}{2(E_o - qU_{(z)} - \mu_{(\omega_D)}B_{(z)})}} dz, \quad (3.10)$$

where z_o is the location of the center of the trap, z_1 is the location of the detector, E_o is the total initial energy of the ions, $U_{(z)}$ is the accelerating gradient applied to the TOF drift tube electrodes (shown in figure 3.17) as a function of z , and $B_{(z)}$ is the magnetic field strength as a function of z .

The conversion from orbital energy to linear energy in the fringe field of the magnet modifies the resulting TOF spectra from that given by $E_{r(\omega_D)}$, deepening the

sidebands and broadening the main TOF peak slightly. This results in a function much closer to a sinc function than a sinc^2 function. The sinc fitting function which is used has the form:

$$TOF_{\text{sinc}} = b - a \times \left| \text{sinc}\left([\omega_D - \omega_c]\left[\frac{3.75}{\Gamma}\right]\right) \right| \quad (3.11)$$

where b is the baseline TOF for the unexcited ions, a is the depth of the main TOF dip and Γ is the FWHM. This is the fit which was used when fitting the TOF spectrum “online” (i.e. while taking data).

Data analysis is performed using a program based on the analysis portion of the online program, but which includes a few additional features such as the ability to sort the data based on the number of ions per bunch or select a range of MCS channels. This program is known as the “offline program”. One of the other additional features in this program is the inclusion of another fitting function which is a modified version of the sinc function given in equation 3.11. This modified sinc function includes an extra parameter to account for a potential incomplete conversion or over-conversion of the ions. It is accounted for by representing the time in equations 3.6 and 3.7 as a certain fraction of the conversion time:

$$T_{RF} = \frac{T_{conv}}{c} \quad (3.12)$$

where a full conversion occurs when $c = 1$. The modified-sinc fitting function then has the form:

$$TOF_{\text{mod sinc}} = b - a \times \left| \frac{\sin\left(\left(\frac{0.89}{2\Gamma}\right)\sqrt{4\pi^2(\omega_D - \omega_c)^2 + \left(\frac{c\pi\Gamma}{0.89}\right)^2}\right)}{\left(\frac{0.89}{\pi\Gamma}\right)\sqrt{4\pi^2(\omega_D - \omega_c)^2 + \left(\frac{c\pi\Gamma}{0.89}\right)^2}} \right| \quad (3.13)$$

The variable parameters in this modified-sinc fitting function are the TOF baseline (b), the maximum TOF depth (a), the FWHM (Γ) and the conversion factor (c).

Though the baseline and the TOF depth are only weakly mass dependent over the range of masses measured during a typical experiment, they are, however, sensitive

to systematic effects. For example, the composition of the ion bunch (the ion purity) can have a significant effect on the TOF depth as this value is an average of the TOF of all the arriving ions. If contaminant ions are present the maximum TOF is an average of both excited and non-excited ions and this results in a smaller TOF depth. As these parameters can change from measurement to measurement b and a are left as free parameters in the fit.

The FWHM and the conversion factor, however, depend only on the applied excitation and so should be the same for all measurements which used the same RF excitation time and amplitude. These two parameters are initially fit as free parameters for measurements of pure ion samples (i.e. with large TOF depths) with high statistics. These measurements were typically our calibration measurements. The resulting values for Γ and c are then fixed for all fits of TOF spectra generated using the same excitation time and amplitude.

Chapter 4

Data, analysis and results

Having produced the ions of interest, transported them through the CPT system, cleaned out contaminant ions, positioned them in the trap, applied a quadrupole RF excitation around that of the expected ω_c frequency, and determined at which applied frequency energy has been added to the ions through the use of a TOF technique, it is only at this point that the “interesting” physics, that which gives some insight into the nature of the Universe, begins. For our data to be able to say something meaningful we need to have chosen nuclides which address some particular outstanding questions, but just as importantly we need to have acquired “good” data.

The basic parameters for quantifying what we mean by “good” data is fairly straightforward. First of all, we want to be sure that we have taken enough data to have a statistically significant result, which generally involves having a good signal-to-noise ratio. In our case the TOF depth of the peak should be significantly greater than the uncertainty in the average TOF at any one applied frequency. A poor signal-to-noise ratio can be a result of poor statistics (i.e. not enough ions measured) and/or large systematic uncertainties (see section 4.2). The signal-to-noise ratio is also negatively affected by the presence of contaminant ions (which reduce the average TOF) or poor CPT capture timing settings (which add energy to the trapped ions lowering the baseline as discussed in section 3.3.1).

Two other important factors are the resolving power of the spectrometer, which is

a measure of the ability of the spectrometer to distinguish between two nearby TOF peaks, and the precision of the measurement, which is how well we can determine the centroid of the TOF peak. Both the resolving power (R) and the precision (P) depend on the FWHM of the fit to the TOF spectrum 3.18, which was shown to depend on the RF excitation time used (equation 3.9).

Resolving power

The resolving power ($m/\Delta m$) is a measure of the ability of the spectrometer to distinguish between two nearby mass peaks, such as the peak related to the ground state of an isotope and the peak associated with its isomer, if one exists. As many of the nuclides presented here have known isomers, the resolving power that was used determined whether or not we could distinguish each state independently.

The resolving power is given by:

$$R = \frac{m}{\Delta m} = \frac{\omega_c}{\Delta\omega_c} \approx \omega_c T_{RF}, \quad (4.1)$$

where $\Delta\omega_c$ is the FWHM of the TOF dip in the TOF *vs.* applied frequency plot which was shown in figure 3.18. It can be seen that longer RF excitation times lead to higher resolving powers and thus better resolutions.

Precision

While the precision of a measurement is related to its resolving power, the precision is dependent on more factors and is essentially a measure of how well we can reduce the uncertainty in our determination of the centroid of the TOF peak. The precision P in our mass determination is directly related to the precision in the ω_c determination:

$$P = \frac{\delta m}{m} = \frac{\delta\omega_c}{\omega_c}, \quad (4.2)$$

where $\delta\omega_c$ is the uncertainty in the parameter ω_c and comes from the least-squares fit of the fitting function to the data. The ω_c uncertainty is a function of both the

number of ions detected (which determines in part the uncertainty in the average TOF of each point in the spectrum) as well as the line width (the FWHM). An empirical relationship for this dependence on the resolving power (equation 4.1) and the number of ions has been determined to be [55]:

$$\frac{\delta m}{m} \approx \frac{1}{R\sqrt{N}} \quad (4.3)$$

where N is the number of ions. Then, from equation 4.1 and the cyclotron frequency (equation 2.1) we find:

$$\frac{\delta m}{m} = \frac{m C}{q B T_{RF} \sqrt{N}}, \quad (4.4)$$

where C is a constant included to take into account the fitness of the fitting function and factors such as the purity of the ion bunch.

It might seem, given the dependence of resolving power and precision on the applied excitation time, that arbitrarily small precisions and resolutions could be achieved if we were to apply the excitation for long periods of time. There are limits to this in practice, however. The maximum excitation time which has proven to be experimentally feasible in the CPT is a 3 s excitation time. This is thought to be set in part by effects due to the residual vacuum pressure, even with pressures of only $\sim 4.5 \times 10^{-10}$ torr in the trap. Unstable nuclides created “online” have additional restrictions. The limited beam-time available means that a balance needs to be struck between the precision gained by increased excitation times (T_{RF}) and the resulting length of time required to acquire an adequate number of statistics (\sqrt{N}). For measurements with desired precisions in the range of 10^{-7} to 10^{-8} excitation times of 0.5 s are generally adequate.

Among the nuclides presented in this thesis, the shortest half-life is 4.66 s and we were limited only by the above considerations. For shorter-lived nuclides, however, the half-lives can also limit the precision as long excitation times can potentially result in significant decay losses. The only factors in the equation for precision (equation 4.4) which are limited by the half-life of the ions are the number of ions, N , and the

excitation time which can be applied, T_{RF} .

The number of ions detected for a given rate of production (λ_R) (and with a β -decay rate of λ_β) is the number of the ions which are accumulated in the linear RFQ trap in time t :

$$N_{L.T.} = \frac{\lambda_R}{\lambda_\beta} (1 - \exp^{-\lambda_\beta t}), \quad (4.5)$$

which remain after the same time t in the Penning trap, as the total accumulation time in the linear trap is equal to the time the ions spend in the CPT. We find than that

$$N = N_{L.T.} (\exp^{-\lambda_\beta t}). \quad (4.6)$$

If the total time that the ions were in the Penning trap was spent applying the quadrupole RF excitation ($t = T_{RF}$) then the maximum possible precision would occur for an excitation time $T_{RF} \approx 2t_{\frac{1}{2}}$ (where $t_{\frac{1}{2}}$ is the half-life of the ions). As there is a certain amount of time required to prepare the ions in the trap prior to the measurement (to clean contaminants via ω_+ excitations and position the ions via ω_- excitations) t is, however, not equal to T_{RF} . Instead $t = T_{\text{prep}} + T_{RF}$. As this preparation time increases, the maximum possible precision which can be obtained decreases. The excitation time which gives the maximum possible precision is found to change as well and, for large cleaning times, becomes $T_{RF} \approx 2.6t_{\frac{1}{2}}$. The additions to the CPT system such as the isobar separators and the Tabor arbitrary waveform generator, which reduce the required preparation time in the trap, become increasingly important when measuring short-lived ions.

4.1 Data and Analysis

4.1.1 Summary of experiments

Mass measurements of 18 proton-rich nuclides of elements niobium, molybdenum, technetium, ruthenium and rhodium are presented in this thesis. As was discussed in Ch. 3, these proton-rich nuclides were produced in fusion-evaporation reactions

Table 4.1: A summary of beams, beam energies and targets for all 8 experiments are listed along with the nuclides measured in each experiment.

Expt.	Beam	Energy (MeV)	Target	Nuclides Measured
1	^{40}Ca	170	$^{\text{Nat}}\text{Ni}$	^{93}Tc , $^{93,94}\text{Ru}$, $^{94,95}\text{Rh}$
2	^{36}Ar	150	$^{\text{Nat}}\text{Ni}$	$^{90,91}\text{Mo}$, $^{90,91,92}\text{Tc}$
3	^{36}Ar	130	$^{\text{Nat}}\text{Ni}$	$^{91,92}\text{Ru}$
4	^{36}Ar	125	$^{58}\text{Ni}^*$	^{91}Tc , ^{91}Ru
5	^{40}Ca	185	$^{58}\text{Ni}^*$	^{90}Mo , $^{90,93}\text{Tc}$, $^{91,93}\text{Ru}$, ^{93}Rh
6	^{40}Ca	185	$^{58}\text{Ni}^*$	$^{92,93}\text{Tc}$, ^{92}Ru
7	^{40}Ca	190	$^{58}\text{Ni}^*$	^{92}Mo , $^{90,92,93}\text{Tc}$, $^{90,92,93}\text{Ru}$, $^{92,93,94}\text{Rh}$
8	^{40}Ca	190	$^{58}\text{Ni}^*$	^{93}Ru , $^{92,93}\text{Rh}$
		200	$^{58}\text{Ni}^*$	^{87}Nb , ^{87}Mo , ^{93}Ru , ^{93}Rh

*99.6% enriched

using beams from the ATLAS accelerator at Argonne National Laboratory. The data were acquired over the course of 8 experiments spread out over a 4-year time period. A summary of accelerator beams, their energies, the target materials used and the nuclides measured in each experiment are presented in table 4.1.

Representative TOF spectra for 4 of these nuclides are shown in figure 4.1. These nuclides were the least stable and also the least abundantly produced isotopes of the elements Mo, Tc, Ru, and Rh and were consequently the most difficult of the nuclides to measure. Excitation times of 500 ms were used to acquire these resonances in all cases except that of ^{92}Rh which used a 300 ms excitation time. The low production of ^{92}Rh of only 0.3 ions per bunch on average, and the fact that the TOF depth indicates the presence of potential contaminant ions, meant that additional scans (a total of 967 in the case of the spectra shown in figure 4.1) were needed to get an

adequate signal-to-noise ratio (no additional correction for the contaminant ion is deemed necessary because, at 0.3 ions loaded into the trap per bunch it is unlikely that both species were ever in the trap at the same time). For comparison, the example spectra shown for ^{87}Mo had even fewer ions per bunch (0.23) than the ^{92}Rh case but, as no contaminant ions were present, only 408 scans were needed to acquire the resulting TOF spectrum. The depth of the TOF peak of ^{87}Mo as compared to the error bars on the data points, indicate that the resulting signal-to-noise is still much better than in the case of ^{92}Rh even with half as many scans. The spectra shown for ^{90}Tc is an example of a best-case scenario as it was a high purity ion sample which was well produced in the fusion-evaporation reaction used. Consequently, with 7.25 ions per bunch, only 80 scans were required to get the TOF spectrum provided. The TOF spectrum of ^{90}Ru shows a case where, while there was a reasonable number of ions per bunch (3.25), we were running short on available beam-time and so only 116 scans of this ion were acquired. This provided an adequate signal-to-noise ratio to be a statistically significant measurement, but the resulting effect of the low signal-to-noise on the precision to which we can fit the data is seen as compared to cases like ^{90}Tc and ^{87}Mo . All the spectra shown are from experiments 7 or 8 as, in cases where there have been more than one measurement, these runs resulted in the highest precision measurements of these nuclides.

One might notice from table 4.1 that many nuclides have been measured in more than one experiment. There are a several reasons for this, all primarily related to the production efficiencies of these nuclides in the fusion-evaporation reactions. Nuclides closer to stability tend to be easier to produce and so have been measured in multiple experiments as a means of checking our system and checking the production rates of the fusion-evaporation reactions used. Also, their higher production meant that it took less time to acquire statistically significant data; a single measurement or two to verify the transmission of the system was enough to contribute to our measured value. Nuclides further from stability were usually revisited to add to the statistics —

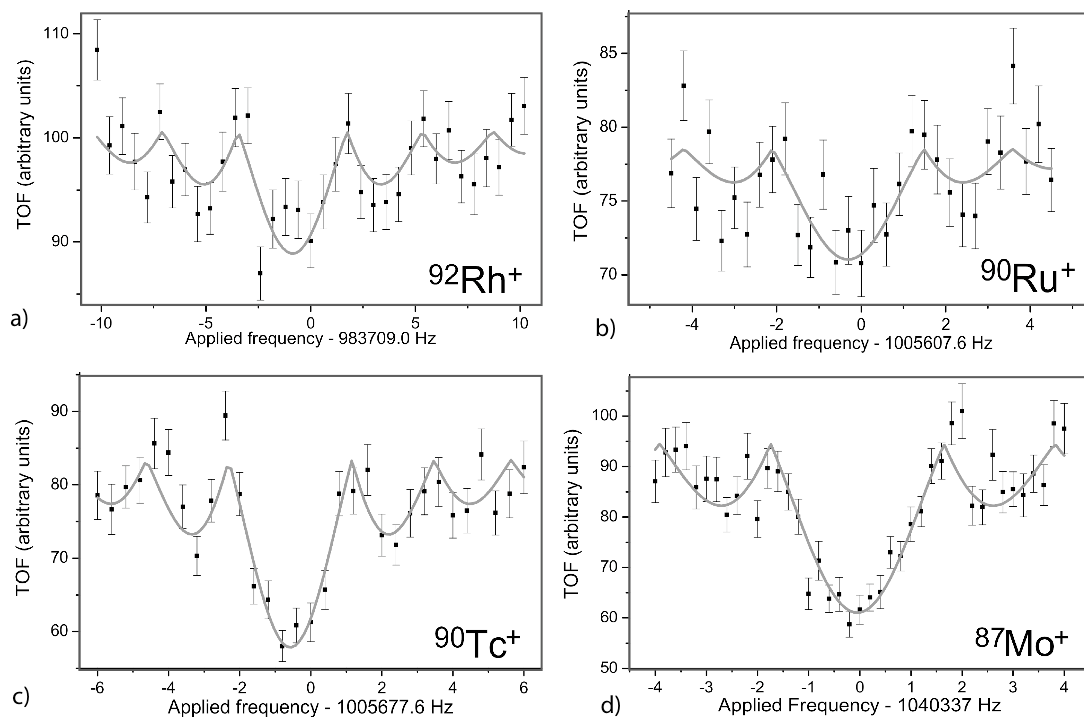


Figure 4.1: Representative time-of-flight spectra for ions of the lightest isotope measured for 4 of the 5 chemical elements measured. Quadrupole RF excitations of 500 ms were used for these spectra except in the case of ^{92}Rh where an excitation time of 300 ms was used. The curves shown represent the theoretical line shapes expected.

increasing \sqrt{N} and reducing the uncertainty in the average TOF per point. In some cases these nuclides were revisited to improve the precision by using longer excitation times than had been used in previous experiment(s).

4.1.2 Data Analysis

As more than one measurement is taken over the course of an experiment, and as the same nuclide is often measured in several different experiments, a method of combining this data to ensure the correct weighting and propagation of errors¹ becomes necessary. A short summary is provided here with a more detailed discussion presented in Appendix B.

The reduced chi square, χ_r^2 , which is a measure of the “goodness-of-fit” of the fitting function to the data, was typically ~ 1 , but when it was larger we followed the standard error analysis procedure and inflated the uncertainty determined from the fit by multiplying it by $\sqrt{\chi_r^2}$. Multiple measurements taken over a single experiment were combined by taking a weighted average of the ω_c frequencies of each ion determined in separate measurements. Both the internal error (based on the measured uncertainties only) and external error (based on the weighted difference of the measured value from the resulting average) were calculated. The largest of these two uncertainties is the one which was taken to be the uncertainty in the weighted average. The values of the weighted averages were compared to fits of TOF spectra which included all of the data points from all measurements of a given nuclide taken during a single experiment which used the same RF excitation parameters (measurements with different scan widths, frequency step sizes, and central frequencies generally cannot be combined). The ω_c values determined from these two methods agreed within the uncertainty as would be expected.

To determine the mass of a nuclide from its average ω_c frequency, precise knowl-

¹note that the terms “error” and “uncertainty” are often used interchangeably. As these values are not in fact errors the term “uncertainty” is preferred. Some of the terminology such as “propagation of errors” and “error bars” however is standard and will be used.

edge of the magnetic field of the Penning trap is required. Instead of determining B explicitly, the cyclotron frequency of an ion with a precisely known mass is measured and the frequency ratio between the ω_c values of the unknown and calibrant ions (\mathcal{R}) is used. Hydrocarbons present in the system were chosen as calibrants due to their precisely known masses. The cyclotron frequency ratios for each nuclide and calibrant pair from each experiment are given in table 4.2.

To determine the mass of the nuclide of interest, m_n , from the frequency ratio the following relationship is used:

$$m_n = \mathcal{R}(m_c - m_e) + m_e, \quad (4.7)$$

where m_e is the mass of the electron and m_c is the mass of the chosen calibrant (these values are given in table 4.3). The mass of the electron is included to account for the fact that we have measured the ω_c frequency of an ion, but wish to determine the mass of the neutral atom. The charge state of the ion must therefore be taken into account. All the ions measured in these experiments were singly charged, however, if either the ion of interest or the calibrant were doubly charged (or more), the mass of the appropriate number of electrons would have to be included.

Often, it is more useful to have the atomic mass expressed in terms of its mass excess, which is the difference between the atomic mass and the sum of all its constituent masses. The mass excess of a nuclide with mass m_n is:

$$\text{Mass Excess} = (m_n - A) * \mathcal{C} \quad (4.8)$$

where A is the mass number of the nuclide and \mathcal{C} is the conversion constant from u to keV given in table 4.3. The uncertainty in the mass excess is simply the uncertainty in the mass multiplied by the u to keV conversion constant. These mass excesses provide a measure of the binding energy of the nucleus and make the calculation of proton and neutron separation energies very straightforward.

Table 4.2: Cyclotron frequency ratio between the ion of interest and calibrant ion with only statistical uncertainty shown.

Measured Ion	Calibrant	Ratio (\mathcal{R})	Expt. #
$^{87}\text{Nb}^+$	$^{12}\text{C}_7^1\text{H}_9^+$	0.93392330(30)	8
$^{87}\text{Mo}^+$	$^{12}\text{C}_7^1\text{H}_9^+$	0.934004087(41)	8
$^{90}\text{Mo}^+$	$^{12}\text{C}_7^1\text{H}_6^+$	0.998522774(46)	2
	$^{12}\text{C}_7^1\text{H}_9^+$	0.96608486(24)	5
$^{90}\text{Tc}^+$	$^{12}\text{C}_7^1\text{H}_6^+$	0.998635367(70)	2
	$^{12}\text{C}_7^1\text{H}_9^+$	0.96619389(23)	5
	$^{12}\text{C}_7^1\text{H}_9^+$	0.966193694(84)	7
$^{90}\text{Ru}^+$	$^{12}\text{C}_7^1\text{H}_9^+$	0.96626101(11)	7
$^{91}\text{Mo}^+$	$^{12}\text{C}_7^1\text{H}_7^+$	0.998429163(87)	2
$^{91}\text{Tc}^+$	$^{12}\text{C}_7^1\text{H}_7^+$	0.998502641(700)	2
	$^{12}\text{C}_7^1\text{H}_7^+$	0.998502501(44)	4
^{91}Ru	$^{12}\text{C}_7^1\text{H}_8^+$	0.9876613(66)	3
	$^{12}\text{C}_7^1\text{H}_7^+$	0.998593853(35)	4
	$^{12}\text{C}_7^1\text{H}_9^+$	0.97696731(24)	5
$^{92}\text{Mo}^+$	$^{12}\text{C}_7^1\text{H}_9^+$	0.987497392(70)	7
$^{92}\text{Tc}^+$	$^{12}\text{C}_7^1\text{H}_7^+$	1.00945040(11)	2
	$^{12}\text{C}_7^1\text{H}_8^+$	0.99839969(14)	6
	$^{12}\text{C}_7^1\text{H}_9^+$	0.987588298(60)	7
$^{92}\text{Ru}^+$	$^{12}\text{C}_7^1\text{H}_8^+$	0.99845374(19)	3
	$^{12}\text{C}_7^1\text{H}_8^+$	0.99845346(11)	6
	$^{12}\text{C}_7^1\text{H}_9^+$	0.987641576(53)	7
$^{92}\text{Rh}^+$	$^{12}\text{C}_7^1\text{H}_9^+$	0.98777176(24)	7
	$^{12}\text{C}_7^1\text{H}_9^+$	0.98777183(18)	8
$^{93}\text{Tc}^+$	$^{12}\text{C}_7^1\text{H}_9^+$	0.998278826(79)	1
	$^{12}\text{C}_7^1\text{H}_9^+$	0.99827903(24)	5
	$^{12}\text{C}_7^1\text{H}_8^+$	1.0092084(21)	6
	$^{12}\text{C}_7^1\text{H}_9^+$	0.998278827(88)	7
$^{93}\text{Ru}^+$	$^{12}\text{C}_7^1\text{H}_9^+$	0.998352655(64)	1
	$^{12}\text{C}_7^1\text{H}_9^+$	0.99835277(25)	5
	$^{12}\text{C}_7^1\text{H}_9^+$	0.998352593(46)	7
	$^{12}\text{C}_7^1\text{H}_9^+$	0.998352615(28)	8
$^{93}\text{Rh}^+$	$^{12}\text{C}_7^1\text{H}_9^+$	0.99844756(28)	5
	$^{12}\text{C}_7^1\text{H}_9^+$	0.998447106(50)	7
	$^{12}\text{C}_7^1\text{H}_9^+$	0.998447265(33)	8
$^{94}\text{Ru}^+$	$^{12}\text{C}_7^1\text{H}_{10}^+$	0.998225805(48)	1
$^{94}\text{Rh}^+$	$^{12}\text{C}_7^1\text{H}_{10}^+$	0.998336267(58)	1
	$^{12}\text{C}_7^1\text{H}_9^+$	1.00914695(32)	7
$^{95}\text{Rh}^+$	$^{12}\text{C}_7^1\text{H}_{10}^+$	1.00890391(11)	1

Species	Mass (u*)	Mass Excess (keV)
e	$5.485799110(12) \times 10^{-4}$	
p	1.00727646676(10)	7288.97050(11)
n	1.00866491574(56)	8071.31710(53)
C ₇ H ₆	90.04695019242(60)	
C ₇ H ₇	91.05477522449(70)	
C ₇ H ₈	92.06260025656(80)	
C ₇ H ₉	93.07042528863(90)	
C ₇ H ₁₀	94.0782503207(10)	

* 1 u = 931494.009 keV

Table 4.3: Table of auxiliary data. All values included here have been acquired or derived from [20, 21]. Note that the masses given for the hydrocarbons do not include the enthalpy of formation and the electron binding energies as they are negligible compared to the uncertainties of the measured frequencies used in the calculations. The masses of the proton (m_p) and neutron (m_n) are not used in our mass determinations but will be used in calculations of separation energies in chapter 5.

As not all the settings of the CPT system were the same from experiment to experiment, and considering that the magnetic field generated by the superconducting magnet is expected to decay slightly over time (< 2.5 ppb/day, see section 4.3), we do not expect the measured ω_c frequency for a given ion to be the same from experiment to experiment. As these shifts affect all cyclotron frequencies the same way the frequency ratios will be still be consistent. As different calibrant ions were occasionally used in different experiments, we determined the mass of the measured nuclide for each experiment and then took the weighted average of these masses across all experiments to arrive at our final value. The uncertainty in the weighted average of the mass was again taken to be the larger of the internal and external errors. The value determined for the potential systematic error (see section 4.2) was added in quadrature to the statistical uncertainty of the mass determination from each experiment before this last weighted average was taken.

4.2 Systematic effects

As with any experimental measurement, there are many potential sources of systematic effects in these Penning trap mass measurements. While many of these effects can be dramatically reduced or even nearly eliminated through care taken in the design and construction the trap, or by taking frequency ratios of ions with nearly equal masses when determining the measured mass, it is important to have a clear understanding of what these effects are and how they can arise. The systematic effects tend to fall into 4 categories: electric field imperfections, magnetic field imperfections, misalignments and ion-ion effects.

4.2.1 Electric field imperfections

Any deviations of the electric field in the trap from the ideal electric field (equation 2.2) can result in systematic shifts in the measured ω_c . The dependence of this potential ω_c frequency shift on trap parameters is given as [54]:

$$\Delta\omega^{elec} = \Omega_c^{elec} \left[\frac{3C_4}{2d^2}(\rho_-^2 + \rho_+^2) + \frac{15C_6}{4d^4}(\rho_z^2(\rho_-^2 - \rho_+^2) - (\rho_-^4 + \rho_+^4)) \right] \quad (4.9)$$

with

$$\Omega_c^{elec} = \frac{\omega_-}{1 - \omega_-/\omega_+} \approx \omega_- \approx \frac{U_o}{2d^2B}, \quad (4.10)$$

and where U_o is the trapping potential, d is a geometric factor (discussed in section 2.1.1), ρ is the orbital radius or amplitude of the ω_+ , ω_- or ω_z motions and C_4 and C_6 are, respectively, the octupole and dodecapole components of the electric field.

To minimize this potential systematic effect an effort has been made to reduce the octupole and dodecapole components of the field as much as possible. This has been done through the precision machining of the electrodes, the symmetrical design, and through the inclusion of the correction electrodes. This was also the primary reason for the gold plating of the electrodes to reduce possible surface charge effects. The

effort spent ensuring that the ions were captured in such a way that they had the lowest possible energies in the trap also helped reduce these systematic effects, as this reduced the orbital radii (ρ) of the ion motions. The magnetic field strength B , trap geometry d and trapping potential U_o all have other criteria which tend to determine their chosen values, but their potential contribution to this systematic effect should also be kept in mind.

As $\Delta\omega_c^{elec}$ is essentially mass independent, the fractional error $\Delta\omega_c^{elec}/\omega_c$ is not a constant across all masses. If the fractional error were constant then, when we took the ratio of two measured ω_c values as we do to determine the measured mass, this systematic effect would cancel out. Instead we find that the size of this systematic effect depends on the mass difference between the ion and the calibrant ion as:

$$\frac{\Delta m^{elec}}{m} = \frac{\Delta\omega_c^{elec}(m - m_{cal.})}{\omega_c m}. \quad (4.11)$$

Therefore choosing calibrant ions with a similar mass to the nuclide of interest is another way to minimize the systematic effects arising from imperfections in the electric field.

4.2.2 Magnetic field imperfections

Any deviations of the magnetic field from an ideal field, in other words any field inhomogeneities, can also give rise to systematic effects. The strength of this systematic effect depends on the strength of any hexapole component of the field (β_2) and on the area of the magnetic field which is sampled by the ion. Again we find that limiting the energy of the ions in the trap, thus limiting the radii of their motions and the amplitude of the ω_z oscillation, is the primary method of reducing this potential systematic effect. The form of this dependence is [54]

$$\Delta\omega_c^{mag} \approx \beta_2 \omega_c (\rho_z^2 - \rho_-^2). \quad (4.12)$$

As $\Delta\omega_c^{mag}$, unlike $\Delta\omega_c^{elec}$, does depend on ω_c this effect cancels out when we take the frequency ratio. This is only true, however, when the radii of the ion motions

are the same, which is why care is taken to capture each ion bunch the same way (to keep ρ_z constant), and one of the reasons why we apply an ω_- excitation (as it ensures similar ω_- orbits for all ions). Also, using a magnetic field with a small β_2 component helps ensure that any resulting effect from potential deviations of these radii remain small.

Another systematic effect due to the magnetic field does not come from any variations in the field in space, but rather variations in the field over time. Though superconducting magnets have relatively stable fields, the measured ω_c value depends directly on the magnetic field strength so to achieve measurements to precisions of 10^{-8} or better it is best if the magnetic field is stable to at least that level over the duration of the experiment. The magnetic field drift can be accounted for by monitoring the measured ω_c values for any systematic changes over time. In cases where high precision is desired it is best to interleave measurements of the calibrant and the ion of interest and only take frequency ratios of the measurements closest in time. We are fortunate as the magnet used for the precision Penning trap is very stable and no shifts are generally seen over the course of a week-long experiment within our experimental precision. As a result we have only been able place an upper limit on this effect (this is discussed further in section [4.2.5](#)).

4.2.3 Misalignments

Another important consideration is the relative alignment of the electric and magnetic fields of the trap as all of the ion motions discussed in chapter [3](#) are based on the assumption that the symmetry axis of the electric field is parallel to the magnetic field. Any misalignment then changes the equations of ion motion from the form in which they have been presented. Keeping the x, y and z directions defined by the trap electrodes we find that with any misalignment, the magnetic field which was

$$B_z = B, \quad B_x = B_y = 0 \quad (4.13)$$

then becomes

$$B_z = B \cos \theta, \quad B_x = B \sin \theta \cos \phi, \quad B_y = B \sin \theta \sin \phi, \quad (4.14)$$

where θ is the angle between the z axis and the magnetic field and ϕ is the angle between the x axis and the plane containing both the z axis and the magnetic field vector [56]. If this is the case then the two eigenmotions in the x, y plane no longer sum to ω_c . The resulting shift $\Delta\omega_c^{align}$ is found to be mass independent and, for small angles θ , given by [54]

$$\Delta\omega_c^{align} = \frac{9}{4}\omega_- \sin^2 \theta. \quad (4.15)$$

The resulting Δm^{align} then depends on the difference in masses between the ion of interest and the calibrant ion in the same way as Δm^{elec} (see equation 4.11). The precision machining of the CPT drift tube discussed in 3.3.1 was undertaken in an effort to minimize this effect. The angle of misalignment between the fields in the CPT is estimated to be < 0.2 milliradians [49].

4.2.4 Ion-ion effects

As the applied quadrupole RF excitation acts on the center of mass motion of the ion cloud, no shift in ω_c is expected theoretically when there are multiple ions of the same species in the trap. While the ion motion as a whole is not affected, it has been shown that if enough of these ions are pushed outwards by the resulting space-charge, thus covering a larger area within the trap, they are more likely to sample areas where trap imperfections are more pronounced. This can result in an uncategorized shift in the ω_c frequency [56]. The best way to minimize this effect is to limit the number of ions present in the trap during measurements.

When more than one species of ion are present in the trap there are other effects in addition to the case just discussed for pure ion samples. When the two ion species cannot be resolved only one resonance appears in the TOF spectrum and it has a frequency corresponding to the ω_c frequency of the average mass of the ions in the

trap. When two ion species present in the trap are resolvable the resonances for both species are shifted to frequencies which are lower than the ω_c frequency of each mass. The amount each resonance shifts by is proportional to the relative number of ions of the other species in the trap [57]. These effects can only be reduced through efficient cleaning of contaminant ions prior to measurement.

4.2.5 The resulting systematic uncertainty

To determine the potential systematic uncertainties quantitatively, various studies of the ion behavior in the trap have been performed:

Past tests of the trap, done in similar conditions to these measurements, have indicated that the systematic effects arising from mass differences between the ion of interest and the calibrant ion are less than 1 ppb/u [58]. In this experiment the largest mass difference between an ion of unknown mass and a calibrant was 6.15 u (^{87}Nb and C_7H_9) so in most cases this effect is negligible.

To look for possible changes in the magnetic field over the course of an experiment, the measured ω_c of each ion is monitored for changes over time. No shifts in ω_c were seen within the precision of our measurements. As a slow decay of the magnetic field is expected we apply a systematic uncertainty based on the upper limit that has been measured for this decay. The most precise determination to date comes from measurements of stable and very long-lived ions and is found to be < 2.5 ppb/day [13].

The resulting systematic effect due to the presence of multiple identical ions in the trap has also been studied and was found to be < 2 ppb per detected ion [11, 14]. In a recent experiment where the trap was subject to a small amount of surface charge (from an electrical discharge near the trap) this ion-ion effect was found to be ~ 13 ppb per detected ion [13]. As no evidence of a surface charge was seen (determined by measuring ω_- and ω_+) in any of the 8 experiments presented here this is presented only as an indication of the magnitude of this effect in a worst-case scenario. Ion-ion effects which involve contaminant ions present in the trap have an upper limit

estimated at ~ 10 ppb [17]. This value was determined in a past experiment from mass discrepancies which remained between the mass determinations of very precisely known nuclides and their AME03 values [21] after all other known systematic effects had been accounted for [17, 11]. To ensure that both of these ion-ion effects remained small, cuts were applied to the data to exclude any data point which included ≥ 10 detected ions.

The resulting total systematic uncertainty of $\Delta m/m = 25$ ppb is combined with the statistical uncertainties listed in table 4.2 to give the mass uncertainties quoted in table 4.4.

4.3 Final Numerical Results

The resulting mass values which are calculated from the frequency ratios presented in table 4.2 are reported in table 4.4. Also presented for comparison sake are the mass excess values presented in the 2003 Atomic Mass Evaluation (AME03) [21] and any other Penning trap measurements which exist for these nuclides. The differences between these values and ours are also given. Negative differences indicate that our measured mass is lighter and more bound whereas positive differences indicate that our measured mass is heavier and less bound. A graphical comparison of our measurements to the AME03 values and those measured with other Penning traps can be seen in figure 4.2. To show more clearly the agreement among the Penning trap measurements a comparison of just these mass excesses is given in figure 4.3.

As the AME03 mass excesses included in the table are all ground state mass excesses it should be noted that there are two cases, ^{90}Tc (discussed in section 5.2.3) and ^{94}Rh (discussed in section 5.2.5), where the assignment of the two existing long-lived states to the ground or isomeric states are still uncertain. Our mass measurements are of the same nuclear state as was measured by other Penning traps, but may or may not correspond to the ground state of the nuclide presented in the AME03. This will be discussed in much greater detail in chapter 5.

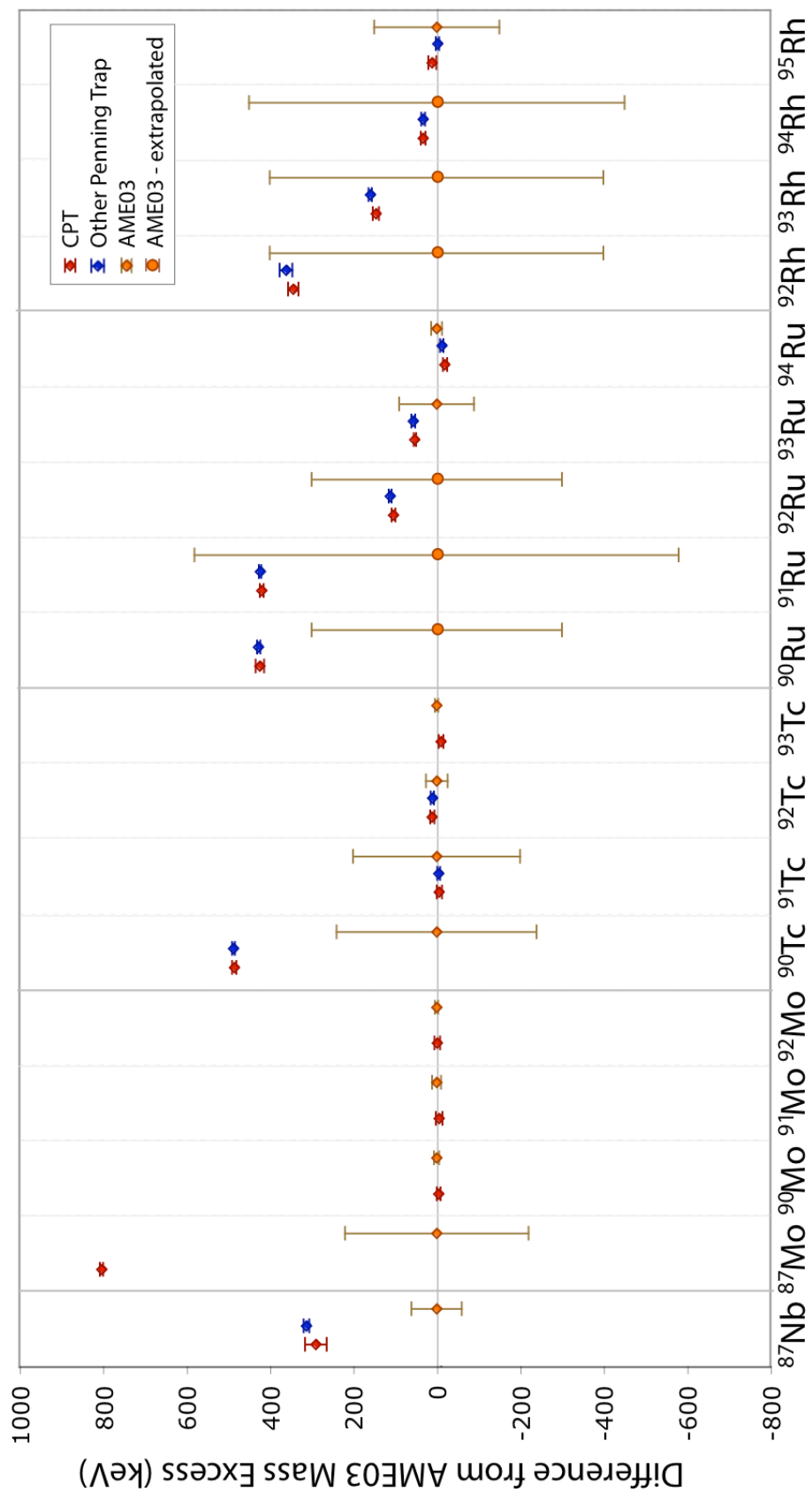


Figure 4.2: Comparison of mass excesses. Plotted are the differences between the mass excesses from Penning trap measurements and those presented in the AME03. CPT mass measurements are shown in red and other Penning trap measurements are shown in blue. The AME03 values are also shown (orange) along with their uncertainties.

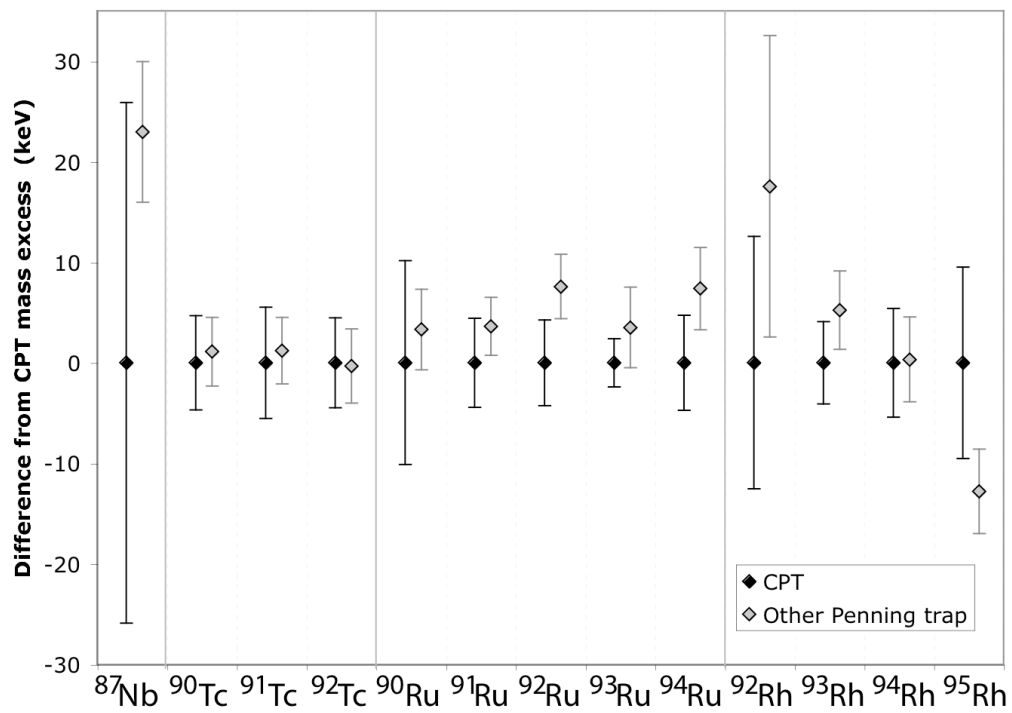


Figure 4.3: Comparison of the CPT mass measurements with those performed using other Penning traps.

Table 4.4: Atomic masses with combined statistical and systematic uncertainties, and the resulting mass excesses. Included in the table are the AME03 mass excess values [21] as well as other Penning trap (PT) measurements where they exist [42, 59]. The rightmost column includes the resulting weighted averages of the existing Penning trap measurements (PT_{w.a.}).

Nuclide	Mass (u)					Mass excess (keV)				
	CPT	CPT	CPT	AME03	AME03	AME03	Other PT	Other PT	Δ _{OtherPT}	PT _{w.a.}
⁸⁷ Nb	86.920675(28)		-73891(26)	-74180(60)	289(65)	-73868(7) [‡]		-23(27)		-73869.6(6.8)
⁸⁷ Mo	86.9281938(38)		-66887.1(4.1)	-67690(220)	803(220)					
⁹⁰ Mo	89.9139319(46)		-80171.9(4.3)	-80167(6)	-4.9(7.4)					
⁹¹ Mo	90.9117439(83)		-82210.0(7.7)	-82204(11)	-6(13)					
⁹² Mo	91.9068091(70)		-86806.8(6.4)	-86805(4)	-1.8(7.6)					
⁹⁰ Tc*	89.9240738(50)		-70724.8(4.7)	-71210(240)	485(240)	-70723.7(3.4)*		-1.1(5.8)		-70724.1(2.8)
⁹¹ Tc	90.9184257(60)		-75986.0(5.5)	-75980(200)	-6(200)	-75984.8(3.3)*		-1.2(6.5)		-75985.1(2.8)
⁹² Tc	91.9152712(48)		-78924.4(4.5)	-78935(26)	11(26)	-78924.7(3.7)*		0.3(5.8)		-78924.6(2.9)
⁹³ Tc	92.9102371(55)		-83613.6(5.1)	-83603(4)	-10.76(6.5)					
⁹⁰ Ru	89.930341(11)		-64887(10)	-65310(300)#	423(300)#	-64883.3(4.0)*		-3(11)		-64883.7(3.7)
⁹¹ Ru	90.9267406(48)		-68240.7(4.4)	-68660(580)#	419(580)#	-68237.1(2.9)*		-3.6(5.3)		-68238.2(2.4)
⁹² Ru	91.9202286(46) [†]		-74306.6(4.3) [†]	-74410(300)#	103(300)#	-74299.0(3.2)*		-7.6(5.3)		-74301.7(3.6)
⁹³ Ru	92.9171036(26)		-77217.5(2.4)	-77270(90)	53(90)	-77214.0(4.0)*		-3.5(4.7)		-77216.6(2.0)
⁹⁴ Ru	93.9113382(51)		-82588.0(4.7)	-82568(13)	-20(14)	-82580.6(4.1)*		-7.4(6.3)		-82583.8(3.7)
⁹² Rh	91.932349(13)		-63017(13)	-63360(400)#	343(400)#	-62999(15) ^{*§}		-18(20)		-63009.3(9.6)
⁹³ Rh	92.9259077(44)		-69016.5(4.1)	-69170(400)#	153(400)#	-69011.3(3.9)*		-5.2(5.7)		-69013.8(2.8)
⁹⁴ Rh*	93.9217302(58)		-72907.8(5.4)	-72940(450)#	32(450)#	-72907.5(4.2)*		-0.3(6.8)		-72907.6(3.3)
⁹⁵ Rh	94.915910(10)		-78329.5(9.5)	-78340(150)	10(150)	-78342.3(4.2)*		13(10)		-78340.2(4.7)

Indicates an extrapolated mass value

† A. Kankainen *et al.*, JYFLTRAP [59]

‡ This measurement is also reported in A. Kankainen *et al.* [60] but without the correction to the uncertainty which is discussed in [42].

* Note that while the measured state is clear, the ordering of the long-lived states is still undetermined (see text).

† J. Fallis *et al.*, CPT [18]

* C. Weber *et al.*, JYFLTRAP & SHIPTRAP [42]

Chapter 5

Discussion

5.1 Previous mass determinations, extrapolations and models

Because of the lack of data in the region on the proton-rich side of the valley of stability between elements Nb and Pd, our knowledge of these masses is primarily based on semi-empirical mass formulae or extrapolations from the observed systematics in the region. There are two primary types of semi-empirical formulas which attempt to determine potential masses from parameterized functions which are based on theoretical descriptions of nuclei. These two approaches are known as microscopic and macroscopic-microscopic approaches. Microscopic approaches attempt to build a function based on a solution to the Schrödinger equation from quantum mechanics (given in the opening paragraph) with specified forces between the nucleons and using a model wave function [61]. Macroscopic-microscopic approaches use the large scale liquid-drop model of the nuclear binding energy and correct for microscopic effects such as nucleon pairing and shell closures at the proton and neutron magic numbers [61]. An example of a microscopic model is the Hartree-Fock-Bogolyubov (HFB) mass formula. There are many different iterations of this formula as more nuclear properties have been included. The model and resulting masses which are discussed here are from HFB-17 [62]. An example of a macroscopic-microscopic formula is the Finite Range Droplet Model (FRDM) [63]. In both cases the formulas are

fit to the currently known masses (taken from the AME) and then used to extrapolate masses beyond the known data. The AME, in contrast, uses the systematic trends of smoothly varying¹ separation energy and reaction energy curves (S_{2p} , S_{2n} , $Q_{2\beta}$ and Q_{α}) to extrapolate masses for nuclides which have yet to be measured, but typically no more than 3 - 4 nuclides beyond the measured values. More information on these models and techniques can be found in their respective references and also in a review article by Lunney, Pearson and Thibault [61], which provides a broad comparison of these models and others which are not discussed here.

Comparisons of our measured values to the AME03 values (both measured and extrapolated) and to the masses determined from the FRDM and from HFB-17 are given in table 5.1 with a graphical comparison shown in figure 5.1. As the FRDM is based on the global behavior of the binding energy of nuclei, the masses which result generally vary from the results of new measurements in a systematic manner. In contrast, the masses predicted by the HFB-17 (which is based on the details of the interactions between the nucleons in an individual nucleus) often differ from newly measured data in a much more random manner.

The atomic masses predicted by these semi-empirical mass models typically have large uncertainties associated with them (669 keV for the FRDM [63] and 581 keV for HFB-17 [62]). Consequently, they are often less useful for astrophysical calculations than extrapolated AME values when they exist. Data on atomic masses on the proton-rich side of the valley of stability is available much nearer to the regions of astrophysical interest than on the neutron-rich side. Therefore, on the neutron-rich side of the valley of stability, these semi-empirical mass models are sometimes the only available option for such information.

Even where measurements exist, an evaluation, such as the AME, is required as not only are many different measurements often available for a single nuclide, they are

¹There are large and small scale changes to these curves due to proton and neutron shell closures and deformation regions but the similarity of the curve of one element or isotone to that of its neighbors provides constraints in these cases.

Table 5.1: Comparison of measured mass excesses to mass models

Nuclide	CPT	Mass excess (keV)						$\Delta_{\text{HFB-17}}^\ddagger$
		AME03	Δ_{AME03}	FRDM [†]	$\Delta_{\text{FRDM}}^\dagger$	HFB-17 [†]	HFB-17 [†]	
⁸⁷ Nb	-73891(26)	-74180(60)	289(65)	-73800	-91	-74650	759	
⁸⁷ Mo	-66887.1(4.1)	-67690(220)	803(220)	-66030	-857	-67380	493	
⁹⁰ Mo	-80171.9(4.3)	-80167(6)	-4.9(7.4)	-80440	268	-79110	-1062	
⁹¹ Mo	-82210.0(7.7)	-82204(11)	-6(13)	-82420	210	-82640	430	
⁹² Mo	-86806.8(6.4)	-86805(4)	-1.8(7.6)	-87170	363	-85660	-1147	
⁹⁰ Tc*	-70724.8(4.7)	-71210(240)	485(240)	-70600	-125	-70960	235	
⁹¹ Tc	-75986.0(5.5)	-75980(200)	-6(200)	-76220	234	-76800	814	
⁹² Tc	-78924.4(4.5)	-78935(26)	11(26)	-79000	76	-79220	296	
⁹³ Tc	-83613.6(5.1)	-83603(4)	-10.6(6.5)	-83880	266	-83550	-64	
⁹⁰ Ru	-64887(10)	-65310(300)#	423(300)#	-64290	-597	-66180	1293	
⁹¹ Ru	-68240.7(4.4)	-68660(580)#	419(580)#	-68010	-231	-69020	779	
⁹² Ru	-74306.6(4.3)	-74410(300)#	103(300)#	-74480	173	-73750	-557	
⁹³ Ru	-77217.5(2.4)	-77270(90)	53(90)	-77390	173	-78100	883	
⁹⁴ Ru	-82588.0(4.7)	-82568(13)	-20(14)	-83080	492	-81880	-708	
⁹² Rh	-63017(13)	-63360(400)#	343(400)#	-62580	-437	-63510	-493	
⁹³ Rh	-69016.5(4.1)	-69170(400)#	153(400)#	-69200	184	-68800	-217	
⁹⁴ Rh*	-72907.8(5.4)	-72940(450)#	32(450)#	-72870	-38	-72110	-798	
⁹⁵ Rh	-78329.5(9.5)	-78340(150)	10(150)	-78680	351	-77840	-490	

Indicates an extrapolated mass value

* Note that while the measured state is clear, the ordering of the long-lived states is still undetermined

(see sections 5.2.3 and 5.2.5).

†FRDM uncertainty = 669 keV

‡ HFB-17 uncertainty = 581 keV

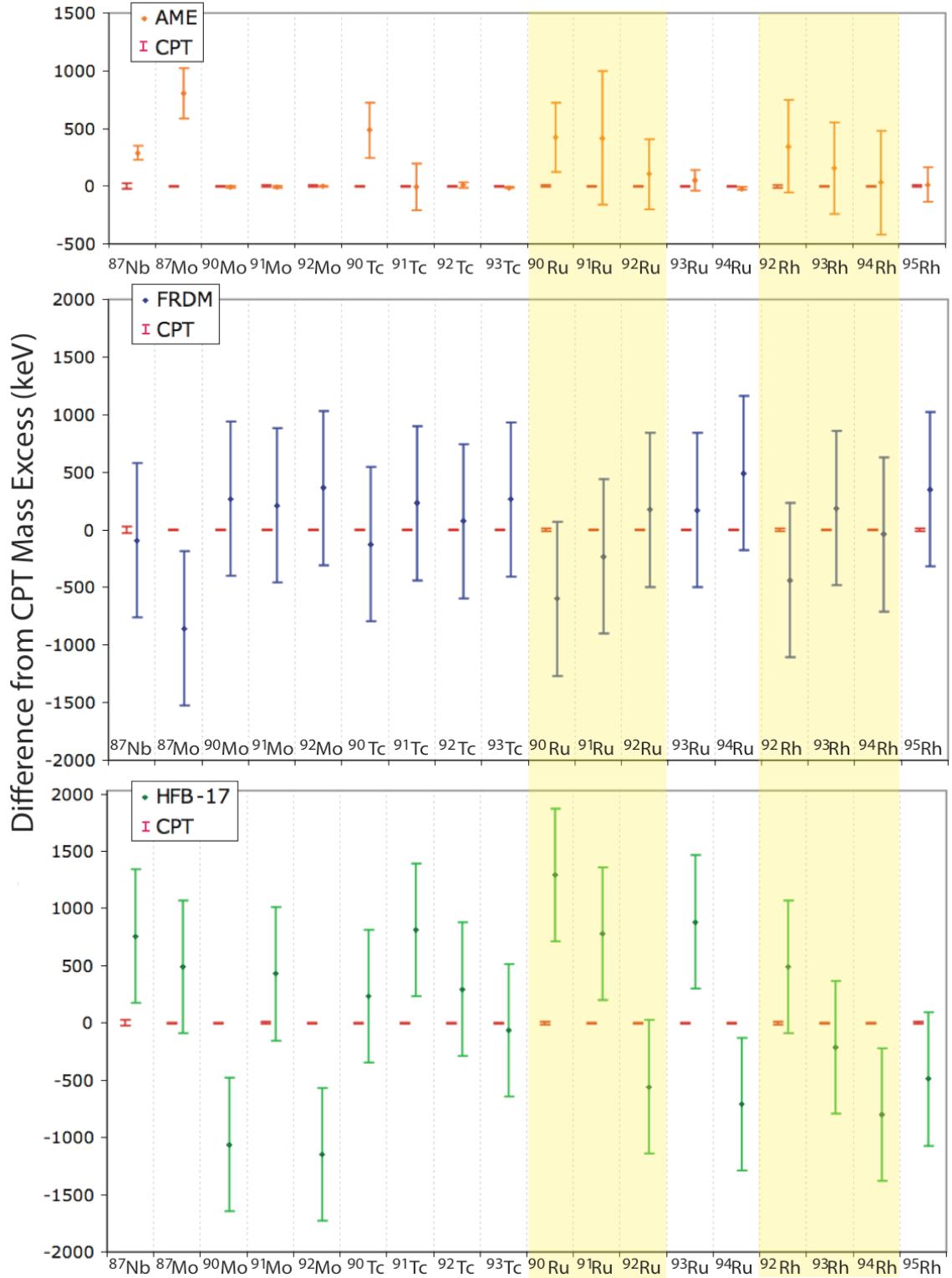


Figure 5.1: Comparison of measured mass excesses from the CPT with various mass models. Mass excesses for which there were no measured values available when these models were fit are highlighted in yellow.

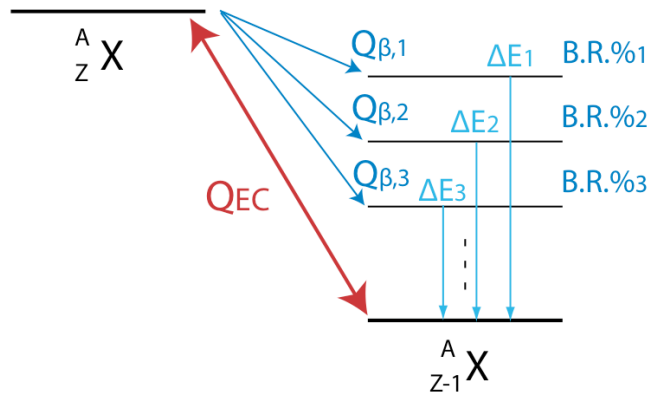


Figure 5.2: Calculating Q_{EC} from β -endpoint measurements involves knowing the branching ratios (B.R.) and energy levels of all of the states in the daughter nuclide into which the parent can decay.

typically a combination of direct measurements and reaction energies from a variety of different reactions. The AME is an important part of tying all of these multiply linked measurements together and determining a “recommended value” (based on solving an over-constrained set of linear equations that connect the masses). In cases where there is only a single measurement of a nuclide, it is compared to the systematic trends which result from nearby mass measurements as a means of confirming its validity.

In the comparison of our mass measurements to existing data the results of several types of reaction-based mass determinations will be discussed. These are mass excess determinations from

- i) electron capture Q values (Q_{EC}) calculated from β -endpoint energy measurements (figure 5.2),
- ii) proton capture Q value (Q_p) measurements,
- iii) transfer reaction Q -values from (p, t) reactions ($Q_{(p,t)}$), and
- iv) the measurements of β -delayed proton emission energies ($Q_{EC} - Q_p$).

The energy required for any given reaction is generally known as the reaction Q value and is defined in its most general form as follows:

$$M_{parent} + M_i - M_{daughter} - M_o = Q \quad (5.1)$$

where M_i is the mass of any incoming particle involved in the reaction and M_o is the mass of any outgoing particle(s) (see chapter 1).

The nuclear level structure of the nuclides in question becomes important when measuring reaction or decay energies as the reactions and decays can populate different states of the daughter nucleus. When isomers are involved, this nuclear structure information becomes even more critical and can affect the Penning trap measurements, if the half-life of the isomer is sufficiently long.

There is an added complication in the determination of reaction energies involving β decay. In single particle decays like p and α decay, the energy of the reaction is only shared between the ejected particle and the much heavier nucleus, and so the energy of the ejected particle corresponds to the energy of the reaction. β decay, in contrast, has a 3-body final state as the decay produces both a β particle and a neutrino (ν). Instead of the energy of the reaction being shared between only the one particle and the daughter nuclide, it is shared among three. If the energies of both the β and ν could be determined this would provide the same information as measuring the energy of one ejected particle in p or α decay. The ν however cannot be detected with any degree of efficiency, and so our knowledge of this reaction energy has to come entirely from the detection of the β particle, which can have any energy smaller than the total energy of the reaction. Measuring the distribution of β energies and fitting an expected distribution curve allows for the determination of the β -endpoint energy, which is the maximum β energy for this reaction and which corresponds to the Q_β value for that reaction. A cartoon illustrating the possible energies measured for the detected particle in these two cases (2-body and 3-body final states) is given in figure 5.3 along with the equations of these two types of reactions.

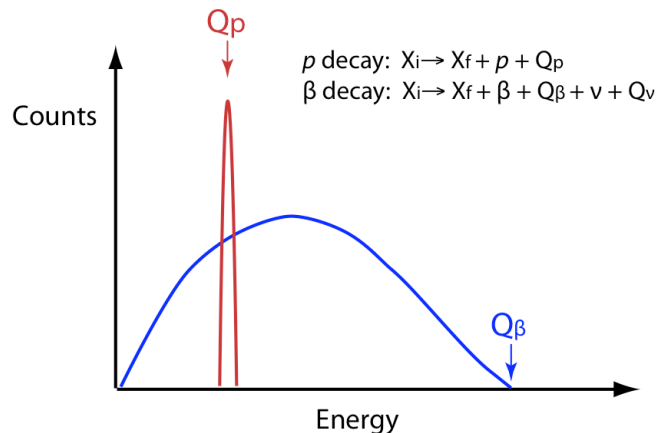


Figure 5.3: Cartoon showing the difference between a measurement of Q_p (or Q_α) and a measurement of a β -endpoint energy Q_β due to the reactions being, respectively 2-body and 3-body final states (the location of the values of Q_p and Q_β along the energy axis are completely arbitrary).

5.2 Comparison of our data to existing values

Due to the interest in the masses in this region we were not the only group which undertook the task of measuring the nuclides presented in this work. A combined effort by two other Penning trap groups, JYFLTRAP in Jyväskylä, Finland, and SHIPTRAP at the GSI facility in Germany, resulted in a paper by Weber *et al.* [42] which included measurements of 13 of the nuclides presented here. Due to the lack of data in this region, and with several of the newer measurements being in disagreement with previous data, the excellent agreement between these new measurements and ours provides a nice confirmation of both sets of results. This agreement can be seen in both table 4.4 and figure 4.3, and as such it will not be included in the discussion of each individual nuclide. It will instead be made clear when one of our values was not also measured by another Penning trap group.

The 18 masses measured for this thesis will be discussed on a case by case basis below. They are grouped by chemical element and presented in order of increasing atomic number, Z . Within each element the isotopes are presented from lightest to heaviest in order of increasing N , meaning that the isotope of each element closest to

the proton drip-line and furthest from the valley of stability will be presented first.

5.2.1 ^{87}Nb

Though the mass excess of $-73891(26)$ keV measured using the CPT is in agreement with the mass excess measured at JYFLTRAP [59], both trap measurements disagree with the AME03 value (see table 4.4 and figure 4.2). The CPT mass excess is found to be 289 keV heavier than the AME03 value, a difference of 4.4σ . There is a known isomeric state in ^{87}Nb but, as it is located only 3.84 keV above the ground state, it cannot be the cause of this discrepancy. This isomeric state falls well within the 26 keV uncertainty in our reported mass excess and so we can not say with certainty whether the ground state, excited state or a combination of the two states was measured.

There was only one measurement of the mass of ^{87}Nb available prior to the AME03 and it was a mass determination resulting from a β -endpoint measurement from the reaction $^{87}\text{Nb}(\beta^+)^{87}\text{Zr}$. The Q_{EC} value determined from this measurement was $5165(60)$ keV [64] and the mass determination of ^{87}Nb which results depends on both this Q_{EC} value and the mass of the daughter nuclide, ^{87}Zr . To determine the potential cause of the mass discrepancy between our mass excess and that from the Q_{EC} measurement we look first at the mass determination of ^{87}Zr . The mass of ^{87}Zr has been recently measured at JYFLTRAP to a precision of 5.3 keV and was found to be in agreement with the AME03 value [59]; this implies that the Q_{EC} value itself is in disagreement.

Source	Mass Excess (keV)	Reaction Energy (keV)	Ref.	Mass Excess (keV)	Source
CPT	<i>-73891(26)</i>	–		–	
JYFLTRAP[59]	<i>-73868(7)</i>	–		–	
Q_{EC} [64]	-74182(61)	<i>5165(60)</i>	^{87}Zr	-79348(8)	AME03[21]
	-74176(60)		^{87}Zr	-79341.4(5.3)	JYFLTRAP[42]

Table 5.2: List of mass excesses for ^{87}Nb either measured directly or determined from reaction energy measurements. The number in italics is the measured value.

Source	Mass Excess (keV)	Reaction Energy (keV)	Ref.	Mass Excess (keV)	Source
CPT	-66887.1(4.1)	–		–	
$Q_{EC,1}$ [64]	-67798(314)	<i>6382(308)</i>	^{87}Nb	-79348(8)	AME03[21]
	-67487(308)		^{87}Nb	-73869.6(6.8)	PT _{w.a.} from table 4.4
$Q_{EC,2}$ [65]	-67591(306)	<i>6589(300)</i>	^{87}Nb	-79348(8)	AME03[21]
	-67280(300)		^{87}Nb	-73869.6(6.8)	PT _{w.a.} from table 4.4
$Q_{EC} - Q_p$ [66]	-66812(301)	<i>3700(300)</i>	^{86}Zr	-79348(8)	AME03[21]
	-6969(300)		^{86}Zr	-77958(7)	JYFLTRAP[59]

Table 5.3: List of mass excesses for ^{87}Mo either measured directly or determined from reaction energy measurements. The number in italics is the measured value. The mass of the proton needed to determine the mass excess from the $Q_{EC} - Q_p$ value is given in table 4.3.

5.2.2 $^{87,90-92}\text{Mo}$

^{87}Mo

The mass excess of -66887.1(4.1) keV measured with the CPT is the first direct mass measurement of ^{87}Mo and is found to disagree with the AME03 mass excess by 803 keV (3.7σ).

Three experimental mass determinations were available prior to the AME03: two Q_{EC} determinations from the reaction $^{87}\text{Mo}(\beta^+)^{87}\text{Nb}$ [64, 65] and one measurement of $(Q_{EC} - Q_p)$ from the reaction $^{87}\text{Mo}(\epsilon p)^{86}\text{Zr}$ [66] (see table 5.3). As the values from the two different types of experiments disagreed only the two Q_{EC} measurements were included in the AME03 mass determination [20]. We find, however, that our ^{87}Mo mass excess is in agreement with that derived from the $^{87}\text{Mo}(\epsilon p)^{86}\text{Zr}$ experiment and disagrees with the mass excesses determined from the Q_{EC} measurements.

The masses of the daughter nuclides of both reactions have been recently measured. ^{86}Zr has been measured at JYFLTRAP and was found to be 158(30) keV lighter than the AME value [59]. The more recent mass measurements of ^{87}Nb are already discussed above and the resulting weighted average of the two Penning trap results given in table 4.4 (-73869.6(6.8) keV) is 311 keV heavier than the AME03 value. As both masses have changed, the mass determinations for all three decay en-

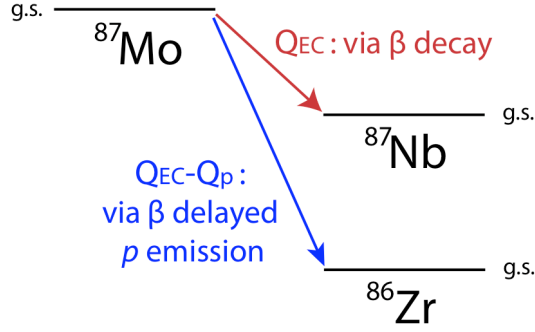


Figure 5.4: The daughter nuclides of the ^{87}Mo decays associated with the Q_{EC} and $(Q_{EC} - Q_p)$ decay energies.

ergy measurements have been recalculated. The ^{87}Mo mass excess determined from the $(Q_{EC} - Q_p)$ measurement remains in agreement with our reported value. The change in the mass of ^{87}Nb brings the mass excesses calculated from the two Q_{EC} measurements into agreement with the mass excess calculated from the $(Q_{EC} - Q_p)$ value. It is not enough of a shift, however, for the ^{87}Nb mass excesses from the Q_{EC} measurements to be in agreement with our reported mass excess. A graphical comparison is shown in figure 5.5.

^{90}Mo

For this nuclide only the ground state has a half-life long enough to have been measured with the CPT ($t_{\frac{1}{2}} = 5.56(9)$ h). Our measured value is in agreement with the AME03 value [21] (see table 4.4 or 5.1).

This is the first direct mass measurement of this nuclide, with the only previous mass determination resulting from one Q_{EC} value for the decay $^{90}\text{Mo}(\beta^+)^{90}\text{Nb}$ [67]. As the uncertainty in our mass excess is 4.3 keV it is 1.4 times smaller than the current AME03 uncertainty thus improving the precision to which this mass is known.

^{91}Mo

This nuclide does have a known isomeric state with a half-life long enough to have been measured in the CPT ($t_{\frac{1}{2}} = 63.6(6)$ s) but as the excitation energy of this state

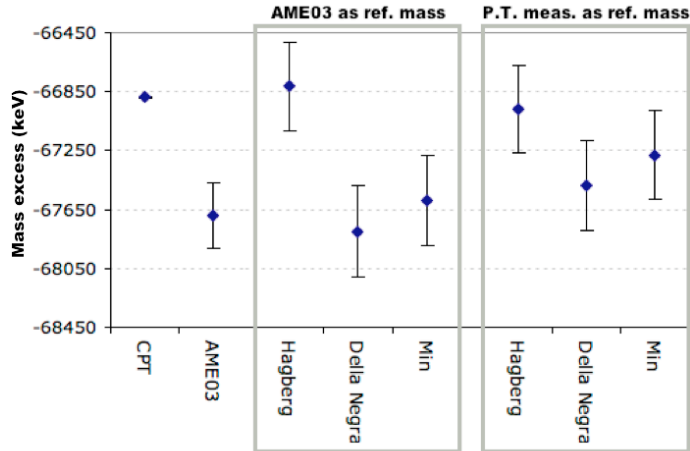


Figure 5.5: Comparison of ^{87}Mo mass excess values. Shown on the left are both our measurement and the AME03 value. Also shown are the previous experimental mass determinations. The resulting ^{87}Mo mass excesses from each are given using either the AME03 values or the more recently measured Penning trap (P.T.) measurements as the reference mass. Min *et al.* [65] and Della Negra *et al.* [64] measured Q_{EC} values and Hagberg *et al.* measured a $(Q_{EC} - Q_p)$ value.

is 653.01(9) keV, our experimental resolution of 191 keV would have been sufficient to resolve these two states had both been present in the trap. Only the ground state was seen and our measured value corresponds to that presented in the AME03 [21]. This is the first direct measurement of ^{91}Mo and, with an uncertainty of 7.7 keV, it is 1.4 times more precise than the AME03 value [21].

^{92}Mo

This nuclide is a stable nuclide and so there have been many previous mass determinations. Two of these were direct measurements using deflection mass spectrometers [68, 69] (with one of these measurements having been performed with a precursor of the Manitoba II mass spectrometer [7] which was located at McMaster University [68]). Our measured value is in agreement with the value from the AME03 which is based primarily on these two measurements and two Q_n measurements from the reaction $^{92}\text{Mo}(n, \gamma)^{93}\text{Mo}$ [21].

5.2.3 $^{90-93}\text{Tc}$

^{90}Tc

This nuclide has two long-lived states with tentatively assigned spins of (1^+) and (8^+) [72]. As fusion-evaporation reactions tend to favor high-spin states, Weber *et al.* [42] assigned their measurement to the (8^+) state. This assignment is supported by our ^{90}Tc measurements, the first of which used the same beam, target and energy as in the γ decay work by Rudolph *et al.* [73] in which only the (8^+) long-lived state was populated.

While we know which state we have measured, it is not clear whether this state is the ground state of ^{90}Tc or its isomeric state. There is only one previous measurement of the (8^+) state which was a Q_{EC} value measurement by Oxorn *et al.* [70] and our value is in agreement with this measurement within its uncertainty. The (1^+) state was also measured by Oxorn *et al.* [70] with another measurement having been presented previously by Iafigliola *et al.* [71]. Oxorn *et al.* [70] assigned the (8^+) spin state to the isomer and the (1^+) state to the ground state based on their Q_{EC} values which were $Q_{EC(J=1^+)} = 9.3 \pm 0.3$ MeV and $Q_{EC(J=8^+)} = 8.8 \pm 0.3$ MeV. As a larger decay energy means a larger mass difference between the parent state and the daughter nuclide, the state with the larger Q_{EC} value, that of the (1^+) state, was taken to be the isomeric state. The large uncertainties associated with these measurements, however, keep this level assignment from being conclusive. Papers by Rudolf *et al.* [73] and Dean *et al.* [74] make cases to reverse this level assignment. Rudolf *et al.* base their state assignment on local energy-level systematics such as the fact that neighboring odd-odd nuclei $^{88,90}\text{Nb}$ and ^{92}Tc have 8^+ ground states. Dean *et al.* present shell model calculations which favor high-spin ground states and suggest a low spin isomer. Added to this, the work by Weber *et al.* [42] looks at the systematics of two proton separation energies, S_{2p} , along the $N=47$ isotone (nuclides with the same neutron number N) and find that their measured value of the (8^+)

Source	State	Mass Excess (keV)	Reaction Energy (keV)	Ref.	Mass Excess (keV)	Source
CPT	(8 ⁺)	-70724.8(4.7)	–		–	
Other PT [42]	(8 ⁺)	-70723.7(3.4)	–		–	
Q_{EC} [70]	(8 ⁺)	-70867(300)	9300(300)	⁹⁰ Mo	-80167(6)	AME03[21]
$Q_{EC,1}$ [71]	(1 ⁺)	-71037(410)	9130(410) [†]			
$Q_{EC,2}$ [70]	(1 ⁺)	-71367(300)	8800(300)	⁹⁰ Mo	-80167(6)	AME03[21]
$Q_{EC,avg}$ [20]	(1 ⁺)	-71207(240)	8960(240)			
$Q_{EC,1,corr}$	(1 ⁺)	-70507(410)	9660(410)	⁹⁰ Mo	-80167(6)	AME03[21]
$Q_{EC,corr,avg}$	(1 ⁺)	-71022(240)	9145(240)			

[†] This value is taken from the AME03 [20] as the paper by Iafigliola *et al.* gives their resulting mass excess instead of the Q_{EC} value but is not clear which mass they used for the daughter nuclide.

Table 5.4: List of mass excesses for ⁹⁰Tc either measured directly or determined from reaction energy measurements. The numbers given in italics are the measured values.

state fits the systematics better than a determination of the (1⁺) state calculated from their measured value.

The energy difference between the states which is given by the NUBASE evaluation (an evaluation of nuclear and decay properties) is 310(390) keV [75]. This value has been derived from the Q_{EC} energy differences discussed above. Weber *et al.* [42] point out that the branching ratio used to calculate the $Q_{EC(J=1+)}$ value which was measured by Iafigliola *et al.* [71] is inverted from that found later by Oxorn *et al.* [70]. Applying the branching ratio from Oxorn *et al.* to the Iafigliola *et al.* measurement results in a different value of $Q_{EC(J=1+)}$. The new weighted average of the Iafigliola *et al.* and Oxorn *et al.* measurements is then found to be $Q_{EC(J=1+)} = 9145(240)$ keV. The Q_{EC} from the (1⁺) state remains lower than the (8⁺) state but the resulting difference between the two long-lived states is found to be 124(390) keV instead of the 310(390) keV which was given above. This change in $Q_{EC(J=1+)}$ also affects the mass excess of the ground state of ⁹⁰Tc which is determined from this Q_{EC} value. The resulting ⁹⁰(^{J=1+})Tc mass excess is 185 keV higher than the AME03 value. The excitation energy which results from the difference between our measurement of the (8⁺) state and the mass excess determined from the corrected $Q_{EC(J=1+)}$ value is 297(240) keV.

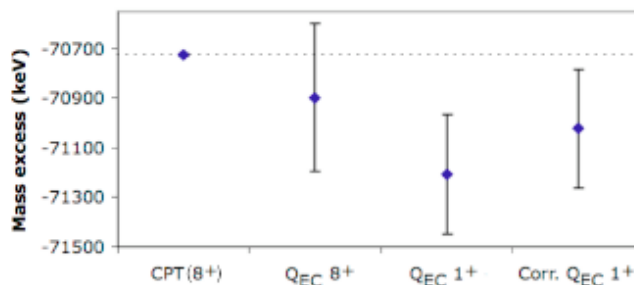


Figure 5.6: A comparison of the ^{90}Tc mass excesses. The source of the mass excesses are shown on the horizontal axis. Supporting data from the AME03 was used as necessary. The Q_{EC} (1⁺) value is the weighted average of the Oxorn [70] and Iafigliola [71] values as presented in the AME03. The “corrected” Q_{EC} (1⁺) value is the weighted average of the Oxorn and Iafigliola values corrected as described in the text.

A graphical comparison can be seen in fig. 5.6

If Rudolf *et al.* [73], Dean *et al.* [74] and Weber *et al.* [42] are correct in their assignment of the (8⁺) state as the ground state of ^{90}Tc , then the energy difference between states cannot just be taken to be the difference in Q_{EC} values as the lower Q_{EC} value corresponds to the higher energy state. We might expect that, given the large uncertainties, an upper limit of this excitation energy could be assigned as the difference between the upper limit of the $Q_{EC(J=1^+)}$ value and the lower limit of the $Q_{EC(J=8^+)}$ value (fig. 5.7). Unfortunately the direct mass measurements place the $^{90(J=8^+)}\text{Tc}$ mass excess outside of the overlap between these two Q_{EC} values so this does not appear to be the case. This suggests that either the (1⁺) state is the ground state of ^{90}Tc or that there is some systematic effect such as an unaccounted for state or incorrect branching ratio used to determine the $Q_{EC(J=1^+)}$. Typically it is preferred to take measured data over systematic arguments, however the arguments for an (8⁺) ground state based on the S_{2p} values is quite compelling and the previous discussions of ^{87}Nb and ^{87}Mo have shown that Q_{EC} values in the lesser studied regions of the chart of the nuclides can be prone to systematic effects potentially resulting from the lack of knowledge in the region.

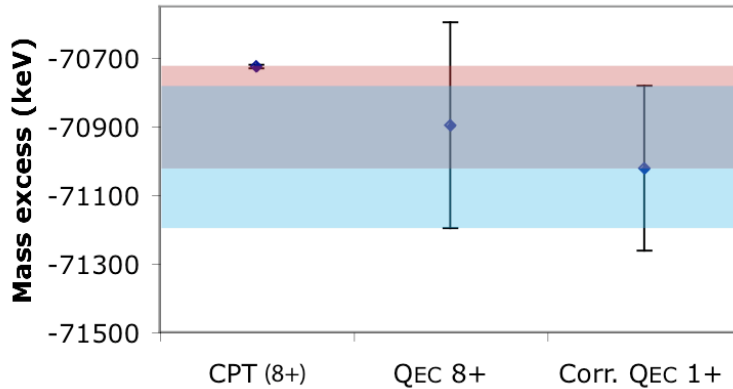


Figure 5.7: Our measurement of the ^{90}Tc mass excess is given along with the mass excess determined from the Q_{EC} measurements discussed in the text. The region in green indicates the expected excitation energy if the (1^+) state is the ground state and the (8^+) state is the isomer. The blue region indicates the expected upper limit of the excitation energy if the state assignment happens to be reversed.

Looking at how the assignment of our measurement to the ground or isomeric state affects the systematic trends of the newly measured values presented in section 5.4, given the excitation energy of 297(240) keV determined above, we find that the systematic trends support the case for the (8^+) state being assigned as the ground state. If the excitation energy is found to be smaller than 297 keV, however, this argument will become less convincing. Preferably further studies of the ^{90}Tc level structure will be undertaken. Until such a time our measured value for ^{90}Tc will be taken as a measurement of the ground state.

If the energy difference between the ground and isomeric states is found to be less than our mass resolution of 191 keV we would not have been able to resolve the two states. As previously discussed however, we do not expect to have produced the (1^+) state of ^{90}Tc and so no correction was applied to our reported mass and uncertainty.

^{91}Tc

This nuclide has a known isomeric state with a half-life long enough to have been measured in the CPT ($t_{\frac{1}{2}} = 3.3(1)$ min). As the energy level of this state is 139.3(3) keV,

with our experimental resolution of 100 keV the two states could be clearly resolved by our spectrometer if both were present and we are confident in assigning of our mass measurement to the ground state. The mass of ^{91}Tc is in agreement with the AME03 value [21] but provides a significant improvement in the precision as our uncertainty is 34 times smaller.

^{92}Tc

For this nuclide only the ground state has a half-life long enough to have been measured with the CPT ($t_{\frac{1}{2}} = 4.25(15)$ min). Our measured mass excess is found to be in agreement with AME03 value [21] but improves on the AME03 precision by a factor of 5.5.

^{93}Tc

This nuclide has an isomer which is known to be 391.84(8) keV above the ground state. As this isomeric state is well outside our experimental mass resolution of 191 keV we assign our measurement to the ground state of ^{93}Tc .

Comparing our mass excess to that in the AME03 we find that our measured mass excess for ^{93}Tc is lighter than the AME03 value by 10.6 keV (1.6σ). The AME03 mass determination is based on one Q_p measurement from the reaction $^{92}\text{Mo}(p, \gamma)^{93}\text{Tc}$ which found $Q_p = 4086.5 \pm 1.0$ keV [76]. Similarly to the Q_{EC} and $(Q_{EC} - Q_p)$ measurements already discussed, the mass determination from this reaction energy

Source	Mass Excess (keV)	Reaction Energy (keV)	Ref.	Mass Excess (keV)	Source
CPT	<i>-83613.6(5.1)</i>	–		–	
Q_p [76]	-83602.5(4.1)	<i>4086.5(1.0)</i>	^{92}Mo	-86805(4)	AME03[21]
Schottky Mass Spec.[77]	<i>-83582.0(28.5)</i>	–		–	

Table 5.5: List of mass excesses for ^{93}Tc either measured directly or determined from reaction energy measurements. The numbers presented in italics are the measured values. The mass of the proton needed to determine the mass excess from the Q_p value is given in table 4.3.

Source	State	Mass Excess (keV)	Reaction Energy (keV)	Ref.	Mass Excess (keV)	Source
CPT	g.s.	<i>-68240.7(4.4)</i>	–		–	
Other PT[42]	g.s.	<i>-68237.1(2.9)</i>	–		–	
$Q_{EC} - Q_p$ [66]	i.s.	> -68578	> 4300	^{90}Mo	-80167(6)	AME03[21]

Table 5.6: List of mass excesses for ^{91}Ru either measured directly or determined from reaction energy measurements. The $(Q_{EC} - Q_p)$ value by Hagberg *et al.* [66] is only a lower limit. The numbers presented in italics are the measured values. The mass of the proton needed to determine the mass excess from the $(Q_{EC} - Q_p)$ value is given in table 4.3.

	Beam	Target	Energy (MeV)	State Produced
Arnell <i>et al.</i> [79]	^{40}Ca	^{58}Ni	187	g.s. only
Heese <i>et al.</i> [78]	^{36}Ar	^{58}Ni	149	g.s. only
Experiment 3	^{36}Ar	$^{\text{Nat}}\text{Ni}$	130	
Experiment 4	^{36}Ar	^{58}Ni	125	
Experiment 5	^{40}Ca	^{58}Ni	187	

Table 5.7: Beams, targets and energies used to produce ^{91}Ru . The two previous studies only produced the ground state of ^{91}Ru .

isomeric state is unknown, so too is the ground state mass of ^{91}Ru . The NUBASE evaluation [75] provides an energy difference of 80(300) keV based on systematics and this was used to determine the ground state mass excess presented in the AME03. Our reported mass excess is 419 keV heavier than the AME03 value but still agrees within its uncertainty.

As the resolution of our measurement was 100 keV we would not have been able to resolve these two states if both were present in the CPT. It was discussed in section 4.2.4 that if two unresolved isomers are present in the trap, the mass that is measured is the center of mass of all ions [57]. This could potentially result in an unaccounted shift in the measured ω_c value and a resultant systematic shift in the measured mass. To determine if an additional systematic uncertainty should be included in our final uncertainty we attempt to determine the relative production of each state as the relative number of each ion species determines the size of this

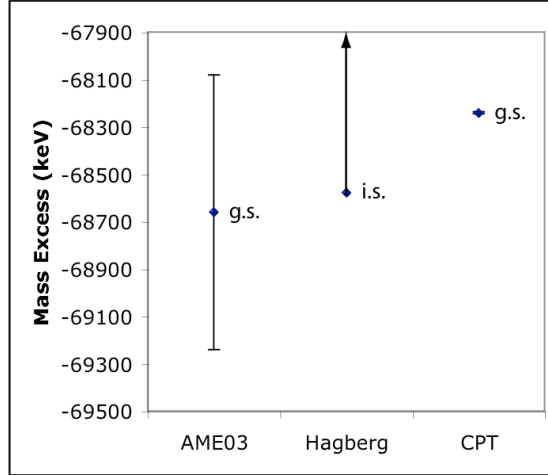


Figure 5.9: Comparison of ^{91}Ru mass excesses. Note that the AME value [20] is calculated from the value by Hagberg *et al.* [66] and not based on any other measurements.

potential systematic effect.

The relative production for these two states in our fusion-evaporation reaction is expected to be similar to that which was seen in previous studies of this nuclide using fusion-evaporation reactions. There are two such studies (see table 5.7). Only one of our experiments (experiment 5) matched one of these two studies exactly in terms of beam, target and energy. Experiment 3 and 4 used the same beam as Heese *et al.* [78] but at a lower energy. Experiment 3 also used a natural Ni target instead of the enriched ^{58}Ni target but this experiment carries the least weight in the determination of our final mass for ^{91}Ru (table 4.2). With both of the previous fusion-evaporation studies producing only the ground state of ^{91}Ru we also expect to have produced and measured the ground state, with no correction needed to account for possible isomeric contamination.

As our mass excess value is higher than the lower limit of the isomeric mass excess determined from the $(Q_{EC} - Q_p)$ measurement by Hagberg *et al.* (see table 5.6 and figure 5.9), we cannot at this point make any inference as to the energy difference between the two states. Using our measurement of the ground state and the excitation

energy from the NUBASE evaluation [75], the isomer would be expected to have a mass excess of -68161(300) keV.

⁹²Ru

Only the ground state of this nuclide has a half-life long enough to have been measured with the CPT ($t_{\frac{1}{2}} = 3.65(5)$ min). The measured mass excess is found to be 103 keV heavier than the AME03 value but still within the uncertainty of this extrapolated value [21]. Our measurement of ⁹²Ru was the first published measurement of this mass [18] and improves on the precision of the extrapolated AME03 value by a factor of 70.

⁹³Ru

This nuclide is known to have an isomer with a half-life long enough to have been measured in the CPT ($t_{\frac{1}{2}} = 10.8(3)$ s). As its excitation energy is 734.40(10) keV, with an experimental resolution of 191 keV both states could be easily resolved if both were present in the trap. We assign our measurement to the ground state of ⁹³Ru. Our mass measurement of ⁹³Ru is in agreement with the AME03 value [21] and improves on the AME03 precision by a factor of 38.

⁹⁴Ru

The mass excess of ⁹⁴Ru presented in this work is found to be 20 keV (1.5σ) lighter than the AME03 value [21]. The value measured by Weber *et al.* [42], with which our value agrees, falls between our value and the AME03 and is in agreement with both.

The source of the AME03 value is one Q-value measurement for the reaction ⁹⁶Ru(p, t)⁹⁴Ru [20, 80]. The reference mass, ⁹⁶Ru needed to calculate the ⁹⁴Ru mass from this measurement has not been remeasured since the AME03 [21] but, as ⁹⁶Ru is a stable nuclide, its mass has been determined extensively (both directly and through various reactions) and is not expected to change.

5.2.5 $^{92-95}\text{Rh}$

^{92}Rh

Our mass excess is 343 keV heavier than the extrapolated AME03 value but is still in agreement due to the large uncertainty in the AME03 value. No isomer is reported in the Nuclear Data Sheets [81] or the NUBASE evaluation [75], however Dean *et al.* [74] suggest a possible isomer in ^{92}Rh based on a 2-component fit to the β -decay lifetime and a larger than expected feeding from the ^{92}Rh ground state to the lower levels of ^{92}Ru (given a (6^+) spin for the ^{92}Rh ground state). The lifetime of this second long-lived state is reported to be 0.53 s [74] which is long enough to have been measured if present in the trap. It has been tentatively assigned to the (2^+) state of ^{92}Rh .

Several shell model calculations [74, 82, 83] indicate a (2^+) state below the (6^+) state currently considered to be the ground state. Kast *et al.* [82] and Dean *et al.* [74] find this (2^+) state to be ~ 50 keV below the (6^+) ground state and also find a (4^+) state ~ 50 keV above. Herndl and Brown [83] calculate both the (2^+) and (4^+) state to be below the 6^+ state by 211 keV and 57 keV respectively. A recent shell model study by Kaneko *et al.* [84], however, does not report these (2^+) and (4^+) states.

As our resolution for the ^{92}Rh measurements was 342 keV we would not have been able to resolve the two long-lived states if both were present in the trap. As with ^{91}Ru , we look to production information from previous studies of this nuclide using fusion-evaporation reactions to determine if any correction due to the potential presence of this isomeric state is required.

A recent level structure study by Pechenaya *et al.* [85], which used the same beam and target combination as our measurements but at a slightly lower beam energy (see table 5.8) did not report seeing either the (2^+) or (4^+) state. An earlier measurement by Kast *et al.* [82] which, again, used the same target and beam combination also did not report seeing a (2^+) or a (4^+) state. Dean *et al.* [74], the only paper which did report seeing this second long-lived state, used a different beam at a much lower

	Beam	Target	Energy (MeV/u)	States Produced
Pechenaya <i>et al.</i> [85]	^{58}Ni	^{40}Ca	4.14	(6 ⁺) only
Kast <i>et al.</i> [82]	^{40}Ca	^{58}Ni	4.5	(6 ⁺) only
Dean <i>et al.</i> [74]	^{36}Ar	^{58}Ni	3.3	(6 ⁺)=95(2)% , (2 ⁺)=5(2)%
Experiment 7 & 8	^{40}Ca	^{58}Ni	4.75	

Table 5.8: Beams, targets and energies used to produce ^{92}Rh .

energy (table 5.8). The relative production of these two states determined from the areas under the associated γ peaks in [74], finds that 95(2)% of the isotopes produced are in the (6⁺) state and the remaining 5(2)% are in the 0.53 s state tentatively assigned as the (2⁺) state [74].

Based on the production information alone, we do not expect to have produced the (2⁺), 0.53 s state. Even if we assume a “worst case scenario” based on the production seen by Dean *et al.* [74], where 5% of the ions measured were in this second state, using an assumed energy difference of 50 keV, our measured value for the (6⁺) state would only shift by 2.35 keV. This shift falls well within our experimental uncertainty. Reducing this possibility even further is the fact that the time from production to detection of the ions in this ^{92}Rh measurement was on the order of ~ 0.5 s, which is roughly equal to the half-life of the (2⁺) state. No correction to our uncertainty to account for possible isomeric contamination is deemed necessary at this time.

^{93}Rh

Our previously published value for this nuclide [18] (the first published measurement of this mass), was published prior to performing the last experiment which is presented in this work (experiment 8). The value measured in this last experiment however, disagrees with our published value by 12.2 keV (1.4 σ). Due to this discrepancy the previous data and analysis was revisited – nothing was found to be amiss. All nuclides measured and presented in this work were checked for evidence of a systematic discrepancy in one of the 3 experiments in which ^{93}Rh was measured – no evidence

of any systematic effect was found.

This change in the ^{93}Rh mass affects our published value for $S_p(^{93}\text{Rh})$ which is now found to be 1999(6) keV as opposed to 2007(9) keV which was reported in [18]. As the value for $S_p(^{93}\text{Rh})$ remains within our previously reported uncertainty this change does not affect our published conclusions (which will be discussed in section 5.5.1).

Both values agreed with the extrapolated AME03 value within uncertainty, though they are ~ 153 keV heavier. Our most recent measurement and the resulting weighted average of all of our measurements both agree with the value reported by Weber *et al.* [42].

^{94}Rh

This nuclide has two known long-lived states, a (4^+) state with a 71 s half-life and an (8^+) state with a 26 s half-life. The energy difference provided in the 2003 NUBASE evaluation determined from systematic trends is 300(200) keV [75]. Prior to the 2003 NUBASE and AME evaluations there had only been one measurement of either of these states; Oxorn *et al.* [86] determined a Q_{EC} value for the (4^+) state of ^{94}Rh which they assigned as a measurement of the isomeric state. The AME03, which uses the state assignments from the NUBASE evaluation, assigns the (4^+) state as the ground state of ^{94}Rh and assigns the (8^+) state as the isomer [75]. The AME03, however, still assigns the measurement by Oxorn *et al.* to the isomeric state even though the spin assignments are reversed [20]. This could explain why our reported mass excess for ^{94}Rh is only 32 keV heavier than the extrapolated ground state AME03 value, even though we expect to have measured the (8^+) state.

There are several reasons why we expect to have measured the (8^+) state, one being that fusion-evaporation reactions generally produce higher spin states. Weber *et al.* [42] make the case for (8^+) being the sole state produced in the $^{40}\text{Ca}+^{58}\text{Ni}$ fusion-evaporation reaction using data from GSI which determined that the 26 s, (8^+) state was produced in the fusion-evaporation reaction and that the 71 s, (4^+) state

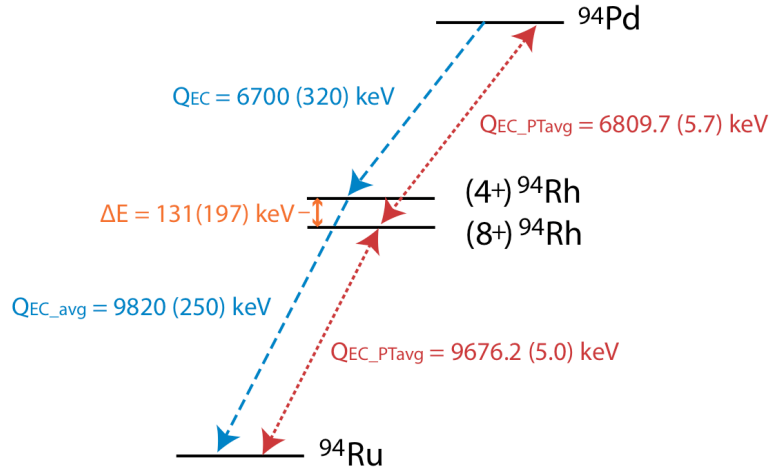


Figure 5.10: The energy level difference of long-lived ^{94}Rh states (orange, solid) as determined from the measured Q_{EC} values (blue, dashed) [89, 86] as compared to the Q_{EC} values calculated from the weighted averages of the Penning trap masses (red, dotted).

was populated as a result of β decay from the ^{94}Pd also produced in the reaction [87]. We add to this a production argument again based on observed production states in level structure studies performed previously. Studies by Arnell *et al.* [88] used a ^{40}Ca beam at 180 MeV on a ^{58}Ni target and produced only the (8^+) state. We measured ^{94}Rh in two experiments both of which used the same beam and similar energies (170 MeV and 190 MeV). While our experiment using the 190 MeV beam used a ^{58}Ni target, the same as was used by Arnell *et al.*, our experiment using the 170 MeV beam used a natural Ni target (68% ^{58}Ni). Given all the arguments above we assign our measurement to the (8^+) state.

Since the last Atomic Mass Evaluation, Batist *et al.* [89] have determined Q_{EC} values from the ground state of ^{94}Pd to the (4^+) state of ^{94}Rh and from this (4^+) state to the ground state of ^{94}Ru (figure 5.10). Using the preliminary values from the first 3 of the 8 experiments presented in this paper, which were originally presented in a diagram in the ENAM04 proceedings [90], Batist *et al.* provide the first experimental indication that the (8^+) state might in fact be the ground state of ^{94}Rh . They make

the assumption that the fusion-evaporation reactions would have produced the higher spin state and then show that the Q_{EC} for $^{94(J=4^+)}\text{Rh}$ to ^{94}Ru is in fact larger than that which can be derived from the difference between the $^{94(J=8^+)}\text{Rh}$ mass measurement and the AME03 ^{94}Ru value. Unfortunately the large uncertainties in the Q_{EC} values keep this from being conclusive. Weber *et al.*, having measured all three corresponding masses: ^{94}Pd , $^{94(J=8^+)}\text{Rh}$ and ^{94}Ru , confirm the argument by Batist *et al.* We confirm the mass measurements of $^{94(J=8^+)}\text{Rh}$ and ^{94}Ru presented by Weber *et al.* and also find that the value Batist *et al.* drew from the graph of preliminary data presented in [90] is equal within his stated uncertainty to that which is presented here. Using the weighted average of the Penning trap measurements of ^{94}Pd , $^{94(J=8^+)}\text{Rh}$ and ^{94}Ru , and the Q_{EC} values from Batist *et al.* [89] and Oxorn *et al.* [86] the energy difference between the two long-lived states is determined to be 131(197) keV. See figure 5.10.

The shell model calculations presented by Batist *et al.* [89], as well as that presented by Kaneko *et al.* [84] the (8^+) state is found to be lower than the (4^+) state.

While we do not expect to have produced the (4^+) state of ^{94}Rh , with a resolution for these measurements of 100 keV it is possible that we would not have been able to resolve the two states, were they both produced. Assuming an energy difference of 100 keV (as an energy difference any larger would be able to be resolved) we find that to cause a shift in our measured value for the (8^+) state larger than our experimental uncertainty, more than 5% of the ions present would need to be in the (4^+) state. From both this and the production arguments, we determine that even if the energy difference between the states is found to be ≤ 100 keV no correction to our uncertainty to account for possible isomeric contamination is necessary.

^{95}Rh

This nuclide is known to have an isomeric state with a half-life long enough to have been measured in the CPT ($t_{1/2} = 1.96(4)$ min) but, as this isomeric state has an excitation energy of 543.3(3) keV, with an experimental resolution of 191 keV, we are

confident in the assignment of our mass measurement as measurement of the ground state. Our mass measurement of ^{95}Rh is in agreement with the AME03 values [21].

5.3 Separation energy systematics

The variation of the nuclear binding energy across the landscape of the chart of the nuclides can provide insights into the underlying physics of nuclear binding. This is most easily viewed by plotting the separation energies of protons or neutrons as they vary with Z or N (as the shell structures of protons and neutrons are largely independent). As pairs of like nucleons are more bound than single nucleons, separation energy trends are often plotted as 2-proton or 2-neutron separation energies (S_{2p} or S_{2n}). This eliminates the oscillations in the S_p or S_n curves due to pairing effects (for an example of this, compare figures 5.11 and 5.12). The smoothness of plots of these 2 nucleon separation energies in regions which do not include shell closures was exploited for the mass extrapolations presented in the AME. In regions where shell closures do exist, the similarity of nearby curves is used to determine the extrapolated values. In the S_{2n} graph (figure 5.13), the effect of a shell closure on the neutron separation energies is clearly seen at the neutron “magic number” $N = 50$, where there is a sharp decrease in the energy required to remove a neutron (or two in the case of this graph) above the shell closure ($N=51,52$, etc.) as compared to nuclei of the same element below the shell closure ($N \leq 50$).

Looking at the S_{2p} systematics presented in fig. 5.11 we find the agreement between the AME S_{2p} curves (including the extrapolated values), and the curves involving our measured values is generally good, except in the cases where one of our measurements has been used in combination with an extrapolated AME03 value to determine the S_{2p} value (this will be discussed further in the following paragraph). Note that even the values with the largest deviations between the S_{2p} values from the CPT measurements and the AME03 extrapolations, $S_{2p}(^{90,91}\text{Ru})$, are within the large AME03 uncertainty.

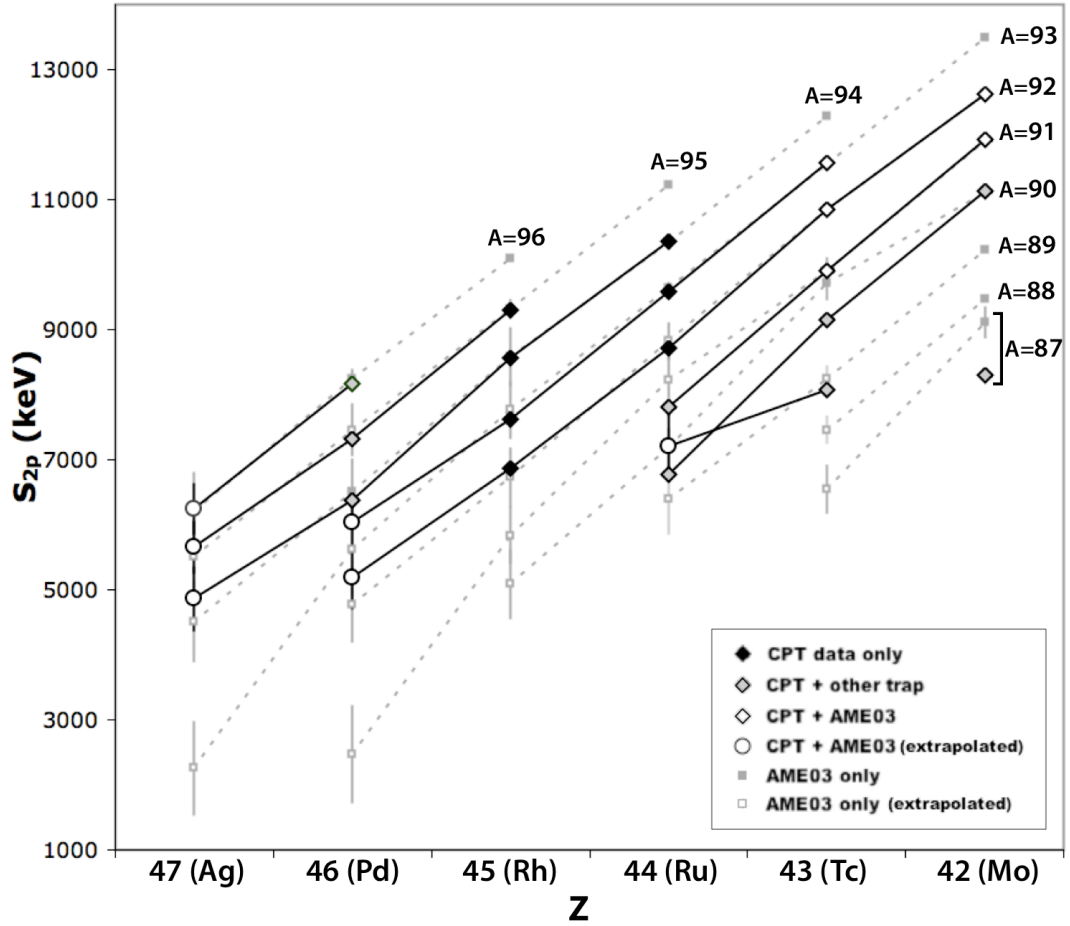


Figure 5.11: The S_{2p} values calculated from our mass measurements are presented here along with the AME03 S_{2p} values for comparison. Each point is derived from two mass values and the source of each of these values is identified in the legend. The other Penning trap values used are from [42, 59]. All the points shown have error bars, there are some cases however where the error bars are smaller than the data points.

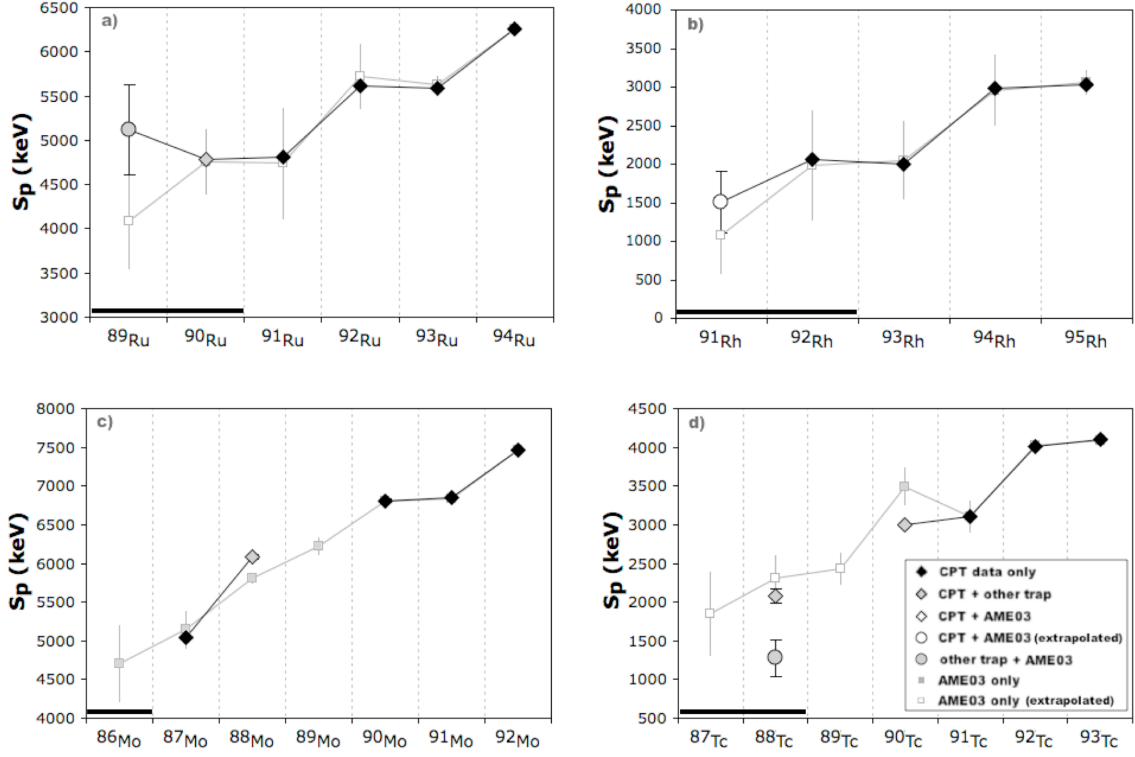


Figure 5.12: Plots of the calculated S_p values for Mo, Tc, Ru and Rh. The legend in fig. 5.12d) applies to all four figures. The thick black bar just above the x-axis on the left of all four figures indicates which nuclides lie along the primary path of the rp process [25]. The other Penning trap values used are from [42, 59]. Error bars are plotted for all the data points, however some are smaller than the size of the data point on the graph.

The values for $S_{2p}(^{90}\text{Tc})$ and $S_{2p}(^{87}\text{Mo})$ differ from the AME03 values by more than the uncertainty, however in both cases this is due to discrepancies in the measured values and not due to the AME03 extrapolations. The $S_{2p}(^{90}\text{Tc})$ deviation is a result of the difference between our measured value of ^{90}Tc and the AME03 ground-state mass excess. The deviation of the $S_{2p}(^{87}\text{Mo})$ value is due to the discrepancy between our measurement of ^{87}Mo and the previously measured values. Even with the good agreement of all of the other S_{2p} values we find that the measured values can disagree with the extrapolated values by as much as 430 keV (as in the case of ^{90}Ru). This, combined with the significant gain in precision which results, clearly illustrates the need for measured values.

While the systematic curves are not dramatically different between our measured values and the AME values, where a combination of our measurements and extrapolated AME03 values have been used to calculate the S_{2p} value (the data points indicated by open circles in figure 5.11) there are large deviations. This is not a new feature in the nuclear binding but rather an artifact of the increasing difference between measured and extrapolated values for the nuclides increasingly further from previously measured values. As the systematics of differences between masses (S_{2p} , S_{2n} , $Q_{2\beta}$ and Q_{α}) are used to determine the extrapolated AME03 mass values [20, 21], the prediction of differences between masses are often better than the predictions of the masses themselves (an example of this is seen in section 5.4). A calculation of any mass difference using one of our newly measured masses with an extrapolated mass is at a clear disadvantage because of this.

The S_p values associated with our measured values as compared to those calculated from the AME03 are presented in in figure 5.12. It can again be seen that the agreement is generally quite good except when using one measured and one extrapolated value to calculate a S_p value. There are two cases where the S_p from our measured values and those from the AME03 disagree, but these are again due to discrepancies between our measurements and the previously measured values. The $S_p(^{90}\text{Tc})$ disagreement is again found to be a result of the difference between our measured value of ^{90}Tc and the AME03 ground-state mass excess. The $S_p(^{88}\text{Mo})$ disagreement is due to a change in the measured ^{87}Nb value from that given in the AME03.

The deviation of the S_p values from the local trends when only one measured mass is available will have potentially important effects on astrophysical rate calculations. While the discussion of the variation in the $S_p(^{88}\text{Tc})$ value which will be presented in section 5.5.1 involves only measured masses, the size of the change in this S_p value is of the same order as the deviations caused by using one measured and one extrapolated mass. The resulting effect on the theoretical reaction rates is seen to be quite

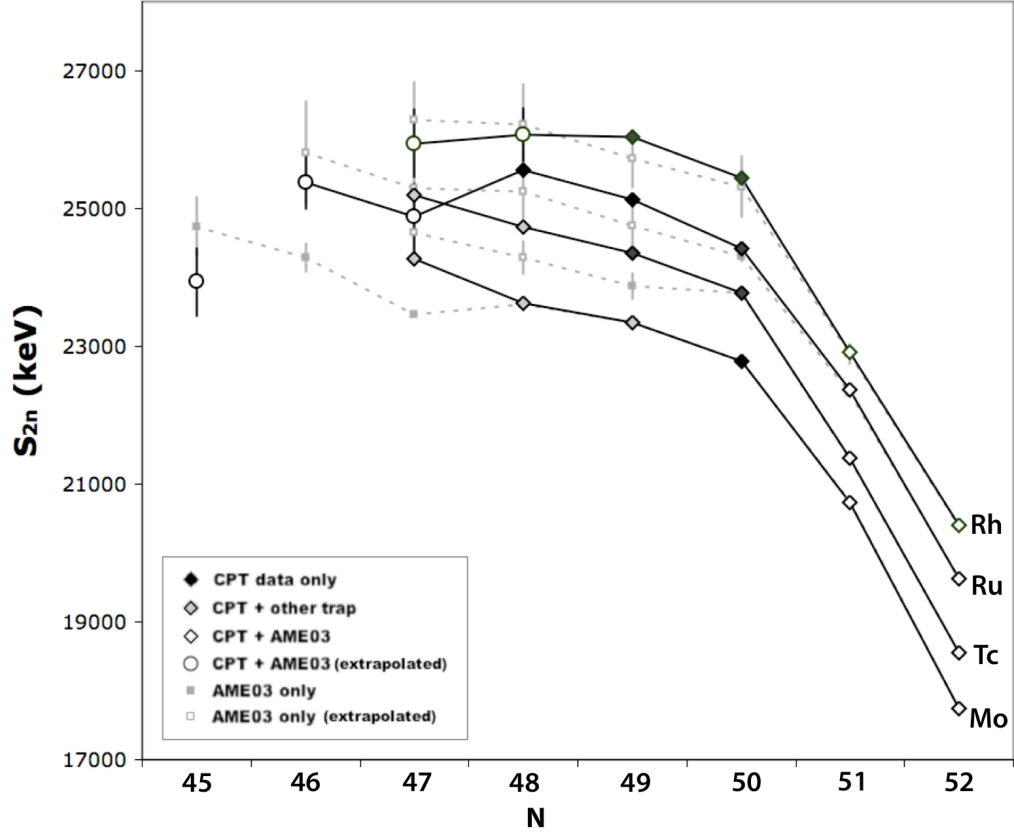


Figure 5.13: The S_{2n} values calculated from our mass measurements are presented here along with the AME03 S_{2n} values for comparison. Each point is derived from two mass values and the source of each of these values is identified in the legend. The other Penning trap values used are from [42, 59]. All the points shown have error bars, there are some cases however where the error bars are smaller than the data points.

significant.

There are much larger deviations between the extrapolated values from the AME03 and measured mass curves in the S_{2n} graphs than was seen in the S_{2p} graphs. This is due to the location of the $N=50$ shell closure and the fact that only the Mo curve and one measurement past the shell closure on the Tc curve were available to be used as a basis for the AME03 S_{2n} extrapolations for Ru and Rh. Once beyond the $N=50$ shell closure the S_{2n} values for Rh, Ru and Tc all deviate by more than 311 keV. The S_{2n}

values for Mo using our measurements follow the AME03 values quite closely even after encountering the shell closure as there had been more prior measurements beyond $N=50$ for this nuclide. This good agreement continues until ^{89}Mo where, due to the 803 keV change in the ^{87}Mo mass excess, the value of $S_{2n}(^{89}\text{Mo})$ deviates significantly from the AME03 value. The resulting curve is, however, found to match the trend of the curve from the recently measured Tc data quite well. Again we find that S_{2n} values calculated from one measured and one extrapolated value vary significantly from the trends. This is most obvious in the case of $^{88,89}\text{Ru}$ as the measured masses of $^{90,91}\text{Ru}$ are much heavier than the extrapolated mass values.

For all three of the separation energies discussed we see that further measurements or new extrapolations are required before single mass measurements can be used to calculate reliable separation energies involving a currently unmeasured mass.

5.4 Extrapolations

5.4.1 From systematic trends

In these extrapolations the neighboring slope resulting from values calculated from the recent measurements are used to estimate the location of the next S_{2p} , S_{2n} or $Q_{2\beta}$ value along the given curve (the Q_α systematics are not studied here as they are not smoothly varying in this region [21] and because, being roughly parallel to the p -dripline either both the required masses are measured or neither are). One example of the neighboring slopes used are given in each of the following 3 figures 5.14, 5.15 and 5.16, and the equations used are provided below:

$$S_{2n}(^A_Z X) = S_{2n}(^{A+1}_Z X) + |S_{2n}(^{A-1}_{Z-1} X) - S_{2n}(^A_{Z-1} X)| \quad (5.2)$$

$$S_{2p}(^A_Z X) = S_{2p}(^A_{Z-1} X) - |S_{2p}(^{A+1}_{Z+1} X) - S_{2p}(^A_{Z+1} X)| \quad (5.3)$$

$$Q_{2\beta}(^A_Z X) = Q_{2\beta}(^{A+1}_Z X) - |Q_{2\beta}(^A_{Z-1} X) - Q_{2\beta}(^{A+1}_{Z-1} X)| \quad (5.4)$$

The resulting extrapolated values are given in table 5.9.

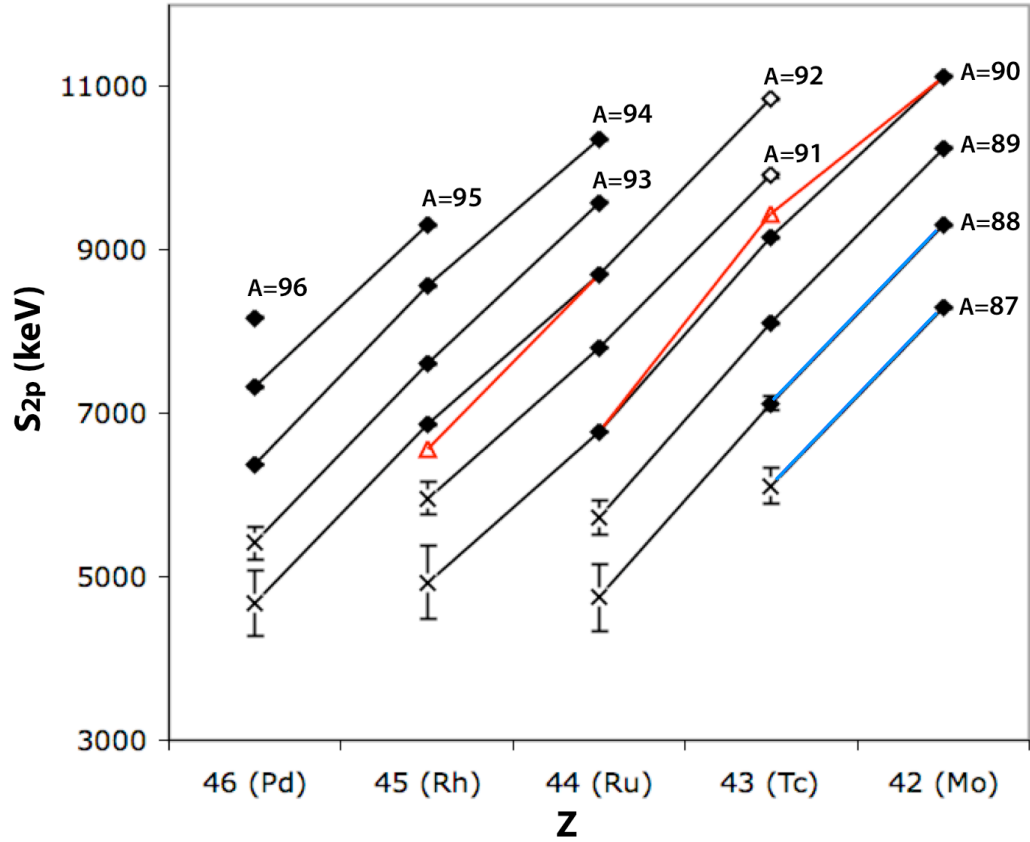


Figure 5.14: S_{2p} curves calculated from the weighted averages of the Penning trap measurements presented in table 4.4 when available. Otherwise the existing single Penning trap value is used (from table 4.4, [42] or [59]). Values which are a combination of one Penning trap measurement and one (non-extrapolated) AME03 value are represented by open diamonds. The extrapolated values are marked with an “x”. The red open triangles indicate the value which would result if our measurement of ^{90}Tc were a measurement of the isomeric state. The two line segments in blue (grey) indicate one example of the neighboring slopes used to determine the extrapolated values. Error bars are plotted but are generally smaller than the data point.

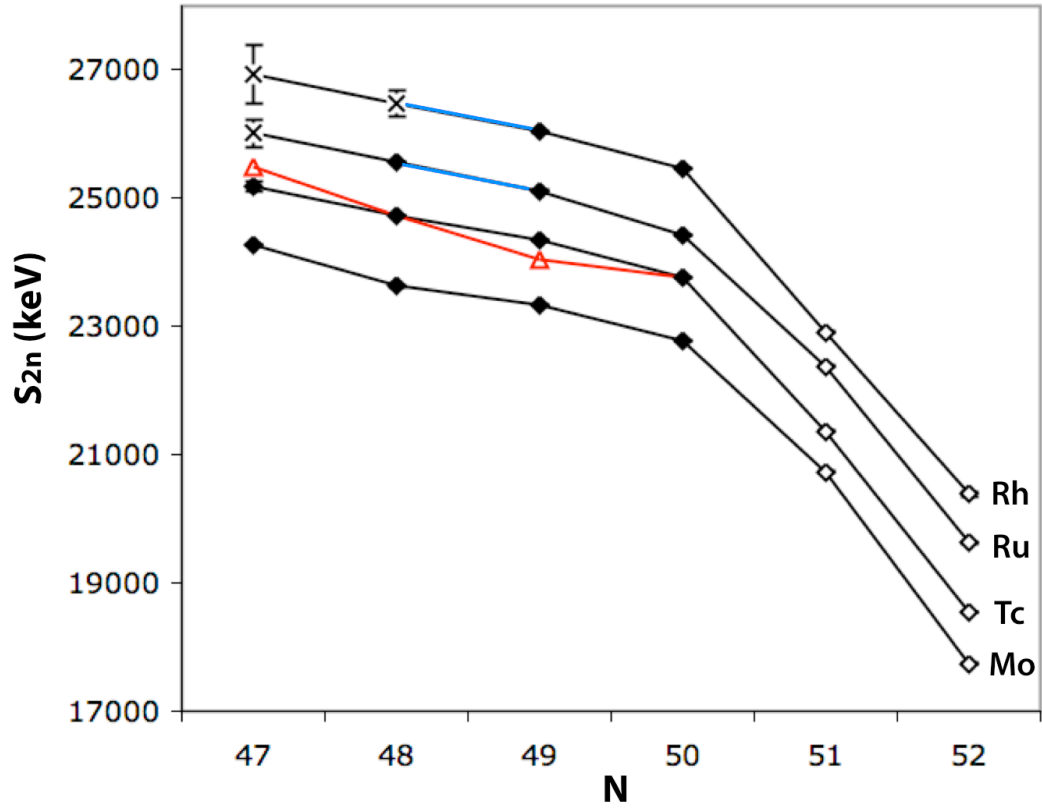


Figure 5.15: S_{2n} curves calculated from the weighted averages of the Penning trap measurements presented in table 4.4 when available. Otherwise the existing single Penning trap value is used (from table 4.4, [42] or [59]). Values which are a combination of one Penning trap measurement and one (non-extrapolated) AME03 value are represented by open diamonds. The extrapolated values are marked with an “x”. The red open triangles indicate the value which would result if our measurement of ^{90}Tc were a measurement of the isomeric state. The two line segments in blue (grey) indicate one example of the neighboring slopes used to determine the extrapolated values. Error bars are plotted but are generally smaller than the data point.

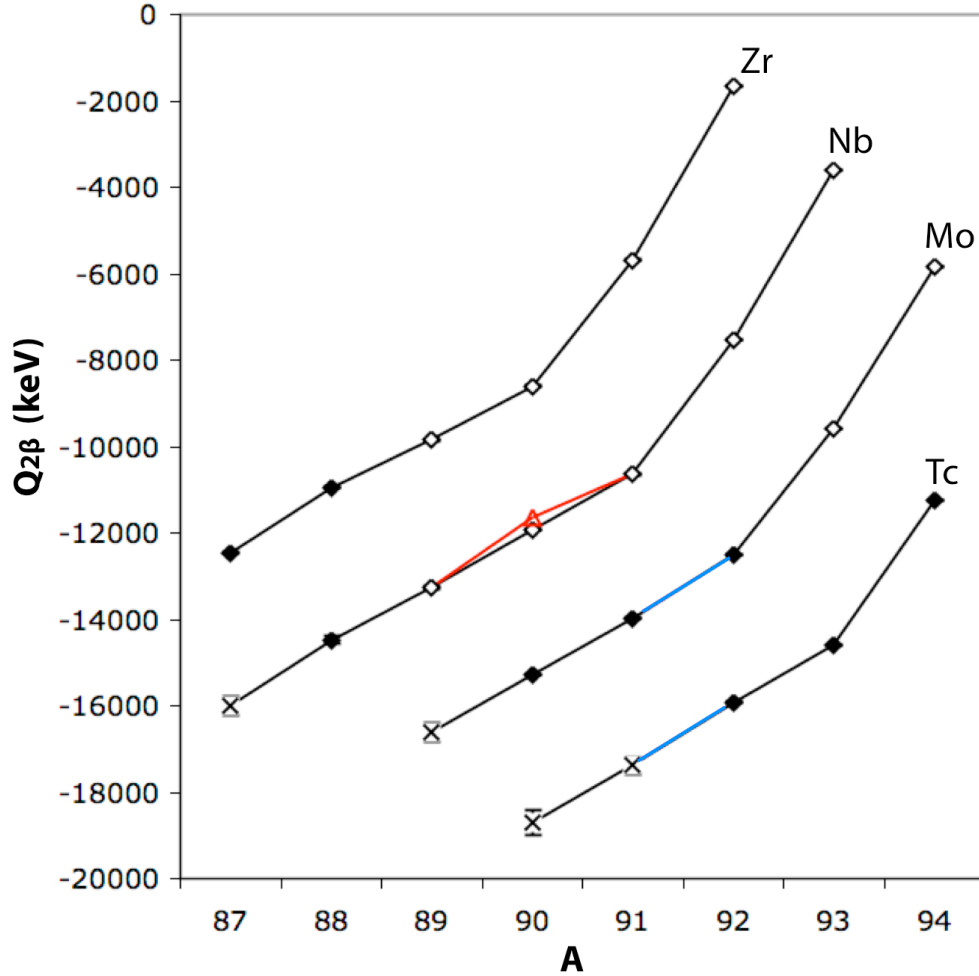


Figure 5.16: $Q_{2\beta}$ curves calculated from the weighted averages of the Penning trap measurements presented in table 4.4 when available. Otherwise the existing single Penning trap value is used (from table 4.4, [42] or [59]). Values which are a combination of one Penning trap measurement and one (non-extrapolated) AME03 value are represented by open diamonds. The extrapolated values are marked with an “x”. The red open triangles indicate the value which would result if our measurement of ^{90}Tc were a measurement of the isomeric state. The two line segments in blue (grey) indicate one example of the neighboring slopes used to determine the extrapolated values. Error bars are plotted but are generally smaller than the data point.

S_{2p} extrapolations (keV)		S_{2n} extrapolations (keV)		$Q_{2\beta}$ extrapolations (keV)	
^{87}Tc	6117(218)	^{91}Ru	26015(218)	^{87}Nb	-15987(218)
^{88}Ru	4750(409)	^{92}Rh	26936(456)	^{89}Mo	-16612(202)
^{89}Ru	5727(200)	^{93}Rh	26481(200)	^{90}Tc	-18699(283)
^{90}Rh	4931(447)			^{91}Tc	-17383(201)
^{91}Rh	5957(200)				
^{92}Pd	4676(400)				
^{93}Pd	5418(200)				

Table 5.9: The resulting extrapolated S_{2p} , S_{2n} and $Q_{2\beta}$ values in keV

The uncertainty which is provided is a combination of the uncertainty in all values used to determine the extrapolated value, plus an arbitrarily assigned uncertainty of 200 keV per step away from known values which was added to account for the uncertainty inherent in performing extrapolations. The AME03 assigns a 100 keV uncertainty in a similar way. I have chosen a larger value as I am looking at each of the systematic trends independently whereas the AME03 studies the variation of all curves simultaneously to determine their extrapolated value.

From these extrapolated separation and reaction energies we can calculate extrapolated values for the unmeasured masses. These are determined as follows:

$$M(N, Z)_{\text{extrapolated}} = M(N, Z - 2) + 2m_p - S_{2p} \quad (5.5)$$

$$M(N, Z)_{\text{extrapolated}} = M(N + 2, Z) - 2m_n + S_{2n} \quad (5.6)$$

$$M(N, Z)_{\text{extrapolated}} = M(N + 2, Z - 2) - Q_{2\beta}, \quad (5.7)$$

with m_p and m_n being the mass of the proton and neutron, respectively, which are given in table 4.3.

As S_{2p} values are differences along an isotone (nuclides with constant N), S_{2n} values are differences along an element (nuclides with constant Z), and $Q_{2\beta}$ are differences along an isobar (nuclides with constant A), sometimes all three values can be used to determine an extrapolated value for an unknown mass (figure 5.17). The resulting extrapolated masses are presented in table 5.10. The proton separation energy

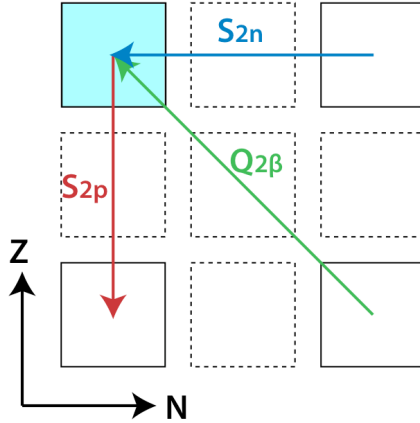


Figure 5.17: The direction of each of the separation or reaction energies used to perform the extrapolations on the chart of the nuclides is shown. This shows how all three separation energies can be used to determine certain extrapolated masses.

$S_p(^{90}\text{Rh})$ which can be calculated from these extrapolations will become important in our discussion of the rp process (section 5.5.2) and so the value determined from each set of curves is also included in table 5.10. For masses that have been determined from more than one extrapolated separation energy, both the uncertainties resulting from the separation energies as well as the standard deviations are provided.

As there is still uncertainty as to the ground and isomeric state assignment of our measurement of ^{90}Tc , and as this has an effect on the slopes used for some of our extrapolations, both our measured value and the calculated ground state (if our measurement is of the isomeric state) are included in the figures 5.14, 5.15 and 5.16. The resulting deviation of these points from the systematic trends in all 3 figures is the basis for the tentative assignment of our measurement of ^{90}Tc as a measurement of the ground state. If the excitation energy is found to be smaller, however, this argument will become less compelling.

If we were to use the calculated ground state of ^{90}Tc in extrapolations presented above we find that the masses of ^{90}Rh and ^{89}Ru would be different in all three cases. The values of ^{90}Rh and ^{89}Ru calculated from the S_{2p} curves would all be heavier by the ^{90}Tc excitation energy (297(240) keV), the values calculated from the S_{2n} curves would

Nuclide	Mass excess (keV)				σ_{std}
	From S_{2p}	From S_{2n}	From $Q_{2\beta}$	Average	
^{92}Pd	-54982(400)				
^{93}Pd	-59079(200)				
^{90}Rh	-52032(456)	-52216(456)	-52025(283)	-52091(235)	88
^{91}Rh	-58774(200)	-58674(200)	-58603(201)	-58684(116)	70
^{88}Ru	-54732(601)				
^{89}Ru	-58036(200)	-58366(218)	-58403(202)	-58268(119)	165
^{87}Tc	-57812(219)		-57883(219)	-57848(155)	36
$S_p(^{90}\text{Rh})$	1285(498)	1140(505)	910(340)	1112(262)	154

Table 5.10: Extrapolated mass excess values in keV resulting from the extrapolations of S_{2p} , S_{2n} and $Q_{2\beta}$. The average and standard deviation are given for the cases where more than one mass extrapolation is possible.

both be lighter by the ^{90}Tc excitation energy and the values calculated from the $Q_{2\beta}$ curves would be affected in opposite directions, with ^{90}Rh becoming lighter and ^{89}Ru becoming heavier. This would reduce the agreement between the extrapolated mass values which result from these calculations and which were presented in table 5.10. Looking at how the value of $S_p(^{90}\text{Rh})$ would be affected we find, however, that the values calculated from both the S_{2p} and S_{2n} extrapolations would not change as each of the two masses would vary by the same amount and so the difference between them would remain constant. This is an example of why the extrapolated mass differences are often more accurate than the masses themselves, and how our new mass measurements can deviate from the AME03 mass values by large amounts while our calculated S_p values still agree with the AME03 values.

5.4.2 Using the Garvey-Kelson relations

A slightly more rigorous method of calculating unknown masses from known ones is through the Garvey-Kelson relations [91, 92] (only the relation first presented in [91] is used here as it is best suited to the mass measurements available). These are derived using an independent-particle model of the nucleus and involve adding and subtracting the masses of nearby nuclides which would result in the same configuration

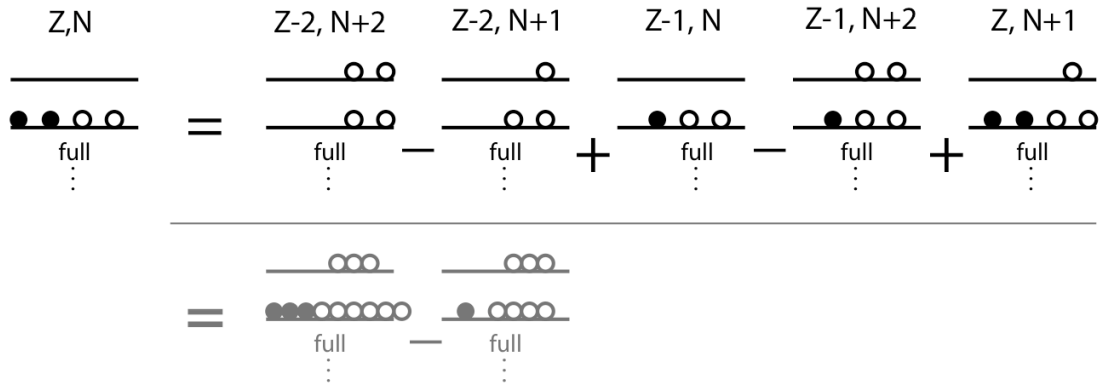


Figure 5.18: The single-particle levels which give rise to the Garvey-Kelson relation. This image is based on the example given in [91] for a case where $N=Z=2n$ where n is an integer. The closed circles represent protons and the open circles represent neutrons. The levels shown in grey do not represent actual nuclides, but are included to show how the two sides of the equation are equivalent.

of p and n levels as the nuclide of interest. This concept is illustrated in figure 5.18.

The resulting relation written in terms of the masses is as follows:

$$\begin{aligned}
 M(N, Z) = & M(N + 2, Z - 2) - M(N + 1, Z - 2) + M(N, Z - 1) \\
 & - M(N + 2, Z - 1) + M(N + 1, Z).
 \end{aligned}
 \tag{5.8}$$

This only holds if $N \geq Z$ and, if $N = Z$, if they are both even. This also relies on the assumption that the mass surface varies smoothly in the region where this relation is being used (our measured values extend far enough beyond the $N = 50$ shell closure that this is not a concern here). The location of these nuclides in relation to one another on the chart of the nuclides can be seen in figure 5.19.

As a calculation of an unknown $M(N, Z)$ relies on knowing (or at least having a previously calculated value for) 5 of its nearby neighbors (figure 5.19) this relation is most useful near existing measurements. The Garvey-Kelson relation can be used in an iterative fashion but, as more of the masses involved become masses previously calculated using this relation, the uncertainty grows accordingly. Here, three masses have been calculated directly from measured values and two more have

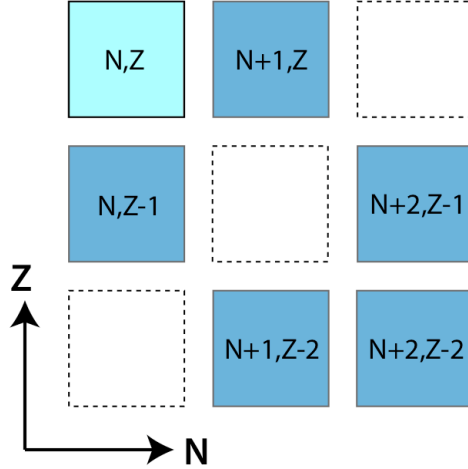


Figure 5.19: The location of the nuclides involved in the Garvey-Kelson relation. The light blue square indicates the relative location of the masses calculated in table 5.11.

Calculated using only measured values	
^{93}Pd	-59114(12) keV
^{91}Rh	-58852(12) keV
^{89}Ru	-58167(87) keV
Calculated using one of the masses above	
^{92}Pd	-55017(17) keV
^{90}Rh	-52111(88) keV

Table 5.11: Masses calculated using Garvey-Kelson relation. References for the measured masses are given in the text.

been calculated using one of the previously calculated masses. These values are presented in table 5.11. The masses used in these calculations were the weighted averages of the existing Penning trap (presented in table 4.4) whenever possible ($^{90,91}\text{Tc}$, $^{90-93}\text{Ru}$, $^{92-94}\text{Rh}$). Our measured values were used for $^{87,90}\text{Mo}$ and values from [42] were used for $^{88,89}\text{Mo}$, $^{88,89}\text{Tc}$ and $^{94,95}\text{Pd}$. These values are in agreement with the mass extrapolations performed using the systematic trends in all cases except ^{91}Rh , which is 1.4σ from the extrapolated uncertainty and 2.8σ from the standard deviation of the ^{91}Rh from the different systematic trends.

The value for $S_p(^{90}\text{Rh})$ which can be calculated from the masses in table 5.11 is

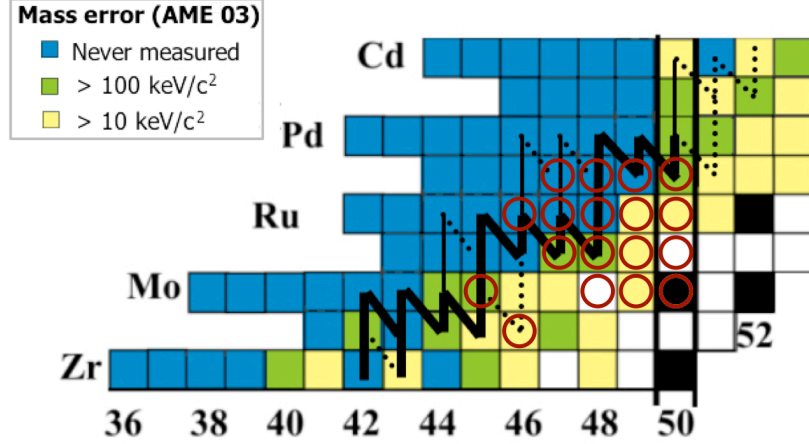


Figure 5.20: The location of our measurements and comparison to the νp process path [41]. The thinner and dotted lines indicate secondary and tertiary reaction paths, respectively. The colouration of the squares indicates the mass knowledge in this region as of the AME03 [21].

1232(124) keV. This value is also in agreement with that calculated from the mass extrapolations performed using the systematic trends.

5.5 Implications for Astrophysics

5.5.1 The νp process

The path of the νp process (or in fact any reaction process) is set by the balance of reaction rates which both create and destroy the various nuclides along that path. It was discussed in section 1.3.2 that the effective lifetime of a nucleus in the rp process was the sum of the lifetimes of the two possible paths: β decay and $2p$ -capture reactions. In terms of reaction rates this means that the effective rate of destruction of the nuclide in question ($\lambda_{\text{effective}}$) is the sum of the β -decay and $2p$ -capture rates (λ_{β} and λ_{2p} , respectively). In the νp process, with the addition of the n -capture reactions, the effective rate of destruction becomes:

$$\lambda_{\text{effective}} = \lambda_{(p,\gamma)} + \lambda_{(n,p)} + \lambda_{(\gamma,p)} + \lambda_{(n,\gamma)} + \lambda_{\beta}, \quad (5.9)$$

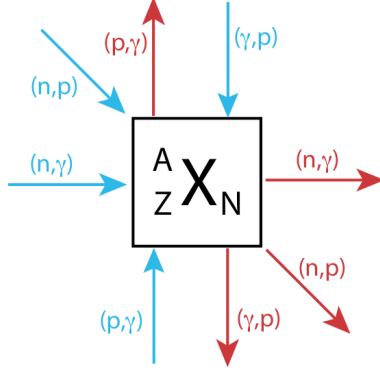


Figure 5.21: Potential reactions which can either create (blue / light grey) or destroy (red / dark grey) a nuclide in the νp process. β decay follows the same path as (n, p) reactions, but is not listed as it is generally negligible in this process.

though λ_β and $\lambda_{(n,\gamma)}$ are generally too slow to contribute significantly. These reaction rates (with the exception of the decay rate λ_β) depend on the temperature of the environment, the p or n abundances, the separation energies S_p or S_n , and on the nuclear level densities. The branching ratios of these reactions (the likelihood that a single nuclide will participate in any given reaction channel) is calculated by taking the rate of the reaction of interest λ_i over the sum of all rates which is $\lambda_{\text{effective}}$.

The rate of change of the abundance of any given nuclide along the process path is given as a differential equation which includes the rates of all of the reactions which create that nuclide (the added terms) and all of the reactions that destroy it (the subtracted terms).

$$\begin{aligned}
 \frac{d\mathcal{N}_{(N,Z)}}{dt} = & - \left(\lambda_{(N,Z)(p,\gamma)} + \lambda_{(N,Z)(n,p)} + \lambda_{(N,Z)(\gamma,p)} + \lambda_{(N,Z)(n,\gamma)} + \lambda_{(N,Z)(\beta)} \right) \times \mathcal{N}_{(N,Z)} \\
 & + \lambda_{(N,Z-1)(p,\gamma)}\mathcal{N}_{(N,Z-1)} + \lambda_{(N,Z+1)(\gamma,p)}\mathcal{N}_{(N,Z+1)} + \lambda_{(N-1,Z+1)(n,p)}\mathcal{N}_{(N-1,Z+1)} \\
 & + \lambda_{(N-1,Z)(n,\gamma)}\mathcal{N}_{(N-1,Z)} + \lambda_{(N-1,Z+1)(\beta)}\mathcal{N}_{(N-1,Z+1)}
 \end{aligned} \tag{5.10}$$

Modeling the νp process then involves constructing a network which can simultaneously solve all of the differential equations for all of the possible nuclides involved in this process. This calculation should also take into account how the various λ change as the temperature and possibly the p and n abundances vary over time.

It should be noted that the photo-disintegration rate ($\lambda_{(\gamma,p)}$) (the only reverse rate which needs to be taken into account in this process) can be calculated from its corresponding forward rate. If the two rates can be considered to be in equilibrium, the Saha equation applies and the reverse rate can be calculated from the forward rate as follows [5]:

$$\lambda_{(\gamma,p)} = \frac{(2\pi\mu kT)^{\frac{3}{2}}}{h^3} \frac{G_i}{G_f} e^{-S_p/kT} \lambda_{(p,\gamma)}, \quad (5.11)$$

where μ is the reduced mass of the parent nuclide and the incoming particle, k is the Boltzmann constant, h is the Planck constant, T is the temperature and G_i and G_f are the partition functions of the “initial” and “final” nuclides (the subscripts “ i ” and “ f ” are used to avoid confusion as “ p ” and “ d ” are typically used as particle identifiers).

As the changes in the proton separation energies determined from our measurements are not large enough to have a significant effect on the forward rates, the reaction rates for (p, γ) and the reverse rates (γ, p) have been calculated from the parametric equations given by Rauscher and Thielemann [93]. The reverse rate calculation requires that the S_p value be added explicitly and so the S_p values determined from our measurements were used when calculating the reverse rate (the partition functions used were those tabulated in [93]).

As discussed in section 1.3.3, the origin of production of the light p -nuclei, nuclei on the proton-rich side of the valley of stability which are not produced by the s or r processes, is largely unknown. There was particular interest in the νp process as it was found that this reaction process could potentially produce light p -nuclides, specifically ^{92}Mo and ^{94}Mo which are underproduced in all of the other nucleosynthesis processes. Fisker *et al.* [40, 41], investigated the details of the νp process models presented in Pruet *et al.* [39] and determined that the observed abundance ratio of ^{92}Mo with respect to ^{94}Mo could be almost completely set by the proton separation

energy of ^{93}Rh , $S_p(^{93}\text{Rh})$. This resulted from the fact that low S_p values for ^{92}Rh and ^{91}Rh meant that the vast majority of the reaction flow from ^{90}Ru and ^{91}Ru occurred through (n, p) reactions, creating ^{92}Ru , and not through (p, γ) reactions, which would create $^{92,93}\text{Pd}$. This resulted in 90% of the ^{92}Mo produced having ^{92}Ru as its precursor and $> 90\%$ of the ^{94}Mo produced having ^{94}Pd as its precursor (The Mo isotopes are produced when the reaction flow freezes-out and the nuclides along the νp -process path decay back towards stability).

There are two (p, γ) and two (γ, p) reactions linking ^{92}Ru to ^{94}Pd (fig. 5.22), but as $S_p(^{94}\text{Pd})$ is large, there is very little photo-disintegration of ^{94}Pd back into ^{93}Rh . As $S_p(^{93}\text{Rh})$ is relatively small photo-disintegration of this nuclide is much more likely. The competition between the rates of destruction of ^{93}Rh through the (p, γ) and (γ, p) reactions is what will set the relative abundances of ^{92}Ru and ^{94}Pd . The $S_p(^{93}\text{Rh})$ value is the primary factor in setting the νp -process $^{92}\text{Mo}/^{94}\text{Mo}$ abundance ratio.

Beginning with the assumption that the νp process is responsible for the observed $^{92}\text{Mo}/^{94}\text{Mo}$ abundance ratio of 1.57 and using current assumptions about the environment in which the νp process occurs (core collapse supernovae [38, 39]) Fisker *et al.* attempted to predict the unknown value of $S_p(^{93}\text{Rh})$ using their νp -process model [40]. There are, however, many uncertainties associated with several of the important parameters in supernovae models. The two main parameters which can affect this calculation are the entropy of the supernova explosion (which defines its temperature) and the electron fraction, Y_e (essentially a measure of the number of free protons). Fisker *et al.* [40, 41] found that for a 20% change in the entropy (which is much larger than the usual associated error) the calculated $S_p(^{93}\text{Rh})$ only changed by 50 keV. The predicted $S_p(^{93}\text{Rh})$ value was found to be most sensitive to the uncertainty in Y_e and so this uncertainty defines the uncertainty in their predicted S_p value [40].

In the supernova model used there are different regions of the early supernova wind with different parameters, these are called trajectories and are studied on a case by case basis. Pruet *et al.* [39] determined that of the 6 trajectories studied only

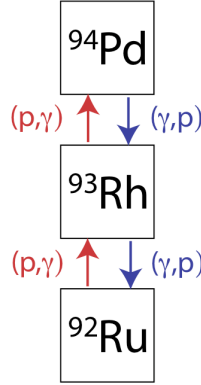


Figure 5.22: The reactions with determine the relative abundances of ^{92}Ru and ^{94}Pd in the νp process are the (p, γ) and (γ, p) reactions indicated in this figure.

one was found to synthesize any appreciable quantity of light p -nuclei [39]. Given the Y_e for this trajectory of 0.57, the $S_p(^{93}\text{Rh})$ which would be required for the νp process to reproduce the solar $^{92}\text{Mo}/^{94}\text{Mo}$ abundance ratio is 1.64 MeV [40, 41]. If the uncertainty in Y_e is $^{+0.03}_{-0.02}$, $S_p(^{93}\text{Rh})$ can be deduced with an uncertainty of 0.1 MeV [40, 41].

The $S_p(^{93}\text{Rh})$ value of 1.999 ± 0.006 MeV determined from our mass measurements is in agreement with the AME03 S_p value of 2.05 ± 0.50 MeV [21], but is well outside the range of the predicted value of $S_p(^{93}\text{Rh}) = 1.64 \pm 0.1$ MeV given by Fisker *et al.* [40, 41]. The lower S_p value from Fisker *et al.* [40, 41] would result in a suppression of flow from ^{93}Rh to ^{94}Pd due to the increased $^{93}\text{Rh}(\gamma, p)^{92}\text{Ru}$ rate. The measured $S_p(^{93}\text{Rh})$ is instead large enough that more ^{94}Pd than required for the solar abundance ratio is produced. Figure 5.23 shows a comparison of the $S_p(^{93}\text{Rh})$ values and includes the relationship between Y_e and $S_p(^{93}\text{Rh})$ needed to produce the solar $^{92}\text{Mo}/^{94}\text{Mo}$ abundance ratio [40]. The discrepancy between our measured $S_p(^{93}\text{Rh})$ value and that deduced by Fisker *et al.* implies that though the νp process is capable of producing ^{92}Mo and ^{94}Mo it does not produce them in the relative abundances needed to explain the observed solar $^{92}\text{Mo}/^{94}\text{Mo}$ abundance ratio of 1.57. The experimentally determined $S_p(^{93}\text{Rh})$ might still produce the solar abundance ratio of these

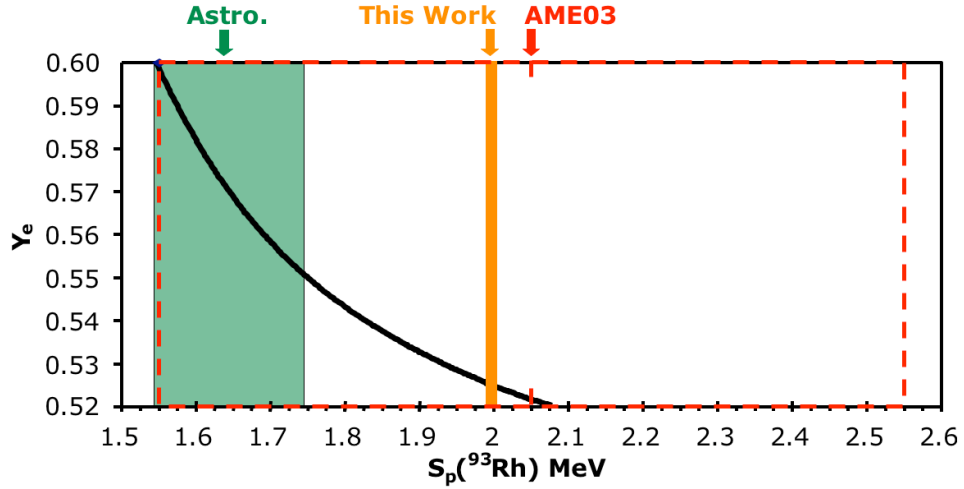


Figure 5.23: A comparison of the $S_p(^{93}\text{Rh})$ value from this work with the $S_p(^{93}\text{Rh})$ value given by the AME03 (enclosed by red dashed lines) [21], and the astrophysically predicted $S_p(^{93}\text{Rh})$ value [40, 41]. The curved black line indicates the relationship between Y_e and $S_p(^{93}\text{Rh})$ required to produce the solar $^{92}\text{Mo}/^{94}\text{Mo}$ abundance ratio. This relationship was used to determine the astrophysically predicted $S_p(^{93}\text{Rh})$, given that $0.55 \leq Y_e \leq 0.60$ [40, 41]

two nuclides if $Y_e \simeq 0.525$, however, none of the trajectories given by Pruet *et al.* [39] involve Y_e below 0.539. Furthermore, an environment with $Y_e \simeq 0.525$ is a much less proton-rich environment and this would have other consequences along the path of the νp process long before it arrives at the $^{92}\text{Ru}(p, \gamma)^{93}\text{Rh}$ reaction. Unless there are some as yet unexpected or unexplored details which affect the conditions in the inner core-collapse ejecta of supernovae or new revelations with regards to the nuclear data in this region, it seems that there must be yet another process or astrophysical site involved in the production of ^{92}Mo and ^{94}Mo .

Looking once again at the νp process path as a whole, there are many reactions where similar changes in S_p values could affect the production rates and potentially the path of the νp process. Weber *et al.* [42] recalculated the forward and reverse rates which were affected by their mass measurements. As so many of the S_p values from

the recently measured masses in this region agreed so closely with the AME03 [21] the recalculated rates and resulting νp -process abundances were also not found to be significantly different [42]. The exceptions to this were the abundances of $^{87,88}\text{Sr}$, ^{89}Y , $^{90,91}\text{Zr}$ [42]. The change in these abundances was determined to be primarily due to a large change in the $S_p(^{88}\text{Tc})$ value reported by Weber *et al* [42] which resulted from their measurement of ^{88}Tc (their measured value for ^{88}Tc was found to be 1031(218) keV heavier than the extrapolated AME03 value [42]). This in turn led to an increased rate for $^{88}\text{Tc}(\gamma, p)^{87}\text{Mo}$ as compared to that calculated from the AME03 values [42]. Their value for $S_p(^{88}\text{Tc})$, however, used their measured ^{88}Tc value and the AME03 value of ^{87}Mo [42]. We have since measured the mass of ^{87}Mo and found it to be significantly different from the AME03 value [21].

Our mass measurement of ^{87}Mo results in a change in the $S_p(^{88}\text{Tc})$ value due to the 803(220) keV difference between our measured value and the AME03 value. This shift in ^{87}Mo compensates in part for the 1031(218) keV shift in the value of ^{88}Tc measured by Weber *et al.* [42] and brings the $S_p(^{88}\text{Tc})$ value back towards the original value from the AME03 [21] (though it remains 230 keV lower). This change will again affect the calculated $^{88}\text{Tc}(\gamma, p)^{87}\text{Mo}$ rate. We find that, though there will still be a suppression of flow through $^{87}\text{Mo}(p, \gamma)^{88}\text{Tc}$ as compared to the AME03 case, the suppression is nowhere near as large as that presented by Weber *et al.* [42]. Using the rate equations provided by Rauscher and Thielemann [93] and changing only the reaction Q_p value (the S_p value of the daughter nuclide from the forward reaction), the photo-disintegration rate calculated using our measured ^{87}Mo mass and the mass of ^{88}Tc from Weber *et al.* [42] is only 1.63 times that calculated using the AME03 values. The photo-disintegration rate calculated from the ^{88}Tc mass from Weber *et al.* and the AME03 value of ^{87}Mo [21] is 343 times the rate calculated from the AME03 values. The forward rates have not been recalculated here as the change of only 170 keV from the FRDM based $S_p(^{88}\text{Tc})$ of 1901 keV [94] used by Rauscher and Thielemann [93] in the calculation of their forward rates would not result in a

Nuclide	Reaction	λ (s ⁻¹)	Branching ratio (B.R.)		
⁸⁷ Mo	γ, p	1.42×10^{-2}	–		
	p, γ	7.93×10^3	99.5%		
	n, p	3.82×10^1	0.48%		
	n, γ	1.35×10^0	0.02%		
Nuclide	Reaction	λ (s ⁻¹)	B.R. _{Traps}	B.R. _{Weber}	B.R. _{AME}
⁸⁸ Tc	γ, p (Traps)	2.31×10^5	3.7×10^{-6} %		
	γ, p (Weber)	4.84×10^7	0.0008%		
	γ, p (AME)	1.41×10^5	2.3×10^{-6} %		
	p, γ	6.08×10^{12}	~100%	99.9992%	~100%
	n, p	4.98×10^1	–	–	–
	n, γ	–	–	–	–

Table 5.12: Shown are the calculated rates, λ , for the various destructive reactions for ⁸⁷Mo and ⁸⁸Tc as well as the corresponding branching ratio. Rates were calculated using reference [93] and parameters from Pruet *et al.* [39] ($T_9 = 2.05$, $\rho = 2.74 \times 10^4$, $Y_p = 0.122$, $Y_n = 1.00 \times 10^{-12}$). The S_p value used for the (γ, p) reaction for ⁸⁷Mo is one of the three cases discussed in the text and are labeled as follows: (Traps) indicating the use of both Penning trap measurements, (Weber) the S_p value presented in Weber *et al.* [42], and (AME) indicating the use of AME03 values [21] for both nuclides.

significantly different result. It is the exponential dependence of the reverse rates on the S_p value that causes even a small change in the S_p value to have a potentially large effect on the photo-disintegration rate.

Given the large change in the mass excess of ⁸⁷Mo and given a new Penning trap measurement of ⁸⁶Nb since the AME03 [59], we have also recalculated the S_p value of ⁸⁷Mo and studied how it affects the rate of ⁸⁷Mo(γ, p)⁸⁶Nb. Though the measured value for S_p (⁸⁷Mo) is found to be ~100 keV lighter than the S_p (⁸⁷Mo) value determined from the AME03, the ⁸⁷Mo(p, γ)⁸⁶Nb reaction rate is not affected as this S_p value is still too large for photo-disintegration to occur at any significant rate given the temperatures involved in the νp process ($T_9 = 2.05$).

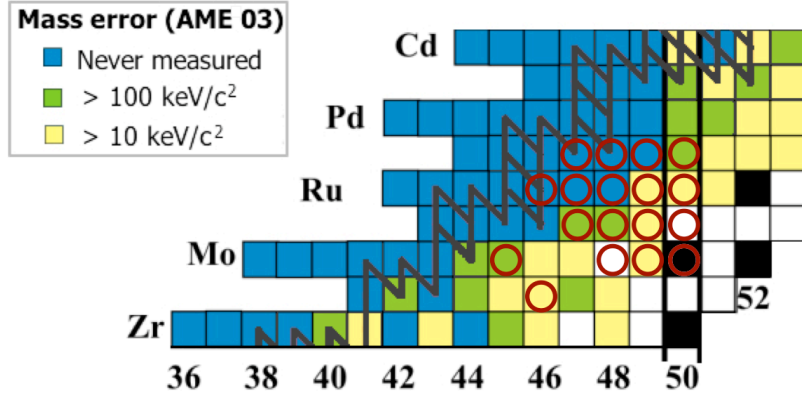


Figure 5.24: The location of our measurements and comparison to the rp process path [25]. The colouration of the squares indicates the mass knowledge in this region as of the AME03 [21].

5.5.2 The rp process

We have already seen from the discussion in sections 5.3 and 5.5.1 that separation energies calculated from a measured value and an extrapolated AME03 value result in large deviations from the systematic trends and should be avoided until new measurements or, at very least, new extrapolated values become available. This unfortunately limits the applicability of our measurements to the rp -process as only a few nuclides along the expected rp -process path in this region have been measured [25] (fig. 5.24). These measurements will, however, inevitably improve the extrapolated values which will come from the next edition of the AME as the general uncertainty for their extrapolated values increases by 100 keV for every step away from the measured values and our measurements as well as those by Weber *et al.* [42] now extend 2-3 isotopes beyond the measurements in the AME03. This should permit extrapolated precisions to the $N = Z$ line of ~ 200 keV as opposed to the values in the AME03 where the uncertainties are 300-450 keV. This will bring the extrapolated uncertainties closer to the precisions of < 100 keV required for accurate modeling of the rp -process, though further measurements in the region are most certainly desired. With the hope of being able to provide at least some insight into the rp process using our measurements

a few mass extrapolations were performed in section 5.4.

A recent paper by Parikh *et al.* [95] looked at the effect of individually varying all of the Q_p values along the rp -process path which were below 1 MeV (this value was chosen as, at the rp -process temperatures, these Q_p are the most likely to create waiting points along the rp -process). This study was undertaken in an effort to determine which reactions have the potential to most significantly affect the rp -process models and indicate where future measurements should be focused. Parikh *et al.* [95] find that even with the recent measurements presented here and elsewhere [42, 59] the masses of the most interest still have yet to be measured.

In the region between Nb and Pd the reaction which has the largest effect on the rp -process is $^{89}\text{Ru}(p, \gamma)^{90}\text{Rh}$. It was noted that, for all cases studied, variations of 20% of the current Q_p uncertainty were too small to create substantial differences in the resulting abundances [95]. In the case of $^{89}\text{Ru}(p, \gamma)^{90}\text{Rh}$, however, the Q_p value needed to be increased by more than 50% of the current uncertainty before it significantly affected the rp -process abundances which were calculated [96]. This means that the Q_p value for this reaction would need to be at least 356 keV higher than that currently given by the AME03 [21]. With a $S_p(^{90}\text{Rh})$ value calculated using a Garvey-Kelson relation of 1232(124) keV which is only 240 keV from the extrapolated AME03 value of 990(710) keV, and with all three of the $S_p(^{90}\text{Rh})$ values determined from our extrapolations within 268 keV of the AME03 value (table 5.10), the rp -process abundances are not expected to change as a result of our measurements of masses in the vicinity of ^{89}Ru and ^{90}Rh .

Other masses in this region which are also considered to be of particular interest which remain future goals are ^{84}Nb , ^{85}Mo , ^{86}Tc , ^{87}Tc and ^{96}Ag [95].

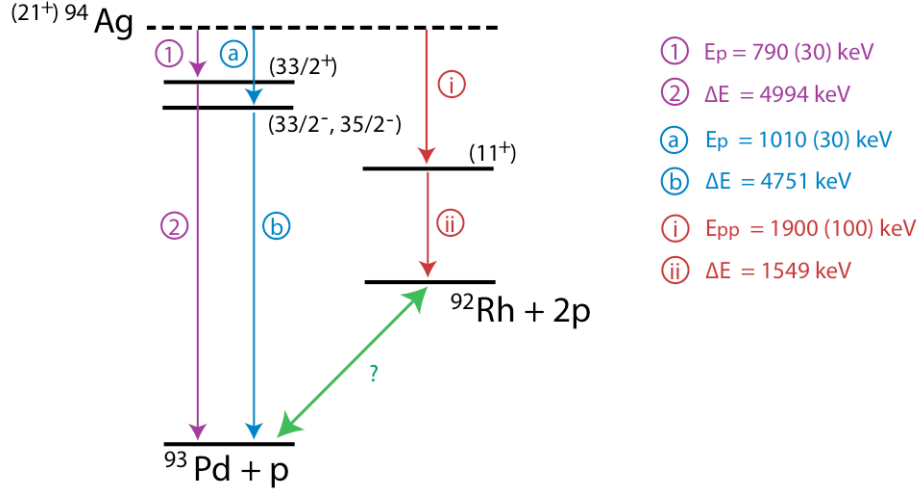


Figure 5.25: The p and pp decay energies from the (21^+) state of ^{94}Ag , the states into which they are believed to decay and that excitation energies of those states are shown in the figure. The sources for the p , pp and excitation energies are: ①, ②, (a) and (b) [98], (i) [97], and (ii) [85].

5.6 Implications of the ^{92}Rh mass for the pp decay of ^{94}Ag

The mass of ^{92}Rh has become the subject of increased interest recently due to the potential pp decay of a state in ^{94}Ag reported in Nature in 2006 by Mukha *et al.* [97]. To confirm that this decay is possible we need to have a measurement of the ground-state mass excesses of the parent and daughter nuclides of this decay, ^{94}Ag and ^{92}Rh , as well as a solid understanding of the level structures of these two nuclides. As producing ^{94}Ag in large enough quantities for mass measurements is difficult, other possible measurements have been considered. Mass measurements of ^{92}Rh and ^{93}Pd could also provide a confirmation as the (21^+) state in ^{94}Ag , which is the one thought to undergo pp decay to ^{92}Rh , also decays to ^{93}Pd via p decay.

$$^{94}(J=21^+)\text{Ag} \rightarrow ^{92}\text{Rh} + 2p + E_{pp} \quad (5.12)$$

$$^{94}(J=21^+)\text{Ag} \rightarrow ^{93}\text{Pd} + p + E_p \quad (5.13)$$

As we know the p and pp energies (E_p and E_{pp}) from the (21^+) state in ^{94}Ag as well

as the excitation energies of the states into which the (21^+) state is expected to decay, with a measurement of the ^{92}Rh mass excess we can determine the ground state of ^{93}Pd expected if the pp -decay does indeed proceed spontaneously (figure 5.25). The mass excess of ^{93}Pd which is calculated from these data is $-58044(100)$ keV. This is $1660(410)$ keV heavier than the extrapolated AME03 mass excess of $-59700(400)$ keV [21].

While our mass measurements have all tended to be heavier than the extrapolated AME03 values (table 4.4) we have not seen any change as large as would be required to explain the difference between the AME03 extrapolation and the ^{93}Pd mass excess calculate from the p and pp -decay of ^{94}Ag . Among our measurements, the largest difference between a measured and extrapolated value was for ^{90}Ru and was $423(300)$ keV, only a quarter of the difference required to explain the discrepancy between the calculated ^{93}Pd value and the AME03.

Kankainen *et al.* [60] use the mass measurements presented by Weber *et al.* [42] to calculate a mass excess for ^{94}Ag via Coulomb displacement from ^{94}Pd . This estimate is then used, in combination with other measured values along the $N=47$ isotone [60, 42], to interpolate a mass excess for ^{93}Pd . The mass excess they report for ^{93}Pd is $59440(160)$ keV [60] which is in agreement with the extrapolated AME03 value and far lighter than the ^{93}Pd mass excess which results from the p and pp decay energies calculated above.

Our value of ^{93}Pd , calculated using a Garvey-Kelson relation (section 5.4.2), of $-59114(12)$ keV does not agree with either the extrapolated AME03 value [21] or that calculated by Kankainen *et al.* [60]. While it results in a heavier mass than either of these two estimated values it, too, remains lighter than the ^{93}Pd mass excess resulting from the p and pp decay energies.

Until there is a measurement of ^{93}Pd or ^{94}Ag , however, there remains no way of conclusively determining whether or not this decay is possible from our measurement of ^{92}Rh .

Chapter 6

Conclusions and Outlook

6.1 Conclusions

Since the first CPT experiments performed to measure masses of proton-rich nuclides in the region between Nb and Pd there have been many upgrades to the CPT system. The combined effect of the greater collection efficiency from the $3^\circ - 12^\circ$ acceptance beam-line (section 3.1.1) and associated high-intensity gas catcher (section 3.1.2), the improved mass selection through the addition of the 2nd generation isobar separator (section 3.2.1), and the improved cleaning in the precision Penning trap through the use of an arbitrary waveform generator (section 3.3.2), have all contributed to a steady progression in the measurements to nuclides increasingly further from stability (fig. 6.1 and table 4.1).

In this work we have reported the results of 18 mass measurements of proton-rich nuclides on or near the νp - and rp -process paths in a region where, until recently, very few experimental mass determinations had existed. We presented the first two mass measurements of ^{92}Ru and ^{93}Rh [18], which were confirmed by Weber *et al.* [42]. We confirm 11 of the other Penning trap mass measurements performed with JYFLTRAP and SHIPTRAP performed during the same time period [42, 59] and present the first direct mass measurements of 4 other nuclides. Our measurement of ^{92}Mo confirms the existing direct mass measurements [20].

The most significant of these 4 new direct mass measurements is the measure-

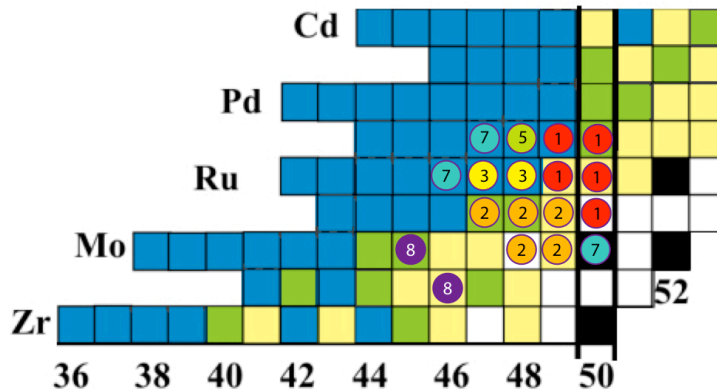


Figure 6.1: Shown above are all nuclides presented in this thesis, colour coded by which experiment was the first to measure them. Experiment 1 is indicated by red circles, experiment 2 by orange circles and so on through the spectrum (experiments 4 and 6 are not indicated as they simply improved the precision of previously measured masses). The colours of the squares indicate the mass knowledge as of the AME03 [20, 21] and their explanation can be found most recently in figures 5.20 and 5.24.

ment of ^{87}Mo which was found to be 803 keV heavier than the AME03 value. This measurement moves $S_p(^{88}\text{Tc})$ closer to the AME03 value than was reported by Weber *et al.* [42], though at 2081(87) keV it remains ~ 230 keV lower. This change in the $S_p(^{88}\text{Tc})$ value results in lowering the photo-disintegration rate of ^{88}Tc back towards the AME03 value. We find that the current rate predicted by mass measurements is only 1.63 times stronger than the rate calculated using the AME03 values, as opposed to a rate 343 times stronger as was found by Weber *et al.* [42].

6.2 Outlook

When not measuring masses online, the CPT system has been contributing to measurements of masses on the neutron-rich side of the valley of stability. The source of these n -rich nuclides is a ^{252}Cf fission source which is currently located in the gas volume of the high-intensity gas catcher. This has been an ongoing program with 26 masses having been published in 2006 [12] and over 20 more [15] having been

measured in the last 2 years.

The success of this gas catcher technology for producing low emittance beams of these ^{252}Cf fission fragments has led to a proposed upgrade of the ATLAS facility which will allow for fission fragments from a much larger ^{252}Cf fission source (up to 1 Ci) to be used as an ion source for the ATLAS accelerator. This Californium Rare Ion Beam Upgrade (CARIBU) is currently under construction. While the CARIBU gas catcher and the accompanying mass separator are being installed, the CPT tower, containing the precision Penning trap and the linear RFQ accumulation trap, will be installed online downstream from the CARIBU ion source. The CPT system will be used to help with the commissioning of the CARIBU system prior to its connection to the accelerator. The expected increase in the production of the fission fragments due to the source strength alone is 7000 fold and this will provide the opportunity to measure another 2-4 isotopes outwards from stability than is currently possible.

While the CPT mass spectrometer is coupled to the CARIBU system it will not be possible to measure ions created through online fusion-evaporation reactions. The rest of the CPT system will remain in use as part of an ongoing program to measure the $\beta - \nu$ correlation in the decay of ^8Li . This measurement will be conducted in the open geometry RFQ trap (named the Beta Paul Trap or BPT) which is located downstream from the second generation isobar separator.

It is expected that, once installed, the CPT mass spectrometer will remain at its new location near the CARIBU system for approximately 2 years before being moved back to its original location. The direction of our future measurements will be selected at that time based on the status of mass measurements completed at other facilities in the interim, and which physics questions will be the driving motivation for future online mass measurements.

Appendix A

Laplace's equations and the trapping potentials

The following discussion of how Laplace's equations give rise to the trapping potentials provided in chapter 2 is also laid out very nicely in *Quadrupole Mass Spectrometry and its Applications* [45]. Much of what follows is derived (at least in part) from that source.

There is a theorem by Earnshaw which states “A charged particle cannot be held in a stable equilibrium by electrostatic forces alone” [99]. This results from Laplace's equations which require that $\nabla \cdot \mathbf{E} = 0$. This implies that there can be no maxima or minima of the field in free space, and thus no possibility for stable confinement. There remains however the possibility of saddle points which result unstable equilibrium conditions. These unstable equilibrium conditions are exploited to create the confinement in ion traps. In linear RFQ traps the confinement comes from the alternating electric potentials used. In Penning traps this arises from the additional force of the ion motion in the added magnetic field.

The equation for the quadrupole electric field on which all ion traps are based can be expressed most generally in the form:

$$\mathbf{E} = E_o(\lambda\mathbf{x} + \sigma\mathbf{y} + \gamma\mathbf{z}), \tag{A.1}$$

where λ , σ and γ are weighting constants and E_o is the field strength. As the effect of the field on the ion is independent in all directions the force acting on the ion increases as it is displaced in any direction from zero. The requirement from Laplace's Equations ($\nabla \cdot \mathbf{E} = 0$) gives rise to the constraint

$$\lambda + \sigma + \gamma = 0. \quad (\text{A.2})$$

The potential arising from the electric field given in [A.1](#) is

$$\Phi = \frac{1}{2}\Phi_o(\lambda x^2 + \sigma y^2 + \gamma z^2), \quad (\text{A.3})$$

and is subject to the same constraints (equation [A.2](#)).

The solutions for equation [A.2](#) depend on the desired function and geometry of the ion trap (with the trivial solution of $\lambda = \sigma = \gamma = 0$ being ignored as there is no field to consider in this case).

A.0.1 2D confinement

A linear radiofrequency quadrupole (RFQ) trap (the type of RFQ trap which is used in the CPT system) is a 2D device. The requirement that the quadrupole field only exist in two dimensions means that one of the weighting constants in equations [A.1](#) and [A.3](#) must be zero. By definition we chose $\gamma = 0$. This leaves

$$\lambda = -\sigma, \quad (\text{A.4})$$

which results in an electric potential of the form

$$\Phi = \frac{1}{2}\Phi_o\lambda(x^2 - y^2). \quad (\text{A.5})$$

Given a distance of r_o between the rods which are used to establish this potential, we have

$$\lambda = -\frac{1}{r_o^2}, \quad (\text{A.6})$$

which in turn results in the potential that is presented in section [2.2.1](#),

$$\Phi = \frac{\Phi_o}{2r_o}(x^2 - y^2). \quad (\text{A.7})$$

A.0.2 3D confinement

To create a 3D ion trap all of the weighting constants in equation A.1 and A.3 are required to be non-zero. The simplest solution to the constraints of equation A.2 in this case is

$$\lambda = \sigma, \quad \gamma = -2\sigma, \quad (\text{A.8})$$

which gives rise to the potential

$$\Phi = \frac{1}{2}\Phi_o\lambda(x^2 + y^2 - z^2). \quad (\text{A.9})$$

The equipotential lines here are similar to the 2D case, but rotationally symmetric about the \mathbf{z} axis. Again with $\lambda = -1/r_o^2$ we find

$$\Phi = \frac{\Phi_o}{2r_o^2}(r^2 - z^2). \quad (\text{A.10})$$

This defines the stationary electric potential in the Penning trap. This equation is not exactly as presented in section 2.1.1 (equation 2.2) but the difference only involves the inclusion of the geometric factor d as defined by equation 2.3.

Appendix B

Error propagation

Presented here is a summary of all error calculations relevant to the data presented in this thesis, in the order that they are used from the acquisition of data through to the final values. For more information on these equations and how they arise see [100]. Also, note that the terms “error” and “uncertainty” are often used interchangeably. “Uncertainty” is the preferred term for these values as they are limits in our ability to determine the precise value and not errors. In much of the standard terminology, however, the word “error” is still commonly used.

Each of our data points at each applied frequency is a collection of ion arrival times. The mean of these arrival times is plotted as the data point associated with that particular applied frequency. The error bar associated with this data point is the error in the mean and is calculated as follows:

$$\Delta\text{TOF}_{Mean} = \frac{\sigma}{\sqrt{N}}, \quad (\text{B.1})$$

where

$$\sigma \simeq \sqrt{\frac{1}{N-1} \sum (\text{TOF}_i - \text{TOF}_{Mean})^2}. \quad (\text{B.2})$$

These data points and their uncertainties are plotted versus their associated frequency, and the spectrum which is generated is fit by one of the fitting functions presented in section 3.4.3. The best fit of the function is determined through a “least squares fit” method where a measure of the goodness of fit is given by a parameter

known as the reduced χ squared (χ_R^2). This is a function of the residual (r), which is the difference between each point and the expected value which arises from the fit:

$$r_i = \text{TOF}_{Mean,i} - \text{TOF}_{fit,i}, \quad (\text{B.3})$$

weighted by the uncertainty associated with the data point given by

$$w_i = 1/\Delta\text{TOF}_{Mean,i}, \quad (\text{B.4})$$

and which is then reduced by the number of degrees of freedom which are used in the fitting function (n). The result is

$$\chi_R^2 = \frac{1}{N-n} \left(\sum r_i^2 w_i^2 \right). \quad (\text{B.5})$$

Fitting the function involves minimizing this χ_R^2 which, mathematically, involves fitting the parameters such that, for a function $\bar{y} = f(x_i)$:

$$\frac{\partial \chi_R^2}{\partial \bar{y}} = \frac{1}{N-n} \sum -2(y_i - \bar{y})w_i^2 = 0. \quad (\text{B.6})$$

For complicated functions computer algorithms are used. The CPT fitting program uses the Marquardt method. For more information see [100].

The value determined for the parameter of the fitting function (equation 3.11 or 3.13) which defines the location of center of the TOF dip is the value for ω_c and its associated error is $\Delta\omega_c$

Typically $\chi_R^2 \simeq 1$. In cases where $\chi_R^2 > 1$ this means that the error bars associated with the data points are smaller than the differences of the fit from the data, and so the value found for $\Delta\omega_c$ may underrepresent the error. In these cases $\Delta\omega_c$ is “inflated” by multiplying it by χ_R resulting in a value $\Delta\omega_c^{infl}$. This inflated error will be taken as the uncertainty for this particular measurement. In contrast when $\chi_R^2 < 1$ this indicates that the error of the data points is larger than the scatter of the points about the line of the fit. Following the same logic as above it might seem that we should reduce the value of $\Delta\omega_c$ in these cases. As it is generally better to

have overestimated an uncertainty than to have underestimated it no reduction of the error is performed. The uncertainty in the measured ω_c is then the maximum of $\Delta\omega_c$ and $\Delta\omega_c^{infl.}$, which I will denote by $\Delta\omega_c^{(infl.)}$

For each experiment then, we have a list of ω_c values for each ion measured. To arrive at a single value for ω_c we take a weighted average of the measurements. This ensures that more precise measurements contribute more strongly to the value of the resulting average. The weight of each measurement of ω_c is set by the size of its associated uncertainty just like in equation B.4

$$w_i = 1/\Delta\omega_{c,i}^{(infl.)}. \quad (\text{B.7})$$

The weighted average is given by

$$\omega_c^{w.a.} = \frac{\sum \omega_{c,i} w_i^2}{\sum w_i^2}. \quad (\text{B.8})$$

The uncertainty which is calculated from the combination of $\Delta\omega_{c,i}^{(infl.)}$ values is known as the internal uncertainty σ_{int} and is given by

$$\sigma_{int} = \sqrt{\frac{1}{\sum w_i^2}}. \quad (\text{B.9})$$

This error, however, does not take into account the scatter in the data points, which could potentially be larger than would be expected from the uncertainties alone. As a test of this we calculate the external uncertainty in a similar way to determining the deviation of the data from the fit in the case of the “least squares fit”. We do this by looking at the weighted residual (the residual was given in equation B.3). The external uncertainty is given by

$$\sigma_{ext} = \sqrt{\frac{1}{N-1} \frac{\sum r_i^2 w_i^2}{\sum w_i^2}}. \quad (\text{B.10})$$

To determine how well the error in each measurement represents the scatter in the data points, we compare the internal and external errors. If the uncertainty in the

points represents the scatter well we should find these two errors to be approximately equal, or, in other words, that the ratio of the errors be close to 1:

$$\left(\frac{\sigma_{ext}}{\sigma_{int}}\right)^2 = \frac{1}{N-1} \sum -2(\omega_{c,i} - \omega_c^{w.a.})w_i^2 \approx 1, \quad (\text{B.11})$$

which is the same form as the equation for χ_R^2 as for a weighted average $n = 1$. Similarly to the case for ω_c if we find that $\chi_R^2 > 1$ we need to inflate the resulting uncertainty by χ_R . From equations B.9 and B.11 however we find that the inflated value of σ_{int} is simply σ_{ext} . The error in the weighted average, $\Delta\omega_c^{w.a.}$ is then the larger of σ_{int} and σ_{ext} .

Finding the uncertainty of the resulting frequency ratio, R (the ratio of the $\omega_c^{w.a.}$ values of the ion of interest and the calibrant ion) is simply a matter of summing the fractional errors in quadrature:

$$\Delta\left(\frac{\omega_{c,1}}{\omega_{c,2}}\right) = \sqrt{\left(\frac{\Delta\omega_{c,1}}{\omega_{c,1}}\right)^2 + \left(\frac{\Delta\omega_{c,2}}{\omega_{c,2}}\right)^2}. \quad (\text{B.12})$$

Finding the uncertainty in the mass which is calculated from this frequency ratio requires correctly combining the error in R as well as the current uncertainty in the mass of the calibrant ion and the mass of the electron. This can be done through either the combined use of the equations for error propagation for products/quotients (given above) and error propagation for sums/differences (summing in quadrature the absolute errors). Or, as is generally done for non-linear functions (say $f(a, b, c, \dots)$), the error can be found as:

$$\sigma_f^2 = \left(\frac{\partial f}{\partial a}\right)^2 \sigma_a + \left(\frac{\partial f}{\partial b}\right)^2 \sigma_b + \left(\frac{\partial f}{\partial c}\right)^2 \sigma_c + \dots \quad (\text{B.13})$$

(Note that both this and equation B.12 only hold as written if the uncertainties are uncorrelated. If there is any correlation between them an additional term of the form $2\left(\frac{\partial f}{\partial a}\right)\left(\frac{\partial f}{\partial b}\right)\rho_{ab}$ is required where ρ_{ab} is a function of the correlation).

At this point we have arrived at a mass value and associated uncertainty for each ion measured for each experiment. To combine the masses of a given ion across

experiments we again take a weighted average and find the error in the same manner as we did when combining ω_c values. This will result in one final mass and statistical uncertainty for each nuclide.

The systematic error which is given in section 4.2.5 is given as a fractional error. This needs to be converted to an absolute error (by multiplying it by the mass) before it can be summed in quadrature with the statistical uncertainty to arrive at the final mass uncertainty.

Finding the uncertainty in the mass excess which results from the measured mass is only a matter of multiplying it by the u to keV conversion constant, as the mass uncertainty is the only uncertainty in equation used to calculate the mass excess (equation 4.8).

Appendix C

List of Acronyms

AME Atomic Mass Evaluation [20, 21].

ATLAS Argonne Tandem Linear Accelerator System, located at Argonne National Laboratory, Argonne, Illinois, USA.

BPT Beta Paul Trap, a secondary experimental station attached to the CPT system.

CERN European Organization for Nuclear Research. Acronym comes from the french name: Conseil European pour la Recherche Nuclaire.

CKM Cabibbo-Kobayashi-Maskawa quark-mixing matrix.

CNO cycle Carbon-Nitrogen-Oxygen cycle.

CPT Canadian Penning Trap, located at Argonne National Laboratory, Argonne, Illinois, USA.

DC Direct Current.

FRDM Finite-Range Droplet Model.

HBF Hartree-Fock-Bogolyubov mass model.

IS1 / IS2 1st and 2nd generation (respectively) Isobar Separators.

ISOL Isotope Separation OnLine.

ISOLDE ISOL facility at CERN.

ISOLTRAP Penning trap located at ISOLDE, CERN.

JYFLTRAP Penning trap located in Jyväskylä (JY), Finland (FL).

LEBIT Penning trap located at Michigan State University. Stands for “Low Energy Beam and Ion Trap”.

RF Radio-Frequency.

RFQ Radio-Frequency Quadrupole.

SHIPTRAP Penning trap located after the SHIP velocity filter at GSI (GSI Helmholtz Centre for Heavy Ion Research) in Darmstadt, Germany.

Bibliography

- [1] A. Einstein, *Annalen der Physik* **18**, 639 (1905).
- [2] K. Krane, *Introductory Nuclear Physics*, 2nd Edition, (John Wiley and Sons, Toronto, 1988).
- [3] The Nobel Prize in Physics 1963, (http://nobelprize.org/nobel_prizes/physics/laureates/1963/).
- [4] C. E. Rolfs and W. S. Rodney, *Cauldrons in the Cosmos*, (The University of Chicago Press, Chicago, 1988).
- [5] D. D. Clayton, *Principles of stellar evolution and nucleosynthesis*, (The University of Chicago Press, Chicago, 1983).
- [6] H. E. Duckworth, R. C. Barber and V. S. Venkatasubramanian, *Mass Spectroscopy*, 2nd Edition, (Cambridge University Press, New York, 1986).
- [7] R. C. Barber, R. L. Bishop, H. E. Duckworth, J. O. Meredith, F. C. G. Southon, P. van Rookhuyzen and P. Williams, *Rev. Sci. Instrum.* **42**, 1 (1971).
- [8] P. McCowan, Master's thesis, University of Manitoba, 2008.
- [9] G. Savard and G. Werth, *Annu. Rev. Nucl. Part. Sci.* **50**, 119 (2000).
- [10] J. Vervier, J. Äystö, H. Doubre, S. Morrison, G. Ricco, D. Schwalm and G.-E. Körner, *Nuclear Physics In Europe: Highlights & Opportunities*, Tech. rep., NuPECC (1997).
- [11] G. Savard, J. A. Clark, F. Buchinger, J. E. Crawford, S. Gulick, J. C. Hardy, A. A. Hecht, V. E. Iacob, J. K. P. Lee, A. F. Levand, B. F. Lundgren, N. D. Scielzo, K. S. Sharma, I. Tanihata, I. S. Towner, W. Trimble, J. C. Wang, Y. Wang and Z. Zhou, *Phys. Rev. C* **70**, 042501(R) (2004).
- [12] G. Savard, J. C. Wang, K. S. Sharma, H. Sharma, J. A. Clark, C. Boudreau, F. Buchinger, J. E. Crawford, S. Gulick, J. P. Greene, A. A. Hecht, J. K. P. Lee, A. F. Levand, N. D. Scielzo, W. Trimble, J. Vaz and B. J. Zabransky, *Int. J. Mass. Spec* **251**, 252 (2006).
- [13] N. D. Scielzo, S. Caldwell, G. Savard, J. A. Clark, C. M. Deibel, J. Fallis, S. Gulick, D. Lascar, A. F. Levand, G. Li, J. Mintz, E. B. Norman, K. S. Sharma, M. Sternberg, T. Sun and J. Van Schelt, *Phys. Rev. C* **80**, 025501 (2009).

- [14] G. Savard, F. Buchinger, J. A. Clark, J. E. Crawford, S. Gulick, J. C. Hardy, A. A. Hecht, J. K. P. Lee, A. F. Levand, N. D. Scielzo, H. Sharma, K. S. Sharma, I. Tanihata, A. C. Villari and Y. Wang, Phys. Rev. Lett. **95**, 102501 (2005).
- [15] J. Van Schelt, G. Savard, S. Caldwell, J. A. Clark, J. Fallis, J. P. Green, D. Lascar, A. F. Levand, G. Li, R. E. Segel, K. A. Sharma, M. Sternberg, T. Sun and B. J. Zabransky, in *proceedings of "NIC X"*, (2008), (PoS(NIC X)150).
- [16] J. A. Clark, G. Savard, K. S. Sharma, J. Vaz, J. C. Wang, Z. Zhou, A. Heinz, B. Blank, F. Buchinger, J. E. Crawford, S. Gulick, J. K. Lee, A. F. Levand, D. Seweryniak, G. D. Sprouse and W. Trimble, Phys. Rev. Lett **92**, 192501 (2004).
- [17] J. A. Clark, K. S. Sharma, G. Savard, A. F. Levand, J. C. Wang, Z. Zhou, B. Blank, F. Buchinger, J. E. Crawford, S. Gulick, J. K. P. Lee, D. Seweryniak and W. Trimble, Phys. Rev. C **75**, 032801(R) (2007).
- [18] J. Fallis, J. A. Clark, K. S. Sharma, G. Savard, F. Buchinger, S. Caldwell, J. E. Crawford, C. M. Deibel, J. L. Fisker, S. Gulick, A. A. Hecht, D. Lascar, J. K. P. Lee, A. F. Levand, G. Li, B. F. Lundgren, A. Parikh, S. Russell, M. Scholte-van de Vorst, N. D. Scielzo, R. E. Segel, H. Sharma, S. Sinha, M. Sternberg, T. Sun, I. Tanihata, J. Van Schelt, J. C. Wang, Y. Wang, C. Wrede and Z. Zhou, Phys. Rev. C **78**, 022801(R) (2008).
- [19] J. Fallis, J. A. Clark, K. S. Sharma, G. Savard, F. Buchinger, S. Caldwell, A. Chaudhuri, J. E. Crawford, C. M. Deibel, S. Gulick, A. A. Hecht, D. Lascar, J. K. P. Lee, A. F. Levand, G. Li, B. F. Lundgren, A. Parikh, S. Russell, M. Scholte-van de Vorst, N. D. Scielzo, R. E. Segel, H. Sharma, S. Sinha, M. Sternberg, T. Sun, I. Tanihata, J. Van Schelt, J. C. Wang, Y. Wang, C. Wrede and Z. Zhou (to be submitted to EPJA).
- [20] A. H. Wapstra, G. Audi and C. Thibault, Nucl. Phys. **A729**, 129 (2003).
- [21] G. Audi, A. H. Wapstra and C. Thibault, Nucl. Phys. **A729**, 337 (2003).
- [22] M. Wiescher and H. Schatz, Nucl. Phys. **A693**, 269 (2001).
- [23] A. A. Chen, R. E. Azuma, S. Bishop, L. Buchmann, M. L. Chatterjee, J. M. D'Auria, S. Engel, D. Gigliotti, U. Greife, D. Hunter, A. Hussein, D. Hutcheon, C. C. Jewett, J. José, J. D. King, A. M. Laird, M. Lamey, R. Lewis, W. Liu, A. Olin, D. Ottewell, P. Parker, J. Rogers, C. Ruiz, M. Trinczek and C. Wrede, Nucl. Phys. **A752**, 510 (2005).
- [24] J. L. Fisker, E. F. Brown, M. Liebendörfer, F.-K. Thielemann and M. Wiescher, Nucl. Phys. **A752**, 604 (2005).
- [25] B. A. Brown, R. R. Clement, H. Schatz, A. Volya and W. A. Richter, Phys. Rev. C **65**, 045802 (2002).
- [26] P. Schury, C. Bachelet, M. Block, G. Bollen, D. A. Davies, M. Facina, C. M. Folden III, C. Guénaut, J. Huikari, E. Kwan, A. Kwiatkowski, D. J. Morrissey, R. Ringle, G. K. Pang, A. Prinke, J. Savory, H. Schatz, S. Schwarz, C. S. Sumithrarachchi and T. Sun, Phys. Rev. C **75**, 055801 (2007).

- [27] A. Wöhr, A. Aprahamian, P. Boutachkov, J. L. Galache, J. Görres, M. Shawcross, A. Teymurazyan, M. C. Wiescher, D. S. Brenner, C. N. Davids, S. M. Fischer, A. M. Heinz, R. V. F. Janssens and D. Seweryniak, *Nucl. Phys.* **A742**, 349 (2004).
- [28] M. B. Gómez-Hornillos, M. Chartier, W. Mittig, A. Lépine-Szily, L. Caballero, C. E. Demonchy, G. Georgiev, N. A. Orr, G. Politi, M. Rousseau, P. Roussel-Chomaz and A. C. C. Villari, *Phys. Rev. C* **78**, 014311 (2008).
- [29] F. Herfurth, G. Audi, D. Beck, K. Blaum, G. Bollen, P. Delahaye, C. Guénaut, A. Kellerbauer, H.-J. Kluge, D. Lunney, D. Rodríguez, S. Saxena, S. Schwarz, L. Schweikhard, G. Sikler and C. Yazidjian, *Nucl. Phys.* **A746**, 487 (2004).
- [30] D. Rodríguez, V. S. Kolhinen, G. Audi, J. Äystö, D. Beck, K. Blaum, G. Bollen, F. Herfurth, A. Jokinen, A. Kellerbauer, H.-J. Kluge, M. Oinonen, H. Schatz, E. Sauvan and S. Schwarz, *Eur. Phys. J. A Suppl.* **25**, 41 (2005).
- [31] G. Sikler, G. Audi, D. Beck, K. Blaum, G. Bollen, F. Herfurth, A. Kellerbauer, H.-J. Kluge, D. Lunney, M. Oinonen, C. Scheidenberger, S. Schwarz and J. Szerypo, *Nucl. Phys.* **A763**, 45 (2005).
- [32] D. Rodríguez, G. Audi, J. Äystö, D. Beck, K. Blaum, G. Bollen, F. Herfurth, A. Jokinen, A. Kellerbauer, H.-J. Kluge, V. S. Kolhinen, M. Oinonen, E. Sauvan and S. Schwarz, *Nucl. Phys.* **A769**, 1 (2006).
- [33] H. Schatz, *Int. J. Mass Spectrom.* **251**, 293 (2006).
- [34] H. Schatz, A. Aprahamian, J. Görres, M. Wiescher, T. Rauscher, J. F. Rembges, F.-K. Thielemann, B. Pfeiffer, P. Möller, K.-L. Kratz, H. Herndl, B. A. Brown and H. Rebel, *Phys. Rep.* **294**, 167 (1998).
- [35] N. N. Weinberg, L. Bildsten and H. Schatz, *Astro. Phys. J* **639**, 1018 (2006).
- [36] H. Schatz, *Nucl. Phys.* **A746**, 347 (2004).
- [37] M. Arnould and S. Goriely, *Phys. Rep.* **384**, 1 (2003).
- [38] C. Fröhlich, G. Martínez-Pinedo, M. Liebendörfer, F.-K. Thielemann, E. Bravo, W. R. Hix, K. Langanke and N. T. Zinner, *Phys. Rev. Lett.* **96**, 142502 (2006).
- [39] J. Pruet, R. D. Hoffman, S. E. Woosley, H.-T. Janka and R. Buras, *Astrophys. J.* **644**, 1028 (2006).
- [40] J. L. Fisker, R. D. Hoffman and J. Pruet, (arXiv:0711.1502v1 [astro-ph]) (2007).
- [41] J. L. Fisker, R. D. Hoffman and J. Pruet, *Astrophys. J.* **690**, L135 (2009), (arXiv:0711.1502v2 [astro-ph]).
- [42] C. Weber, V.-V. Elomaa, R. Ferrer, C. Fröhlich, D. Ackermann, J. Äystö, G. Audi, L. Batist, K. Blaum, M. Block, A. Chaudhuri, M. Dworschak, S. Eliseev, T. Eronen, U. Hager, J. Hakala, F. Herfurth, F. Heberger, S. Hofmann, A. Jokinen, A. Kankainen, H.-J. Kluge, K. Langanke, A. Martín, G. Martínez-Pinedo, M. Mazzocco, I. Moore, J. Neumayr, Y. Novikov, H. Penttilä, W. Plaß, A. Popov, S. Rahaman, T. Rauscher, C. Rauth, J. Rissanen, D. Rodríguez, A. Saastamoinen, C. Scheidenberger, L. Schweikhard, D. Seliverstov, T. Sonoda, F.-K. Thielemann, P. Thirof and G. Vorobjev, *Phys. Rev. C* **78**, 054310 (2008).

- [43] L. S. Brown and G. Gabrielse, *Rev. of Mod. Phys.* **58**, 233 (1986).
- [44] G. Savard, S. Becker, G. Bollen, H.-J. Kluge, R. B. Moore, T. Otto, L. Schweikhard, H. Stolzenberg and U. Wiess, *Phys. Lett.* **A158**, 247 (1991).
- [45] P. H. Dawson (Ed.), *Quadrupole Mass Spectroscopy and its Applications*, (Elsevier Scientific Publishing Company, New York, 1976).
- [46] E. A. Mason and E. W. McDaniel, *Transport Properties of Ions in Gases*, (John Wiley & Sons, New York, 1988).
- [47] N. R. Whetten, *J. of Vac. Sci. Technol.* **11**, 515 (1974).
- [48] A. Gavron, *Phys. Rev. C* **21**, 230 (1980).
- [49] J. Clark, Ph.D. thesis, University of Manitoba, 2005.
- [50] J. Clark, R. C. Barber, C. Boudreau, F. Buchinger, J. E. Crawford, S. Gulick, J. C. Hardy, A. Heinz, J. K. P. Lee, R. B. Moore, G. Savard, D. Seweryniak, K. S. Sharma, G. Sprouse, J. Vaz, J. C. Wang and Z. Zhou, *Nucl. Inst. and Meth. in Phys. Res. B* **204**, 487 (2003).
- [51] G. Savard, J. Clark, C. Boudreau, F. Buchinger, J. E. Crawford, H. Geissel, J. P. Greene, S. Gulick, A. Heinz, J. K. P. Lee, A. Levand, M. Maier, G. Münzenberg, C. Scheidenberger, D. Seweryniak, K. S. Sharma, G. Sprouse, J. Vaz, J. C. Wang, B. J. Zabransky, Z. Zhou and The S258 Collaboration, *Nucl. Inst. and Meth. in Phys. Res. B* **204**, 582 (2003).
- [52] G. Savard, S. Baker, C. Davids, A. F. Levand, E. F. Moore, R. C. Pardo, R. Vondrasek, B. J. Zabransky and G. Zinkann, *Nucl. Inst. and Meth. in Phys. Res. B* **266**, 4086 (2008).
- [53] W. Trimble, G. Savard, B. Blank, J. A. Clark, F. Buchinger, T. Cocolios, J. E. Crawford, A. Frankel, J. P. Greene, S. Gulick, J. K. P. Lee, A. Levand, M. Portillo, K. S. Sharma, W. J. C., B. J. Zabransky and Z. Zhou, *Nucl. Phys.* **A726**, 415 (2004).
- [54] G. Bollen, S. Becker, H.-J. Kluge, M. König, R. B. Moore, T. Otto, H. Raimbault-Hartmann, G. Savard, L. Schweikhard and H. Stolzenberg, *Nucl. Inst. and Meth. in Phys. Res. A* **368**, 675 (1996).
- [55] G. Bollen, *Nucl. Phys.* **A693**, 3 (2001).
- [56] G. Bollen, R. B. Moore, G. Savard and H. Stolzenberg, *J. Appl. Phys.* **68**, 4355 (1990).
- [57] G. Bollen, H.-J. Kluge, M. König, T. Otto, G. Savard, H. Stolzenberg, R. B. Moore, G. Rouleau, G. Audi and Isolde Collaboration, *Phys. Rev. C* **46**, 2140 (1992).
- [58] J. V. F. Vaz, Ph.D. thesis, University of Manitoba, 2002.
- [59] A. Kankainen, L. Batist, S. A. Eliseev, V.-V. Elomaa, T. Eronen, U. Hager, J. Hakala, A. Jokinen, I. Moore, Y. N. Novikov, H. Penttilä, K. Peräjärvi, A. V. Popov, S. Rahaman, S. Rinta-Antila, P. Ronkanen, A. Saastamoinen, D. M. Seliverstov, T. Sonoda, G. K. Vorobjev and J. Äystö, *Eur. Phys. J. A* **29**, 271 (2006).

- [60] A. Kankainen, V.-V. Elomaa, L. Batist, S. Eliseev, T. Eronen, U. Hager, J. Hakala, A. Jokinen, I. D. Moore, Y. N. Novikov, H. Penttilä, A. Popov, S. Rahaman, S. Rinta-Antila, J. Rissanen, A. Saastamoinen, D. M. Seliverstov, T. Sonoda, G. Vorobjev, C. Weber and J. Äystö, *Phys. Rev. Lett.* **101**, 142503 (2008).
- [61] D. Lunney, J. M. Pearson and C. Thibault, *Rev. of Mod. Phys.* **75**, 1021 (2003).
- [62] S. Goriely, N. Chamel and J. M. Pearson, *Phys. Rev. Lett.* **102**, 152503 (2009).
- [63] P. Möller, J. R. Nix, W. D. Myers and W. J. Swiatecki, *At. Data Nucl. Data Tables* **59**, 185 (1995).
- [64] S. Della Negra, D. Jacquet and Y. Le Beyec, *Z. Phys* **A308**, 243 (1982).
- [65] B. J. Min, S. Suematsu, S. Mitarai, T. Kuroyanagi, K. Heiguchi and M. Matsuzaki, *Nucl. Phys.* **A530**, 211 (1991).
- [66] E. Hagberg, J. C. Hardy, H. Schmeing, E. T. H. Clifford and V. T. Koslowsky, *Nucl. Phys.* **A395**, 152 (1983).
- [67] Pettersson, H. and Bäckström, G. and Bergman, C., *Nucl. Phys.* **83**, 33 (1966).
- [68] R. L. Bishop, R. C. Barber, W. McLatchie, J. D. MacDougall, P. van Rookhuizen and H. E. Duckworth, *Can. J. Phys.* **41**, 1532 (1963).
- [69] R. R. Ries, R. A. Damerow and W. H. Johnson, *Phys. Rev.* **132**, 1662 (1963).
- [70] K. Oxorn and S. K. Mark, *Z. Phys.* **303**, 63 (1981).
- [71] R. Iafigliola, S. C. Gujrathi, B. L. Tracy and J. K. P. Lee, *Can. J. Phys.* **52**, 96 (1974).
- [72] E. Browne, *Nuclear Data Sheets* **82**, 379 (1997).
- [73] D. Rudolph, C. J. Gross, M. K. Kabadiyski, K. P. Lieb, M. Weiszflog, H. Grawe, J. Heese, K.-H. Maier and J. Eberth, *Phys. Rev. C* **47**, 2574 (1993).
- [74] S. Dean, M. Górska, F. Aksouh, H. de Witte, M. Facina, M. Huyse, O. Ivanov, K. Krouglov, Y. Kudryavtsev, I. Mukha, D. Smirnov, J.-C. Thomas, K. Van de Vel, J. Van de Walle, P. Van Duppen and J. Van Roosbroeck, *Eur. Phys. J. A* **21**, 243 (2004).
- [75] G. Audi, O. Bersillon, J. Blachot and A. H. Wapstra, *Nucl. Phys.* **A729**, 3 (2003).
- [76] J. Äystö, J. Honkanen, W. Trzaska, K. Eskola, K. Vierinen and S. Messelt, *Nucl. Phys.* **A404**, 1 (1983).
- [77] Y. Litvinov, Ph.D. thesis, Justus-Liebig Universität Gießen, 2005.
- [78] J. Heese, H. Grawe, K. H. Maier, R. Schubart, F. Cristancho, C. J. Gross, A. Jungclaus, K. P. Lieb, D. Rudolph, J. Eberth and S. Skoda, *Phys. Rev. C* **49**, 1896 (1994).

- [79] S. E. Arnell, D. Foltescu, H. A. Roth, Ö. Skeppstedt, A. Nilsson, S. Mitarai and J. Nyberg, *Phys. Scripta* **47**, 355 (1993).
- [80] J. B. Ball, *Nucl. Phys.* **A160**, 225 (1971).
- [81] C. Baglin, *Nuclear Data Sheets* **91**, 423 (2000).
- [82] D. Kast, A. Jungclaus, A. Harder, K. P. Lieb, D. Rudolph, R. Schubart, H. Grawe, D. Foltescu, H. A. Roth, O. Skeppstedt, I. Bearden and T. Shizuma, *Z. Phys.* **A356**, 363 (1997).
- [83] H. Herndl and B. A. Brown, *Nucl. Phys.* **A627**, 35 (1997).
- [84] K. Kaneko, Y. Sun, M. Hasegawa and T. Mizusaki, *Phys. Rev. C* **77**, 064304 (2008).
- [85] O. L. Pechenaya, C. J. Chiara, D. G. Sarantites, W. Reviol, R. J. Charity, M. P. Carpenter, R. V. F. Janssens, T. Lauritsen, C. J. Lister, D. Seweryniak, S. Zhu, L.-L. Andersson, E. K. Johansson and D. Rudolph, *Phys. Rev. C* **76**, 011304 (2007).
- [86] K. Oxorn, B. Singh and S. K. Mark, *Z. Phys.* **294**, 389 (1980).
- [87] W. Kurcewicz, E. F. Zganjar, R. Kirchner, O. Klepper, E. Roeckl, P. Komninos, E. Nolte, D. Schardt and P. Tidemand-Petersson, *Z. Phys.* **308**, 21 (1982).
- [88] S. E. Arnell, D. Foltescu, H. A. Roth, O. Skeppstedt, J. Blomqvist, A. Nilsson, T. Kuroyanagi, S. Mitarai and J. Nyberg, *Phys. Rev. C* **49**, 51 (1994).
- [89] L. Batist, A. Blazhev, J. Döring, H. Grawe, M. Kavatsyuk, O. Kavatsyuk, R. Kirchner, M. La Commara, C. Mazzocchi, I. Mukha, C. Plettner, E. Roeckl and M. Romoli, *Eur. Phys. J.* **A29**, 175 (2006).
- [90] J. A. Clark, R. C. Barber, B. Blank, C. Boudreau, F. Buchinger, J. E. Crawford, J. P. Greene, S. Gulick, J. C. Hardy, A. A. Hecht, A. Heinz, J. K. P. Lee, A. F. Levand, B. F. Lundgren, R. B. Moore, G. Savard, N. D. Scielzo, D. Seweryniak, K. S. Sharma, G. D. Sprouse, W. Trimble, J. Vaz, J. C. Wang, Y. Wang, B. J. Zabransky and Z. Zhou, *Eur. Phys. J. A Suppl.* **25**, 629 (2005).
- [91] G. T. Garvey and I. Kelson, *Phys. Rev. Lett.* **16**, 197 (1966).
- [92] G. T. Garvey, W. J. Gerace, R. L. Jaffe, I. Talmi and I. Kelson, *Rev. Mod. Phys.* **41**, 1 (1969).
- [93] T. Rauscher and F.-K. Thielemann, *At. Data Nucl. Data Tables* **75**, 1 (2000).
- [94] P. Möller, J. R. Nix, W. D. Myers and W. J. Swiatecki, *At. Data Nucl. Data Tables* **59**, 185 (1995).
- [95] A. Parikh, J. José, C. Iliadis, F. Moreno and T. Rauscher, *Phys. Rev. C* **79**, 045802 (2009).
- [96] A. Parikh, private communication (2009).

- [97] I. Mukha, E. Roeckl, L. Batist, A. Blazhev, J. Döring, H. Grawe, L. Grigorenko, M. Huyse, Z. Janas, R. Kirchner, M. La Commara, C. Mazzocchi, S. L. Tabor and P. van Duppen, *Nature* **439**, 298 (2006).
- [98] I. Mukha, E. Roeckl, J. Döring, L. Batist, A. Blazhev, H. Grawe, C. R. Hoffman, M. Huyse, Z. Janas, R. Kirchner, M. La Commara, C. Mazzocchi, C. Plettner, S. L. Tabor, P. V. Duppen and M. Wiedeking, *Phys. Rev. Lett.* **95**, 022501 (2005).
- [99] D. Griffiths, *Introduction to Electrodynamics*, 3rd Edition, (Prentice Hall, New Jersey, 1999).
- [100] P. R. Bevington and D. K. Robinson, *Data Reduction and Error Analysis for the Physical Sciences*, 2nd Edition, (WBC McGraw-Hill, Wisconsin, 1992).